X-ray spectroscopy of deposited noble metal clusters

vorgelegt von
Diplom-Physiker
Sven Peters
Frankfurt (Oder)

Von der Fakultät II - Mathematik und Naturwissenschaften
der Technischen Universität Berlin
zur Erlangung des akademischen Grades
Doktor der Naturwissenschaften
Dr. rer. nat.

genehmigte Dissertation

Promotionsausschuss:

Vorsitzender:	Prof. Dr. Janina Maultzsch
Berichter/Gutachter:	Prof. Dr. Dr. h.c. Wolfgang Eberhardt
Berichter/Gutachter:	Prof. Dr. Klaus Rademann

Tag der wissenschaftlichen Aussprache: 20. August 2012

Berlin 2012

D 83

Kurzfassung

In dieser Arbeit wurden deponierte massenselektierte Metallcluster mit Hilfe weicher Röntgen-Synchrotronstrahlung untersucht. Die Cluster wurden mit einer Magnetronclusterquelle hergestellt, massenselektiert und zerstörungsfrei auf der natürlichen Siliziumdioxidschicht eines p-dotierten Siliziumwafers deponiert. Inbesondere Kupfer- und Goldcluster wurden mit Röntgen-Photoelektronenspektroskopie, Augerelektronenspektroskopie und kanten-ferner Röntgenabsorptionsspektroskopie an der Synchrotronstrahlungsquelle Bessy II analysiert, um die elektronische und geometrische Struktur in Abhängigkeit der Clustergröße zu erforschen.

Die Gold 4f Rumpfniveau-Bindungsenergie nimmt mit abnehmender Clustergröße zu und skaliert mit dem inversen Clusterradius in Übereinstimmung mit dem klassischen "metal sphere model". Der größenabhängige XPS-Shift ist eindeutig kleiner als erwartet für freie Cluster aufgrund von dynamischen außeratomaren Screenings des Rumpflochs durch das Substrat. In Kupferclustern wurde ein größenabhängiger PCI-Shift beobachtet, welcher verdeutlicht, dass die Photoelektron-Rumpfloch-Wechselwirkung sich schrittweise von einer coulombartigen in eine abgeschirmte coulombartige Wechselwirkung verändert. Das verringerte Vermögen von Clustern kleiner als 10 Angström Ladungen effektiv abzuschirmen zeigt, dass die elektronischen Eigenschaften dieser Cluster eher nichtmetallisch sind im Vergleich zum Festkörper. K-Kanten Absorptionsspektroskopie offenbart eine Kontraktion der Bindungslängen von kleinen Kupferclustern von 8%. In oxidierten Kupferclustern konnten mehrere Kupfer-Kupferbindungen identifiziert werden.

Abstract

The present thesis deals with the spectroscopic study of supported mass-selected metal clusters using soft X-ray synchrotron radiation. The clusters have been produced by a magnetron cluster source, mass-separated and softly landed onto a thin silica layer naturally grown on a doped Si-wafer. In particular, copper (Cu_n, n=8-55) and gold (Au_n, n=1-35) clusters have been analysed by means of X-ray photoelectron spectroscopy (XPS), Auger electron spectroscopy (AES) and extended X-ray absorption spectroscopy (EXAFS) at the synchrotron light source Bessy II in order to investigate the electronic and geometric structure as function of cluster size.

The gold 4f core level binding energy is increasing with decreasing cluster size and is found to be scalable with the inverse cluster radius according to the classical metal sphere model. The size-dependent XPS shift is clearly smaller than expected for free clusters due to dynamic extra-atomic core hole screening by the substrate. In copper clusters a size-dependent PCI-shift has been observed which reveals that the photoelectron core-hole interaction gradually changes from a Coulomb-like into a screened Coulomb-like interaction within the sub-nm range. The reduced screening ability of the clusters smaller than 10 Å illustrates that the electronic properties of the clusters are rather non-metallic as compared to the solid phase. K-edge EXAFS measurements reveals a bond length contraction for small copper clusters from 2.55 to 2.36 Å. In oxidised copper clusters multiple Cu-Cu bonds have been identified.

Contents

Kurzfassung **2**

Abstract **3**

1 Introduction **5**

2 Cluster deposition and synchrotron light source **6**

2.1 Cluster deposition 6

2.1.1 Vacuum system 6

2.1.2 Cluster source 8

2.1.3 Mass separation 10

2.1.4 Cluster deposition 13

2.1.5 Cluster size optimization 17

2.1.6 UHV-suitcase and EXAFS chamber 18

2.2 Synchrotron light facility 20

2.2.1 Beamlines and end stations 22

3 X-ray spectroscopy techniques **27**

3.1 X-ray photoelectron spectroscopy (XPS) 27

3.2 Auger electron spectroscopy (AES) 29

3.3 Extended X-ray absorption fine structure (EXAFS) 31

4 Experimental results **33**

4.1 X-ray photoelectron spectroscopy of deposited Au_n clusters ($n = 1-35$) 33

4.2 Auger electron spectroscopy of deposited Cu_n clusters ($n = 8 - 55$) . 47

4.2.1 Post collision interaction in Cu clusters 50

4.3 X-ray absorption fine structure of deposited Cu_n clusters ($n = 19; 35; 55$) 59

4.3.1 X-ray absorption near edge structure 59

4.3.2 Extended X-ray absorption fine structure 61

5 Summary **73**

Bibliography **75**

Publications **85**

Acknowledgements **87**

1 Introduction

Clusters are aggregates of atoms or molecules of a few to several thousands. The physical and chemical properties of these extremely small nanoparticles such as electronic and geometric structure, magnetism [1], metallicity [2, 3] and catalytic reactivity [4, 5, 6] are generally strikingly different from those of the single atom and macroscopic solid. Very small clusters composed of just a few atoms can usually be treated by concepts of atomic and molecular physics. The properties of very large clusters, on the other hand, gradually evolve into those of the macroscopic solid. The size region in between, i.e. the so-called "each-atom-counts" regime, is highly influenced by quantum-size effects, a single atom adding or removing from a cluster in the each-atom-counts regime can alter the properties in a substantial manner. An accurate size separation is thus necessary in order to study the properties of clusters with high accuracy. Generally speaking, the intention of cluster research is to determine the properties as function of cluster size.

Clusters can be studied as free particles [7, 8, 9, 10, 11] or as deposited clusters on a substrate [12, 13, 14, 15, 16, 17]. To measure the pristine properties of free clusters an intense cluster source is required to achieve an appropriate target density for spectroscopic exploration. For potential kinds of applications the clusters have to be brought into contact with a substrate. Thus the cluster-support interaction becomes an important concern. To study deposited clusters it is possible to deposit free mass-selected clusters under soft-landing conditions to accumulate a coverage density of a few percent of an atomic monolayer in a reasonable time. At this coverage element-specific X-ray spectroscopic methods can be applied in order to receive cluster-specific information of application-relevant supported clusters.

To explore the electronic and geometric structure of deposited metal clusters a variety of X-ray spectroscopic techniques have been used: X-ray photoelectron spectroscopy has been applied to gold clusters in order to analyse the size-dependent XPS binding energy shift. PCI-Auger electron spectroscopy has been applied to copper clusters to reveal information about the electrostatic screening ability of small clusters. Moreover extended X-ray absorption spectroscopy has been used to receive nearest neighbour distances of mass-selected copper clusters for the very first time. In general, metal clusters [18] are of special interest due to their potential applications as new semiconductors, catalysts and magnets.

All measurements have been done at the synchrotron light source Bessy II. Synchrotron radiation and its high brilliance is ideally suited to explore mass-selected clusters. The possibility of varying the photon energy allows for X-ray absorption spectroscopy, to measure the desired core level at the maximum photoionisation cross section, and to measure photon-energy dependent PCI-Auger spectra of mass-selected clusters.

2 Cluster deposition and synchrotron light source

2.1 Cluster deposition

Figure 2.1 shows a sketch of the cluster deposition apparatus [19, 20, 21]. The clusters are produced by a combination of magnetron sputtering and gas aggregation. By use of electrostatic lenses the cluster cations are accelerated to a kinetic energy of 2900 eV and focused onto the entrance slit of a dipole bending magnet. The magnet resolves the different cluster masses and focuses a particular mass onto the exit slit. Immediately behind the exit slit it is possible to record a mass spectrum by using a secondary electron multiplier (SEM). If the SEM is not used the clusters are transmitted and focused into the deposition chamber. After deceleration the clusters are focused onto a biased substrate. Finally the cluster sample is transferred with the help of an UHV suitcase to the beamline endstation.

2.1.1 Vacuum system

In order to avoid contamination the pressure in the deposition chamber should be in the low 10^{-9} mbar range during deposition. As the pressure in the aggregation tube is in the order of 1 mbar, that means 9 orders of magnitude higher, the cluster deposition setup uses five differentiell pumping stages.

The source chamber which is separated from the aggregation tube by a nozzle is pumped by a 2200 l/s turbopump (Pfeiffer TPU 2200 S) with a 130 m^3/h side channel pump (Pfeiffer Booster 150) as forepump. Here is a pressure of about 10^{-3} mbar. Between the two skimmers there is a 880 l/s turbopump (Pfeiffer TMU 1001 P) with a rotary vane pump as forepump and a pressure of about 10^{-5} mbar. In front of the magnet a 180 l/s turbopump (Pfeiffer TPU 180 H) is pumping and a pressure of about 10^{-6} mbar is reached. Just because of the low cross section ((5×3) cm^2, length 50 cm) of the ion flight tube between the poles of the bending magnet we get a two orders of magnitude better pressure behind the bending magnet. Here the chamber is pumped by a 210 l/s turbopump (Pfeiffer TMU 260). Finally the deposition chamber is pumped by a 450 l/s turbopump (Pfeiffer TPU 450 H). Upon baking the final deposition chamber it is possible to get a base pressure without gas load in the low 10^{-10} mbar range. The turbopumps before the magnet, behind the magnet an at the deposition chamber have the same forepump a 10 m^3/h scroll pump (Boc Edwards XDS10).

The cross between the UHV suitcase and the deposition chamber or the beamline endstation is pumped by a 210 l/s turbopump (Pfeiffer TMU 261) and is baked after every assembly. To keep the pressure of about 10^{-9} mbar during transport the UHV suitcase is equipped with a 40 l/s ion getter pump (Gamma Vacuum 45S) powered

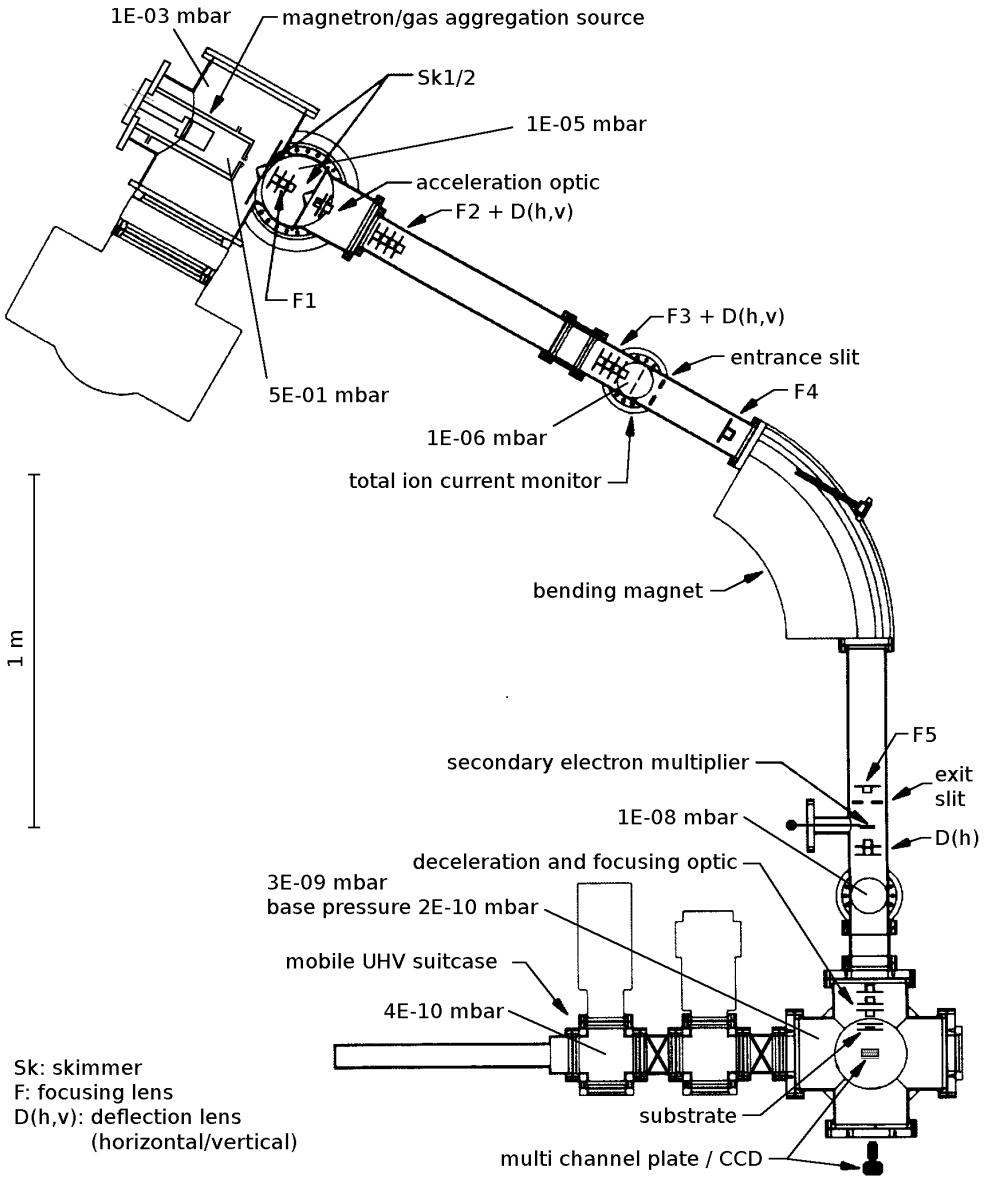

Figure 2.1: *Overview of the cluster deposition setup. The cluster cations are generated by combination of a magnetron discharge and gas aggregation source. After acceleration to 2900 eV the clusters are mass-selected by a bending magnet. A mass spectrum can be recorded behind the exit slit with a secondary electron multiplier. After deceleration the clusters are soft landed with less than 1 eV per atom onto a biased substrate. Using a home-built the UHV suitcase it is possible to move the cluster covered samples without breaking the vacuum to a synchrotron endstation.*

by a car battery. Between car battery and power supply of the getter pump a DC-DC converter is connected to provide a voltage of 24 V needed by the power supply.

2.1.2 Cluster source

The home-built magnetron cluster source is essentially similar to the one described by the Haberland group [22]. The magnetron cluster source is capable of producing a continuous cluster beam with an adjustable mass distribution. Moreover the magnetron sputter head enables vaporisation of a wide range of materials, such as metals and semiconductors. The magnetron sputtering head (ION'X-2UHV, Thin Film Consulting) is located in a double walled, liquid nitrogen cooled aggregation tube as shown in figure 2.2. A negative voltage provided by a dc power supply is ap-

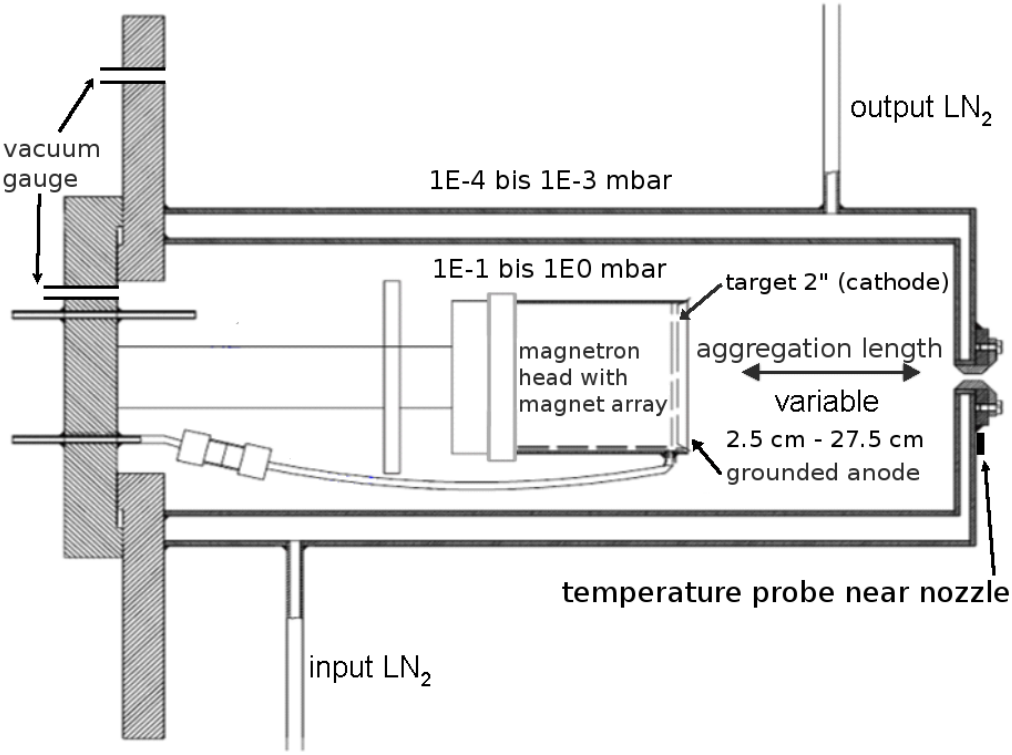

Figure 2.2: *Sketch of the magnetron sputtering gas aggregation source. With the commercial magnetron sputter head it is possible to evaporate a wide variety of target materials. The difference between the pressure in the aggregation tube and the source chamber is three orders of magnitude, leading to a supersonic expansion of the cluster gas mixture.*

plied to the target (cathode) whereas the annular anode is grounded. To sputter the material of interest argon gas (≈ 60 sccm continuous flow) is guided directly between the target and the anode. Helium (< 20 sccm continuous flow), which is used as aggregation gas, is introduced directly into the aggregation chamber. Both process

gases are individually dosed with the help of two gas flow controllers. The sputtered atoms aggregate in collisions with the surrounding argon and helium atoms. The cluster gas mixture is swept towards the nozzle at the end of the aggregation tube. Because of the high difference in pressure the cluster gas mixture leaves the aggregation tube within an adiabatic supersonic expansion. This cools the vapour mixture and forms a narrow cluster beam with a small velocity distribution. The cluster beam passes a first skimmer which collimates the clusters and deflects the aggregation gas.

Magnetron sputter head

Atoms are sputtered from the target surface by bombarding with high energetic argon ions, which are produced in a dc plasma discharge. Plasma confinement is achieved by a permanent magnet array located behind the target. The resulting magnet field forces the secondary electrons ejected from the target onto a spiral path around a ring above the target. This greatly enhances the ionization rate as well as the sputter rate. The sputter yield is increased even at lower pressures especially because magnetrons usually are operated at much lower pressures. Since the ion bombardment mainly takes place where the magnetic field lines are parallel to the target surface the abrasion region forms an annular ring on the target (figure 2.3). The sputter targets have a diameter of 2 " and a thickness of 2-5 mm depending on the material. As most of the energy applied to the magnetron is converted into heat, the target mount is made of copper and water-cooled.

Gas aggregation

The sputtered atoms are swept into the aggregation region between the magnetron head and the nozzle. Here the cluster growth starts with dimers. If not sputtered directly from the target the dimers are generated by three body collisions due to energy and momentum conversation. At the beginning when single atoms dominate over larger clusters the clusters grow by adding single atoms. Further downstream, when the density of larger clusters increases the clusters grow by cluster cluster agglomeration. The inverse process is also possible, that means that the clusters might evaporate atoms. To avoided this a cold aggregation gas is injected which carries away the excess binding energy. The cluster growth is enhanced by the high pressure of the cold aggregation gas inside the aggregation tube. The collision probability is increased by the high pressure of the argon helium mixture whereas the cooling slows down the particles to increase the collision duration. The double walled aggregation tube is cooled down in about 20 min by liquid nitrogen, with a consumption of 20 l per hour. To keep a constant temperature of the aggregation

Figure 2.3: *Used copper sputtering target with a diameter of 2″ and a height of 4 mm. The sputtered circle has a diameter of 2.5 cm. Plasma confinement mainly takes place above the circle.*

tube, a constant liquid nitrogen flow is used at which a temperature of -170 °C is measured at the nozzle.

2.1.3 Mass separation

As the cluster source provides a very stable, continuous beam of clusters it is ideally suited to be combined with a static magnetic sector field mass filter. After acceleration and collimation by a system of electrostatic lenses, the clusters pass the entrance slit of the mass filter (AMD M-60 CLS). The magnet consists of two coils in parallel circuit. The gap between the poles is 15 mm, the angle of deflection is 58 ° and the radius is 462 mm. The lower pole is the north pole, so the the field lines direct perpendicular upwards. The maximum magnetix flux density is 1.5 T. Due to the Lorentz force the magnet spatially resolves the clusters by their momentum and focuses one cluster size onto a point of the focal plane, where one cluster size passes the variable exit slit of the mass filter. Behind the exit slit a moveable secondary electron multiplier is located. By scanning the current through the coils (0-22 A) and keeping a constant acceleration voltage a mass spectrum can be recorded.

In figure 2.4 a silver clusters mass spectrum is shown. The cluster intensities follow a log-normal size distribution, as usually observed for inert-gas aggregation sources. This shows the proper working conditions of this source, that is single-

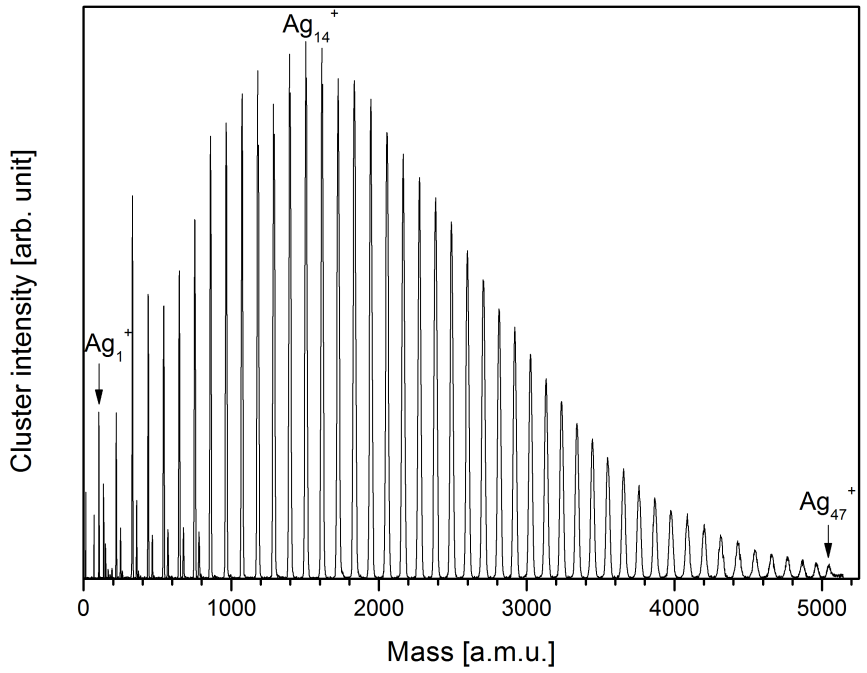

Figure 2.4: *A mass spectrum of silver clusters. With the clusters having a kinetic energy of 2900 eV the bending magnet can resolve masses up to 5000 a.m.u..*

particle growth and agglomeration growth [23]. To assign the peaks in the mass spectrum to the corresponding cluster mass and to get a calibration curve for the mass selector, one can use the isotope pattern. Copper for example has two stable isotopes. ^{63}Cu with an abundance of 69% and ^{65}Cu with an abundance of 31%. Hence Cu_2 consists of three peaks with a ratio of $^{65+65}$Cu : $^{63+65}$Cu : $^{65+65}$Cu = 100:90:20.

$$^{63}Cu + {}^{63}Cu = 0.69 \cdot 0.69 \tag{2.1}$$

$$^{63}Cu + {}^{65}Cu = 0.69 \cdot 0.31 + 0.31 \cdot 0.69 \tag{2.2}$$

$$^{65}Cu + {}^{65}Cu = 0.31 \cdot 0.31 \tag{2.3}$$

In figure 2.5 the isotope pattern of the Cu_1 monomer and the Cu_2 dimer is shown from which the resolution $m/\Delta m$ ($\Delta m = FWHM$) of the mass selector can be deduced. The monomer is clearly resolved and the dimer is nearly resolved. Hence a resolution of $m/\Delta m \approx 115$ at fully open slit results. The same value over the whole mass range is received by the evaluation of the peak width of an isotope-free gold mass spectrum. Figure 2.6 exemplarily shows the mass peaks of the gold clusters Au_2, Au_{12} and Au_{22}. From all three mass peaks a resolution of approximate

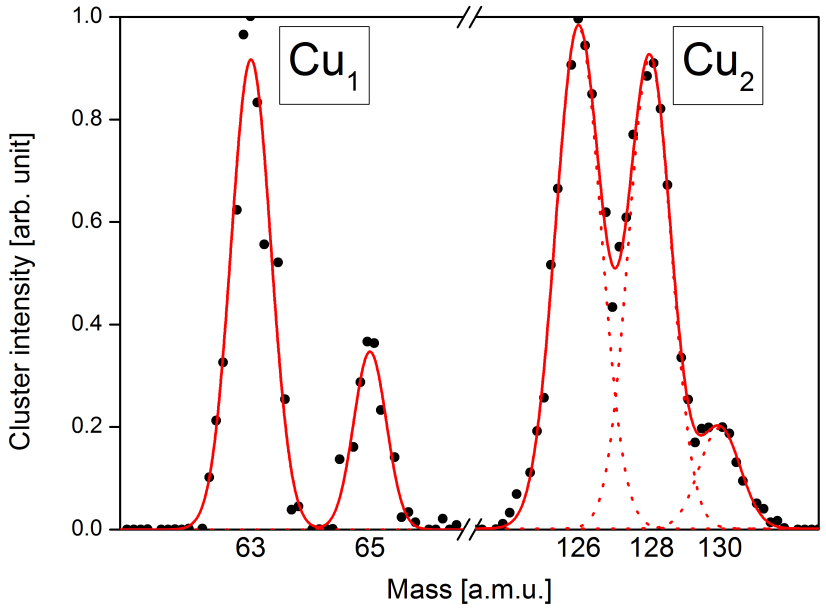

Figure 2.5: *Isotope Pattern of the clusters Cu_1^+ and Cu_2^+. The monomer is clearly resolved and the dimer almost. Hence a resolution of $m/\Delta m = 115$ can be deduced from the spectrum.*

115 can be deduced. Due to the increasing absolute width of the mass peaks with increasing mass the point density of the mass peaks is increasing too. With a kinetic energy of 2900 eV the bending magnet can resolve masses up to 5000 a.m.u.. Note that the mass spectra of a bending magnet are not linear in mass, in other words the distances between the cluster peaks are not equal (See figure 2.5, the mass spectrum in figure 2.4 is calibrated). To achieve a constant distance a calibration curve is needed for each acceleration voltage.

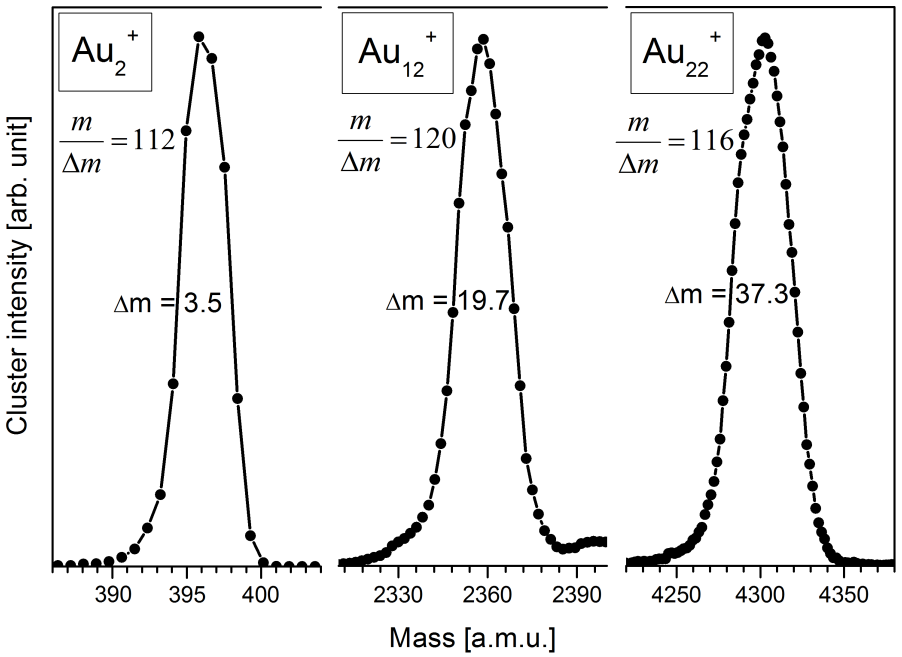

Figure 2.6: *Mass peaks of the clusters Au_2, Au_{12} and Au_{22} out of an isotope free gold cluster mass spectrum. The resolution of the mass selector is directly determined by the FWHM (Δm) and the mass of the individual mass peaks.*

2.1.4 Cluster deposition

After passing the exit slit of the bending magnet the clusters are horizontally deflected and focused before entering the deposition chamber. For a non-destructive deposition the high kinetic energy of the cluster cations is reduced by an assembly of electrostatic lenses that refocuses and decelerates the ion beam trough a final aperture of 6 mm in diameter (Figure 2.7). This aperture is placed about 2 mm in front of the substrate surface. A gold mesh with a transmission of 80% covers the last orifice to keep a homogeneous electric field between the last lens element and the substrate. The isolated substrate is connected to an electrometer (Keithley 617) to measure the ion current and to apply a voltage to the substrate. During deposition the ion current is continuously recorded and simultaneously integrated over the time. The voltage can be varied between -100 V and +100 V. To allow for a non-destructive landing the clusters have to be soft landed with kinetic energies smaller than 1 eV/atom. Usually the clusters are deposited with energies about 0.5 eV per atom; bigger clusters with even lower kinetic energies. To adjust the desired bias voltage, which of course depends on the cluster size, the substrate voltage is varied until the deposition current drops to zero or starts to increase. From this bias a

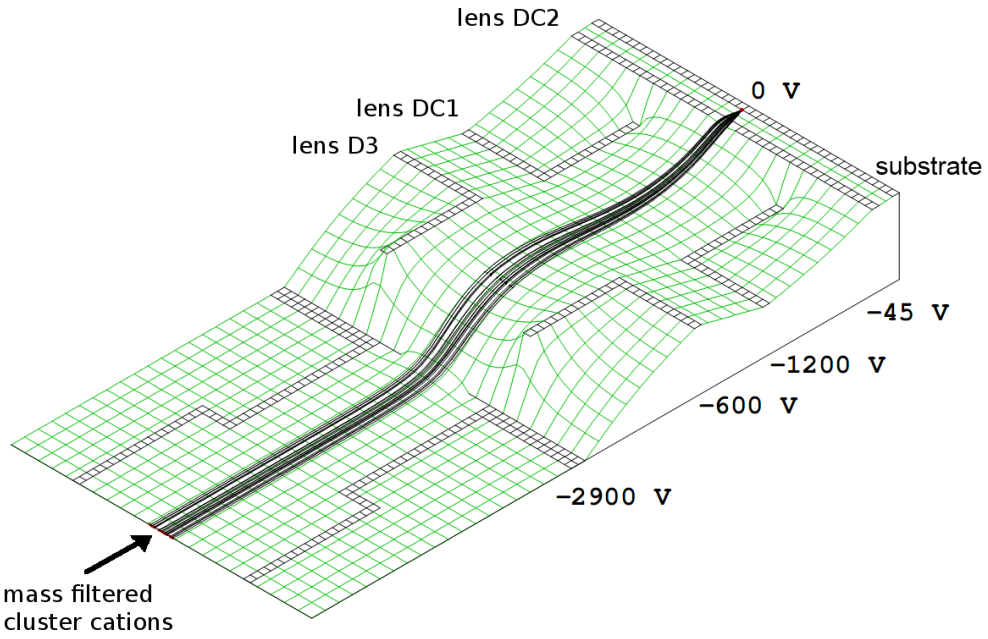

Figure 2.7: *Simion simulation of the soft-landing ion lens assembly. The orifice of the last lens DC2 is covered with a gold mesh. The substrate is biased.*

voltage less than 1 eV/atom is subtracted in order to perform soft landing deposition for each cluster size. Figure 2.8 shows the deposition current for a particular cluster size (Au_{25}^{+}). In less than two minutes Au_{25} clusters with a total number of 1.3×10^{12} atoms are deposited. Depending on the cluster size and the cluster current the deposition time typically varies between 5 and 60 minutes.

To get an idea about the cluster density on the substrate, which is important to avoid agglomeration of individual clusters, it is necessary to know the cluster spot size on the substrate and the amount of clusters deposited. The surface coverage distribution is visualized with the help of a spatially resolved ion beam monitor. It is also possible to measure the position dependent X-ray absorption or photoelectron signal at the beamline to define the cluster density on the substrate. Usually the cluster spot has a diameter of about 3 mm and the amount of clusters deposited is determined by the integration of the deposition current. In the example of figure 2.8 a charge of 8.7×10^{-9} C was accumulated this corresponds to 5.4×10^{10} clusters or 1.3×10^{12} atoms. With this quantity of deposited atoms and a cluster spot radius on the substrate of 3 mm (See figure 2.11) a typical coverage density of 2×10^{13} atoms per cm^2 is estimated. An area of $a_0 \cdot a_0$ contains two silicon atoms ($a_0 = 543$ pm is the lattice constant of silicon, that adopts the diamond cubic crystal structure). That means one monolayer of silicon contains 7×10^{14} atoms per cm^2 and on the

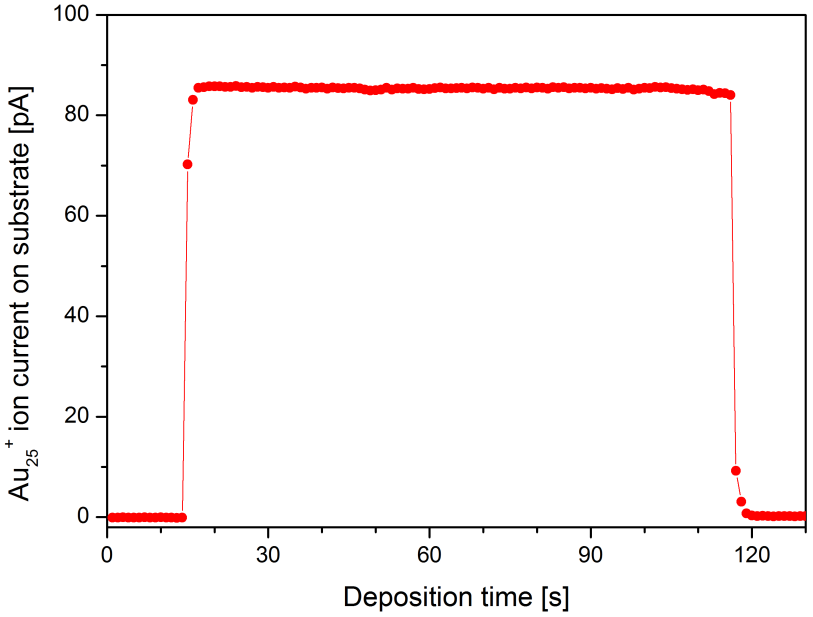

Figure 2.8: *Recorded deposition current of* Au_{25}^{+}. *As seen by the constant ion current during deposition the cluster source can be operated quite stable. Within two minutes clusters with a total number of* 1.3×10^{12} *atoms are deposited softly onto the sample.*

substrate an atomic density of $\approx 3\%$ of a silicon monolayer is estimated.

Ion beam monitor

To quantify the cluster spot size behind the last lens element the deposition chamber is equipped with a spatially resolving ion beam monitor. The ion beam monitor consists of a dual micro-channel plate detector in a chevron configuration including a phosphor (P43) screen. The detector is placed immediately behind the sample holder. After removing the sample the cluster beam is projected onto the channel plate by a high attracting potential. The dual channel plate assembly is biased by a voltage of about -1300 V. The rear is grounded to earth potential and between the rear of the channel plate and the phosphor screen a voltage of 3800 V is applied (figure 2.9). The electron image on the phosphor screen is taken by a video camera which is connected either to a monitor or a computer with frame grabber card.

Figure 2.10 shows the a video image of the projected cluster beam. The spot size can be varied by tuning the last two lenses of the deceleration optics (figure 2.7). A three dimensional image of the same cluster spot is shown in figure 2.11. From both figures a cluster spot diameter of approximate 4 mm is obvious. The weak

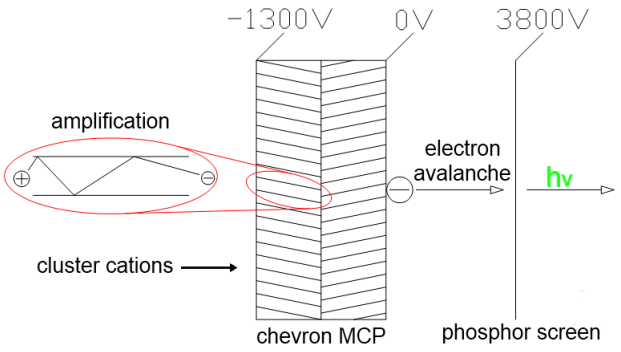

Figure 2.9: *The micro-channel plate/phosphor screen assembly for measuring the deposition spot size. The MCP consists of various channels with 10 µm in diameter and 12 µm distance from each other. Due to the chevron configuration the gain is increased from* 10^3 *to* 10^6 *but the resolution is slightly decreased because the amplified electrons from the first channel plate are distributed over a few channels from the second channel plate. After amplification the electron avalanche is accelerated onto the phosphor screen to make it optically visible.*

reflection of the MCP frame holder (diameter 20 mm) visible in figure 2.10 serves as a scale for calculating the cluster spot diameter. For the spot in figure 2.10 and 2.11 a voltage of -80 V and -700 V has been applied to the last (DC2) and third but last (D3) deceleration lens, respectively. For the deposition spots shown in figure 2.12 the voltage of the last deceleration lens has been varied. With a higher voltage on the last lens (-120 V figure 2.12 a) the cluster spot diameter can be increased, whereas at lower voltage (-40 V figure 2.12 b) the spot diameter is decreased.

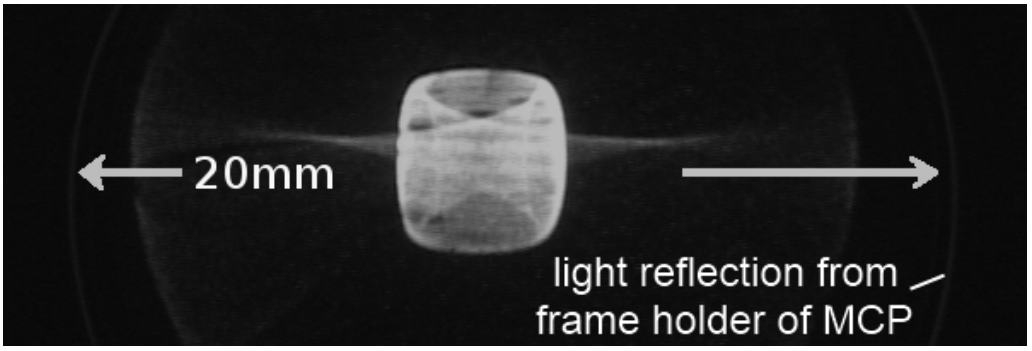

Figure 2.10: *Spatial distribution of the cluster deposition spot as recorded with a CMOS camera. Due to the weakly visible metal frame of the MCP holder (diameter 20 mm) a scale is available on every picture. The diameter of the cluster spot is approximate 4 mm.*

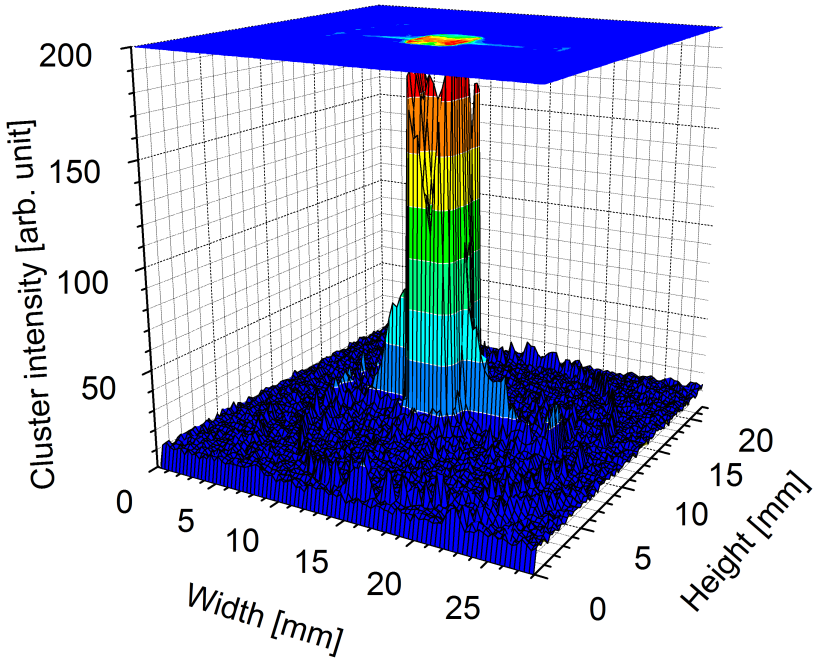

Figure 2.11: *Spatially resolved cluster deposition image monitored by a MCP/CMOS assembly.*

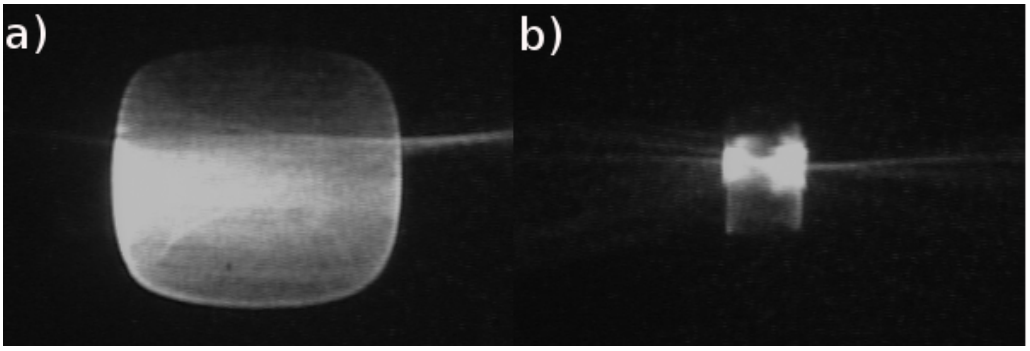

Figure 2.12: *By the use of the deceleration optics a) an increased (-120 V applied to the last lens) and b) a decreased (-40 V applied to the last lens) cluster deposition spot. The scale is the same as in figure 2.10.*

2.1.5 Cluster size optimization

There are several parameters which affect the cluster mass distribution and cluster intensity. These parameters are not really independent of each other. That means if one parameter is chanced the others should be checked to get an even better performance. Helium and argon are dosed by two gas flow controllers. The gas flow can be varied between 0 and 200 sccm (3.6 mbar·l/s). The temperature of the aggregation tube is cooled down to liquid nitrogen (LN_2) temperature and kept

stable. To vary the dwell time of the cluster gas mixture in the aggregation tube one can change the gas flow or vary the aggregation length. The minimal distance between the magnetron head and the nozzle is 2.5 cm and the maximum distance is 27.5 cm. The magnetron power affects the amount of vaporised target material. The magnetron is controlled either in the "current-mode" or in the "power-stabilising" mode. For different target materials of course the parameters usually differ. For example, much more power is necessary to vaporise silicon compared to copper due to different sputter yields [24]. The production of carbon clusters is hardly ever possible due to the very low sputter yield of carbon (0.1 with 300 eV argon ions, the sputter yields of transition metals are 10 to 20 times higher). The silver mass spectrum in figure 2.4 has been recorded with the following parameters (table 2.12).

Temperature at nozzle	-152.5 °C
Power	268 V $\times$ 0.13 A
Aggregation length	9.5 cm
Argon flow	50 sccm
Helium flow	0 sccm
Pressure aggregation tube	4.1×10^{-1} mbar
Pressure 1st skimmer chamber	7.5×10^{-4} mbar

Table 2.12: *Cluster source parameters which have been used for generating the silver mass spectrum shown in figure 2.4.*

2.1.6 UHV-suitcase and EXAFS chamber

After deposition the cluster covered samples are transferred either to a mobile UHV-suitcase (figure 2.13) or to a portable EXAFS chamber (figure 2.14). For photoelectron and Auger spectroscopy the samples are transferred to the UHV suitcase and for EXAFS the samples are transferred to the EXAFS chamber. With the help of a wobble stick the samples are inserted into a particular slot of the multiple-slot magazine, which is connected to the transfer rod (Ferrovac) of the UHV-suitcase. The silicon substrate with a dimension of $\approx$ 1 x 1 cm^2 is glued with an electrically conductive silver two-component adhesive to Omicron stainless steel sample plates. During transport the UHV-suitcase is solely pumped by a battery-powered ion getter pump (24 V). The pressure during transport keeps in the low 10^{-9} mbar range. The height of the UHV-suitcase is adjustable with a hand wheel so that it can be

connected to several beamline end stations at Bessy II. The UHV suitcase was used with end stations at beamline UE52 PGM, UE56-2 PGM1 and the Optics beamline.

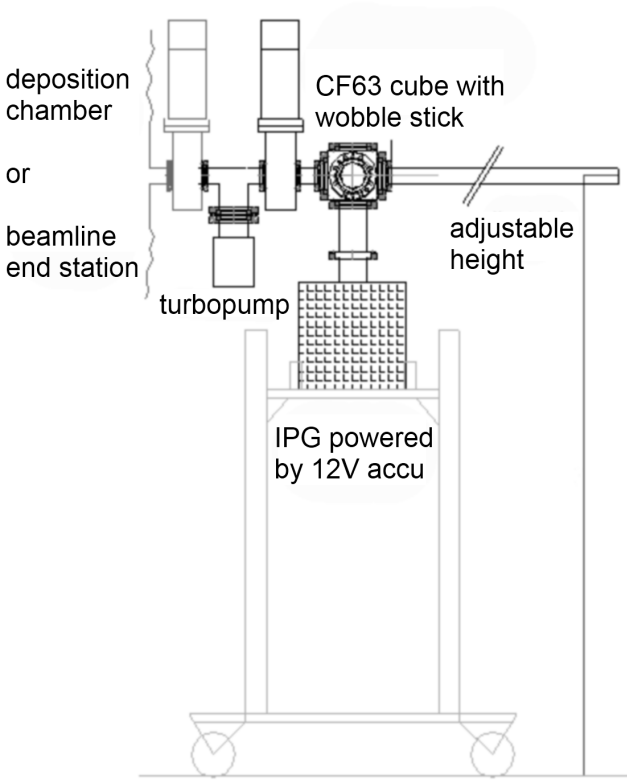

Figure 2.13: *Sketch of the UHV-suitcase for transferring the cluster covered samples under UHV conditions.*

For the measurements at beamline KMC-2 a new portable EXAFS chamber was constructed during this thesis. Usually hard X-ray EXAFS measurements at KMC-2 are made with the samples exposed to air. As the clusters itself can oxidise when they are exposed to air [25] a portable UHV vacuum chamber is necessary at the KMC-2 beamline for cluster measurements.

The main part of the EXAFS chamber (see figure 2.14) is a CF35 cube with an additional CF16 port. The sample holder is connected to the lower CF35 flange in that way that the sample surface is exactly positioned in the centre of the cube. A 10 cm $\times$ 10 cm stainless steel plate is connected to this flange to fix the whole chamber to the motorised sample holder in the hutch at the end of beamline KMC-2. The upper CF35 flange is connected to a gate valve. This valve allows for the sample transfer between deposition chamber and EXAFS chamber. Two CF35 beryllium windows are installed perpendicular to the sample surface. Beryllium is used because

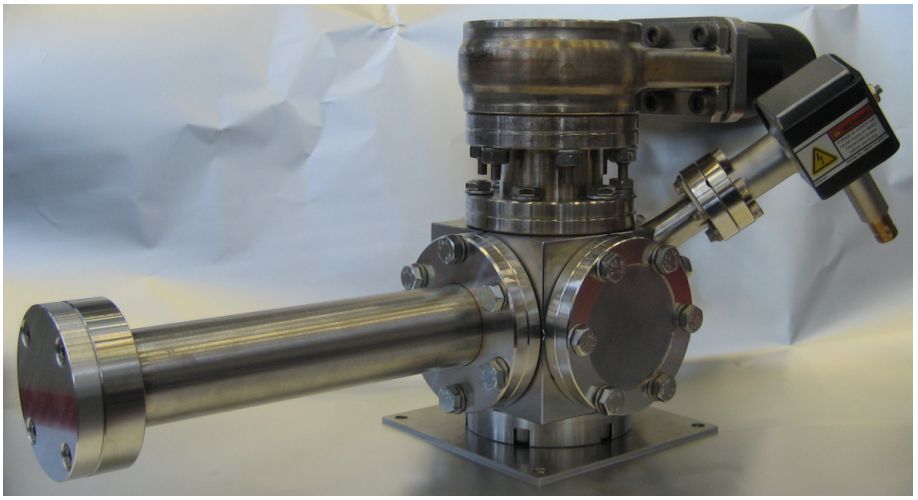

Figure 2.14: *Picture of the new EXAFS chamber. The X-ray fluorescence detector is connected to the vacuum tube to the left (detector not shown). Pumped by a small ion getter pump the pressure is kept at about* 10^{-6} *mbar.*

of its low absorption coefficient for hard X-rays. The beryllium has a thickness of 180 μm. In the desired photon energy range (copper K-edge 9 keV - 10 keV) the transmittance is above 95% [26]. Through the "front" beryllium window the X-ray beam shines onto the sample. Whereas the "back" beryllium window transmits the reflected beam to a "simple" additional photon detector behind the EXAFS chamber. By this signal the sample together with the whole vacuum chamber is adjusted into the X-ray beam. The Röntec x-flash 1201 is an energy dispersive X-ray fluorescence detector based on the silicon drift principle (SDD silicon drift detector). The resolution (FWHM) is below 150 eV at 5.9 keV (manganese k-alpha). The CF35 flange on the right side is closed with an ordinary window which is needed for samlpe transfer. To keep the vacuum in the chamber after disconnection from the sample tranfer cross and during transport and measurement a 3 l/s ion getter pump is connected to the CF16 flange. The power supply of this pump is also equipped with an electrical switch to change between mains operation and battery operation. Due to the fact that the X-ray detector is just sealed via an o-ring the pressure in the EXFAS chamber is about 10^{-6} mbar. This is obviously good enough to not oxidise the clusters as proven by XPS measurements.

2.2 Synchrotron light facility

X-ray spectroscopy experiments of deposited clusters were performed at the synchrotron light facility Bessy II in Berlin. Bessy II is a third generation light source for soft X-rays. The storage ring has a circumference of 240 m with a total ring

current of 300 mA in the multi bunch mode and an operation energy of 1.7 GeV.

Synchrotron radiation has several advantage over other X-ray sources such as X-ray tubes or gas discharge lamps. Not only that synchrotron radiation is a tunable X-ray light source it is also highly polarised and brilliant. The high photon flux (10^{12} photons per second behind monochromator) makes it ideal to study dilute samples like deposited and also free clusters. Because of the tunable photon energy it is possible to measure absorption spectra (EXAFS and XANES). Moreover it is feasible to measure photoelectron spectroscopy with a high X-ray absorption cross section (1-10 Mbarn for soft X-rays) for the desired core levels or resonant and photon energy dependent Auger spectroscopy. With elliptically polarizing undulators it is possible to measure X-ray magnetic circular dichroism on solids and clusters.

Synchrotron radiation has its origin in the deflection of charged relativistic particles in a magnetic field. The deflection can occur in dipole magnets (1st and 2nd generation of light source) or via insertion devices called undulators (3rd generation of light source) or wigglers. The 4th generation of light sources are FEL (free electron laser) and ERL (energy recovery linear accelerator). Dipole magnets bend the electron's path and X-rays are emitted tangential to the electron trajectory. The result is a continuous and broad energy distribution. Undulators and wigglers are arrays of dipole magnets with alternating polarity. The difference between undulators and wigglers is the period length and the magnetic flux density of the dipole magnets. In both cases the electrons are forced on a periodical path. The electron motion is characterized by the deflection parameter

$$K = \frac{eB_0\lambda_u}{2\pi m_e c} \tag{2.4}$$

where e is the unit charge, B_0 the maximum magnetic flux density, λ_u the undulator period, m_e the electron mass and c the speed of light. For $K \leq 1$ the insertion device is referred to as an undulator where the radiation from the various magnet periods exhibit strong interference phenomena whereas for $K \gg 1$ the insertion device is referred to as a wiggler where interference effects are less important. The wiggling electrons of insertion devices emit synchrotron light in their average propagation direction. In undulators the emitted radiation adds coherently and the X-ray intensity is proportional to N^2 (N is the number of magnet periods of the insertion device). In a wiggler the emitted radiation adds incoherently and the X-ray intensity is just proportional to 2N. The result is a continuous energy spectrum for the wiggler and a line spectrum for the undulator [27].

2.2.1 Beamlines and end stations

Mass selected deposited clusters were explored at four different beamlines at Bessy II [28]. Beamline UE52 PGM is equipped with a permanent XPS end station. The Optics Beamline is combined with the permanent XPS end station SurICat (Surface Investigation and Catalysis). At beamline UE56-2 PGM1 the moveable station iDEEAA (Instrument for Direct Electron Energy and Angular Analysis) is used as XPS chamber. When choosing a beamline the desired photon energy range and resolution, the polarisation and the existence of an appropriate end station has to be considered. For the X-ray photoelectron spectroscopy and Auger measurements the end stations had to be compatible with standard omicron sample plates and a load lock for the UHV suitcase was needed. The EXAFS K-edge measurements of copper were performed at beamline KMC-2. To apply in situ EXAFS measurements on deposited clusters a new portable vacuum chamber was built and installed into the beamline hutch.

Beamlines

Beamline UE52 PGM consists of the UE52 undulator. The undulator UE52 is an elliptical undulator with a period length of 52 mm. UE56-2 PGM1 also consists of an elliptical undulator but provides a period length of 56 mm. Both undulator sources can deliver linearly polarised light as well as circularly polarised light. The Optics Beamline is a "simple" bending magnet beamline located behind the dipole magnet D81. All three beamlines are equipped with a plane grating monochromator (PGM) [29]. A plane grating monochromator consists of a plane mirror and a plane grating. The mirror reflects the light from the undulator onto one of the changeable gratings. To get the grating equation for the constant focal distance one need the c_{ff}-value (fix-focus constant) which is defined as

$$\frac{cos\beta}{cos\alpha} = c_{ff} = constant \tag{2.5}$$

where β and α are the emergent and incidence angles of the reflection, respectively. A high c_{ff}-value yields to higher resolution whereas a higher flux is achieved by a low c_{ff}-value. With the grating equation

$$m \cdot \lambda = d(sin\alpha + sin\beta) \tag{2.6}$$

where m is the reflection order and λ is the lights wavelength. Using the algebraic identity

$$sin\lambda = \sqrt{1 - cos^2\lambda} \tag{2.7}$$

the grating equation for the constant focal distance results

$$m \cdot \lambda = d \cdot (\sqrt{1 - \frac{cos^2\beta}{c_{ff}}} + sin\beta) \tag{2.8}$$

where d is the grating constant. Equation 2.8 can be transposed [27] into

$$1 - (\frac{m \cdot \lambda}{d} - sin\beta)^2 = \frac{cos^2\beta}{c_{ff}^2} \tag{2.9}$$

Because of the fixed focal distance, no matter of the chosen photon energy, the exit slit does not have to be moved. Plane grating monochromators exhibit a high achievable energy resolution, a good suppression of higher grating orders and a high submitted photon flux from very low to high photon energies [30].

The final device which belongs to the monochromator is the exit slit. With the help of the exit slit the dispersed light will arrive at the focal point (i.e. sample position) with different spectral resolution. Typical values for the exit slit width are 0 - 1000 μm.

Figure 2.15 shows the photon flux of the Optics Beamline for two different gratings (360 and 1228 l/mm). The grating with 1228 lines per millimetre covers a broad photon energy range with high resolution. At low photon energy the grating with 360 lines per millimetre has a higher photon flux. On the basis of figure 2.15 it is obvious that the core level spectra of silver (E_B=368.2 eV) and gold (E_B=84 eV) where recorded with the 360 lines per millimetre grating and the core level spectra of copper (E_B=932.5 eV) were recorded with the 1228 lines per millimetre grating to get a photon flux as high as possible at the particular photo ionization cross section ($\sigma_{Cu2p}(1000\ eV) \approx 1$ Mbarn, $\sigma_{Ag3d}(450\ eV) \approx 4$ Mbarn, $\sigma_{Au4f}(300\ eV) = 5.5$ Mbarn [31]).

Beamline KMC-2 [32] is a beamline especially used for EXAFS and XANES in air in the energy range of 4 keV - 15 keV. The beamline is located behind the dipole D92. A double-crystal monochromator with two graded SiGe 111 crystals is used as monochromator [33]. The beam intensity is stabilized with an acccuracy of 0.3 % by a MOSTAB electronics. A crystal monochromator operates through the diffraction of X-rays at a crystal lattice according to Bragg's law. Constructive intereference between X-rays only occurs if the path difference is a multiple of the wavelength (λ).

$$n \cdot \lambda = 2 \cdot d \cdot \sin\Theta \tag{2.10}$$

Θ is the angle between the X-rays and the crystal plane and d is the distance between two crystal planes.

The measurement position is less than one metre away from the last beamline element (a kapton or beryllium window). In the energy range for copper K-edge

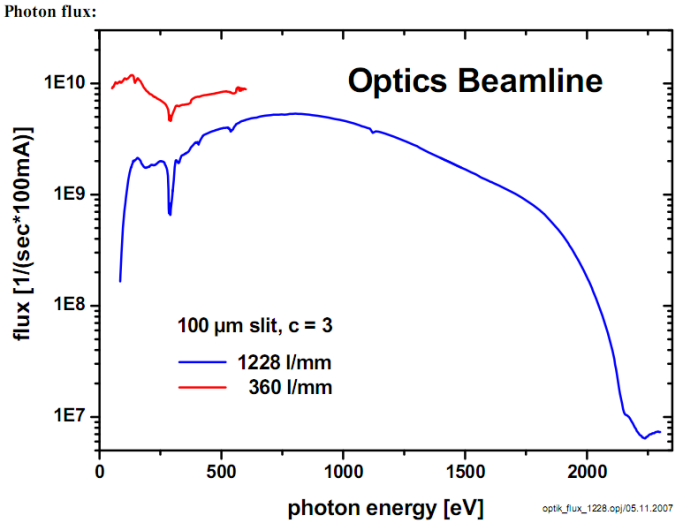

Figure 2.15: *The photon flux as a function of the photon energy for two different gratings.*

EXAFS measurements (9 keV - 10 keV) the beamline delivers a photon flux of 10^{10} photons/s per 100 mA ring current. The absorption of X-rays in matter is described by the Beer-Lambert law. The intensity of light after travelling a matter with the attenuation coefficient μ for a distance d is given by

$$I(d) = I_0 \cdot e^{-\mu \cdot d} \tag{2.11}$$

The ratio of $I(d)$ to I_0 for 80 cm of air ($\mu_{air}\,[h\nu = 10keV] = 0.006\ cm^{-1}$ [34]) is 0.62. That means at the sample position is still more than 60% of the initial X-ray intensity.

End stations

The end stations used for XPS and Auger are all essentially equal. All consist of three independent vacuum chambers separated by UHV gate valves.

The first chamber serves as a load lock and sample preparation chamber. Usually the UHV-suitcase is connected to the load lock to transfer the cluster samples from the mobile UHV-suitcase to the end station. The load lock can be equipped with an evaporator and a film thickness monitor to prepare fresh and clean bulk films to compare spectra of solid and cluster under the same conditions. Also an UHV-needle valve is available at the load lock to expose the samples to reactive gases. The pressure in the first chamber is below 10^{-8} mbar.

The second chamber is the main preparation chamber. To this chamber the main manipulator is connected on which the samples are located during measurement. With a needle valve for argon dosing and a sputter gun it is possible to clean

sample surfaces. For example single crystals for solid measurements. Because the end station at UE52 PGM has no load lock the UHV-suitcase is connected to this chamber. The pressure in this chamber is about 10^{-9} mbar.

The third chamber is the analyser chamber which is equipped with the electron analyser which measures the kinetic energy of the photoelectrons. Also other detectors can be connected to the analyser chamber like partial yield detectors or X-ray fluorescence detectors. In the same plane as the electron detector the beamline is placed. Other light sources that can be connected are X-ray tubes for XPS and helium lamps for UPS. The pressure in this chamber is in the low 10^{-10} mbar range.

The end stations at the undulator beamlines UE52 PGM and UE56-2 PGM1 are equipped with the hemispherical electron analyser Scienta R4000 which has a 200 mm mean radius. SurICat at the Optics Beamline is equipped with the hemispherical electron analyser Scienta SES100 with a mean radius of 100 mm. The resolution ΔE of such hemispherical analyser is given by

$$\frac{E_{pass}}{\Delta E} = \frac{2 \cdot R}{slit} \tag{2.12}$$

where E_{pass} is the pass energy, R is the mean radius of the hemispheres and *slit* is the entrance slit width of the electron analyser. Thus using the same parameters (E_{pass} and entrance slit) the R4000 has a twice better resolution than the SES100. A larger pass energy and a larger slit size increases the electron signal but the resolution is decreasing in the same way.

A hemispherical electron analyser consists of a system of electron lenses, the entrance slit, two concentric hemispheres and an electron detector. The electrons coming from the sample are focused onto the entrance slit by the electrostatic lenses. The voltage applied between the two hemispheres is equivalent to the pass energy. Only electrons with the same kinetic energy like the pass energy can pass the analyser. A chosen electron kinetic energy interval of interest is scanned by changing the voltages of the electrostatic lenses. During measurement the electrons are accelerated or retarded and a spectrum can be recorded. For example the gold $4f_{7/2}$ (E_B=84 eV, $\phi = 5.1\ eV$) photoelectrons excited with a photon energy of 250 eV have to be retarded by 140.9 eV to pass the analyser with a pass energy of 20 eV.

$$E_{pass} = E_{h\nu} - E_B - \phi - U_{retard} \tag{2.13}$$

$$20\ eV = 250\ eV - 84\ eV - 5.1\ eV - 140.9\ eV \tag{2.14}$$

After passing the analyser the electrons are detected by the installed detector for instance a system of a microchannel plate, a phosphor screen and a camera.

Figure 2.16 shows the moveable end station iDEEAA which was used at beamline UE56-2 PGM1. The end station is equipped with two electron spectrometer, which

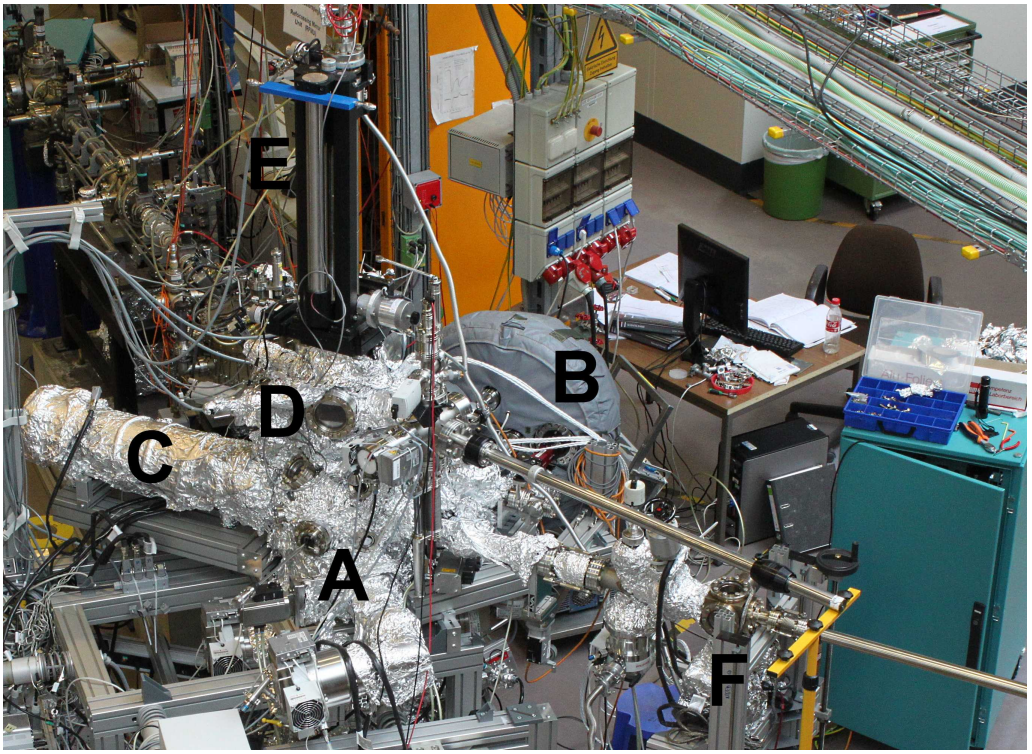

Figure 2.16: *The moveable end station iDEEAA. To the analyser chamber **A** a hemispherical electron spectrometer **B** and a time-of-flight electron spectrometer **C** is connected. On top of the analyser chamber the preparation chamber **D** is located, to which the main manipulator **E** is connected. The UHV-suitcase **F** is connected to the analyser chamber. In the upper left corner the beamline is visible.*

are connected to the analyser chamber **A**, the hemispherical electron spectrometer Scienta R4000 **B** and the time-of-flight spectrometer Scienta ARTOF 10k (Angel Resolved Time Of Flight) **C**. The beamline, which is visible in the upper left corner, and both spectrometer are located in one plane with an included angle between the beamline and both spectrometer of 45 °. On top of the analyser chamber is the preparation chamber **D**, to which the main manipulator **E** and a load lock is connected. The UHV-suitcase **F** is connected directly to the analyser chamber. Right from the CF63 cube of the UHV-suitcase, where the samples are located during transport, the transfer rod is visible. With the help of the transfer rod the samples are transferred into the analyser chamber and after that transferred onto the main manipulator by the use of a wobble stick (to the left of the **A**).

3 X-ray spectroscopy techniques

X-ray photoelectron spectroscopy (XPS), X-ray absorption spectroscopy (XAS) and Auger electron spectroscopy (AES) are element specific techniques for the investigation of the electronic structure of atoms, molecules and bulk materials. During this work all these techniques have been applied to investigate the evolution of the electronic structure of mass selected deposited clusters.

3.1 X-ray photoelectron spectroscopy (XPS)

X-ray photoelectron spectroscopy is based on the photoelectric effect which was first observed by Heinrich Hertz in 1887 [35] and was explained in 1905 by Einstein [36]. The principle of photoelectron spectroscopy is to shine highly monochromatic light onto the sample and to measure the kinetic energy distribution of the escaping photoelectrons. The measured kinetic energy is given by

$$E_{kin} = E_{h\nu} - E_B - \phi_{analyser} \tag{3.1}$$

where E_{kin} is the kinetic energy of the photoelectron measured by the electron analyser, $E_{h\nu}$ is the photon energy, E_B is the binding energy of the given electron relative to the Fermi level and $\phi_{analyser}$ is the work function of the electron analyser. It is important to make clear that the kinetic energy of the photoelectron measured by the electron analyser could be different from the kinetic energy of the photoelectron just after leaving the sample. The latter is given by

$$E^*_{kin} = E_{h\nu} - E_B - \phi_{sample} \tag{3.2}$$

with the samples work function ϕ_{sample}. After entering the spectrometer the energy of the photoelectron is increased or decreased by the contact potential between sample and spectrometer ($\phi_{sample} - \phi_{analyser}$) in the case of a grounded sample (figure 3.1). For the determination of the binding energy only the work function of the spectrometer is needed because the kinetic energy measured by the electron analyser refers to the work function of the spectrometer. The work function of the spectrometer can be determined by the position of the Fermi edge in the photoelectron spectrum (E^{max}_{kin}). If the photon energy is exactly known the work function of the spectrometer is given by

$$\phi_{analyser} = E_{h\nu} - E^{max}_{kin} \tag{3.3}$$

In the case of $\phi_{sample} > \phi_{analyser}$ the work function of the sample can be calculated with the help of the spectrum's width $W = E^{max}_{kin} - E^{min}_{kin}$. In that case the photoelectron spectrum starts at an E^{min}_{kin} greater than zero. In the case of $\phi_{sample} \leq \phi_{analyser}$

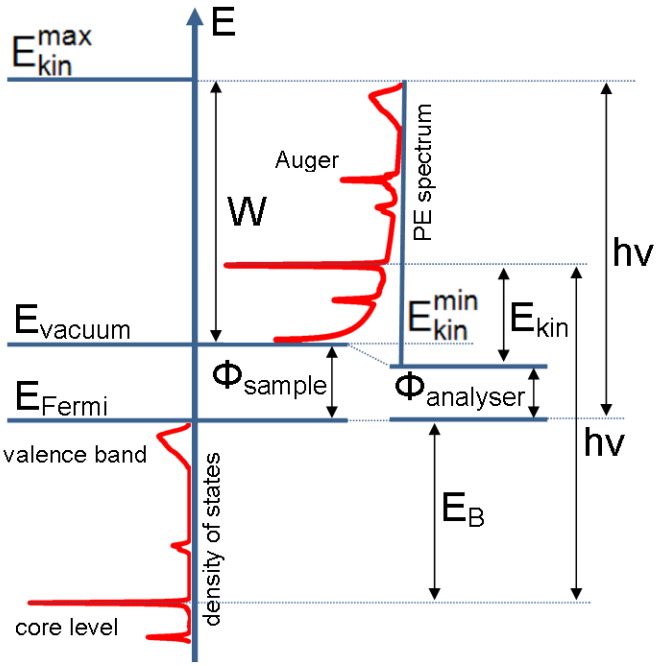

Figure 3.1: *Overview of the involved energies during PES in the case of a grounded sample. The Fermi levels of the sample and analyser are aligned due to the grounding.*

the sample must be biased. In both cases the work function of the sample is given by

$$\phi_{sample} = E_{h\nu} - W \tag{3.4}$$

Usually the line shape of XPS peaks can be well fitted with a Voigt profile, i.e. a convolution of a Gauss profile and a Lorentz profile. The Lorentzian width results from the natural lifetime of the core hole, whereas the Gaussian width results mainly from the experimental broadening. The latter is the resolution of the monochromator and the electron analyser. For metals often a skew line shape is observed as explained by S. Doniach and M. Sunjic [37]. The spectral function of the core hole is not Lorentz-like. It tails off on the low kinetic energy side due to the energy dependent creation of low energy conduction electron-hole pairs. The skewness is quantified by the singularity index alpha of the Doniach-Sunjic function. A Doniach-Sunjic profile with a singularity index $\alpha = 0$ is a Lorentz profile. Therefore the Voigt profile results from a convolution of a Gauss profile and a Doniach-Sunjic profile.

The peak width of the XPS peak is usually defined as the full width at half maximum (FWHM), which is determined by the experimental and natural lifetime

width. A good approximation is given by [38]

$$\Delta E_{Voigt} \approx 0.6346 \cdot \Delta E_{Lorentz} + \sqrt{0.2166 \cdot \Delta E_{Lorentz}^2 + \Delta E_{Gauss}^2} \tag{3.5}$$

where ΔE_{Gauss} (experimental resolution) is the convolution of the monochromator resolution and electron analyser resolution.

$$\Delta E_{Gauss}^2 = \Delta E_{monochromator}^2 + \Delta E_{analyser}^2 \tag{3.6}$$

The typical XPS background is caused by inelastically scattered electrons. In the simplest case the background can be approximated by a line or a polynomial function. In more challenging cases a Shirley background [39] or a Tougaard background [40] is advisable for peak analysis.

In this thesis the core hole spectra were fitted with the fitting software FitXPS [41].

3.2 Auger electron spectroscopy (AES)

After creation of a core hole by photoionisation the atom is left in a core ionised state, in case of resonant photoabsorption a neutral core excited electron-hole state is produced. The core hole is filled by an electron of a higher atomic level, i.e. by an electron of lower binding energy. This transition is accompanied either by the emission of a photon or the emission of another electron. The latter case is the Auger effect, a non-radiative core hole relaxation process. The element specific energy of the Auger electron or photon is given by the energy difference between the initial and final state. Both processes compete with each other. For lighter elements the Auger effect dominates over X-ray emission, while X-ray emission is more probable for elements with higher atomic number Z. The ratio between Auger and X-ray emission depends on the absorption edge. For the K-edge the ratio is one at Z $\approx$ 30. Whereas for the L_3-edge the ratio is one at Z $\approx$ 90 [42].

The kinetic energy of the Auger electron for a normal Auger process, i.e. when using a photon energy far above the threshold, does not depend on the photon energy. The Auger kinetic energy just depends on the initial and final state. This is one difference between Auger and photoemission peaks in an electron spectrum, the latter shift with the photon energy. The Auger kinetic energy minus the work function for the $L_3M_4M_5$ transition is given by

$$E_{kin}^{Auger} = E_{L_3} - E_{M_4} - E_{M_5} - E_{Coulomb} \tag{3.7}$$

where E_L, E_{M_4} and E_{M_5} are the binding energies relative to the Fermi level of the involved atomic levels. $E_{Coulomb}$ accounts for the Coulomb interaction of the double ionised Auger final state.

When exciting the atom to a resonant bound state below threshold, the subsequent non-radiative relaxation process is called resonant Auger (RAS - resonant Auger spectroscopy) [43]. Such a state can decay in two ways. In case of a participator decay, the core hole is filled by the excited electron and a valence electron is ejected into the continuum. The atom is left in a one hole valence final state (photoionisation final state). In the other case, the spectator decay, the core hole is filled by a valence electron and another valence electron of the same orbital leaves the atom. Now the atom is left in a two hole, one electron final state (shake-up final state).

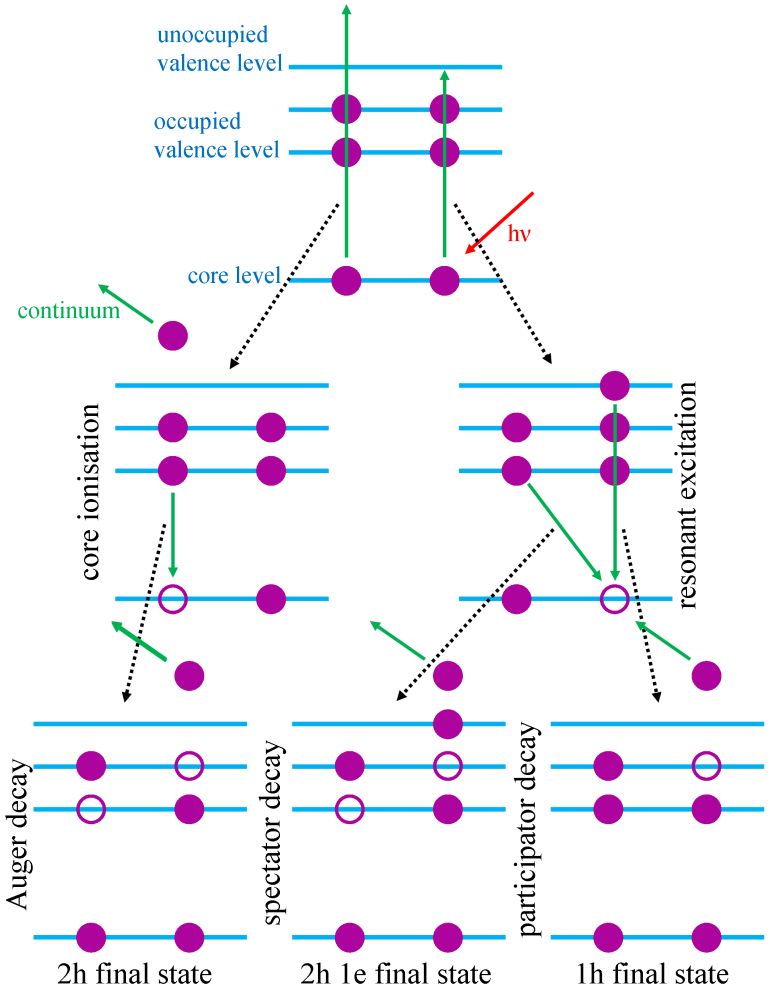

Figure 3.2: *Auger core hole decay diagram. The diagram starts with an atom in the ground state. Due to the interaction with a photon of appropriate energy the atom is promoted either in a core ionised Auger initial state or in a resonant core-excited state. The core ionised state relaxes through the normal Auger decay into a two hole final state. The resonant excited state can relax by a spectator or participator decay ending up with a two hole one electron and one electron final state, respectively.*

A special case of the Auger process is the so-called Coster-Kronig transition [44]. In this case the core hole is filled by an electron of a higher sub level of the same main shell. For instance the $L_2L_3M_{45}$ Coster-Kronig transition where the L_2 core hole is filled by an electron of the L_3 shell and one M_{45} electron is ejected into the continuum. The latter transition shortens the copper $2p_{1/2}$ core hole lifetime which results in a broader linewidth compared to the $2p_{3/2}$ final state [45]. A super Coster-Kronig transition is present when all participating electrons origin from the same main shell.

3.3 Extended X-ray absorption fine structure (EXAFS)

X-ray absorption spectroscopy (XAS) is the measurement of the absorption coefficient near and above an absorption edge as a function of the photon energy. The absorption edge is the sharp rise of the absorption coefficient at the ionisation threshold energy due to the transition of core electrons into unoccupied valence states. Beyond the absorption edge the absorption coefficient does not monotonically decrease with the photon energy but exhibits the X-ray absorption fine structure (XAFS). An X-ray absorption spectrum is typically divided into two regions. The X-ray absorption near edge spectroscopy (XANES), which is also called near edge X-ray absorption fine structure (NEXAFS), with some ten eV above the absorption edge and the EXAFS region well above the absorption edge.

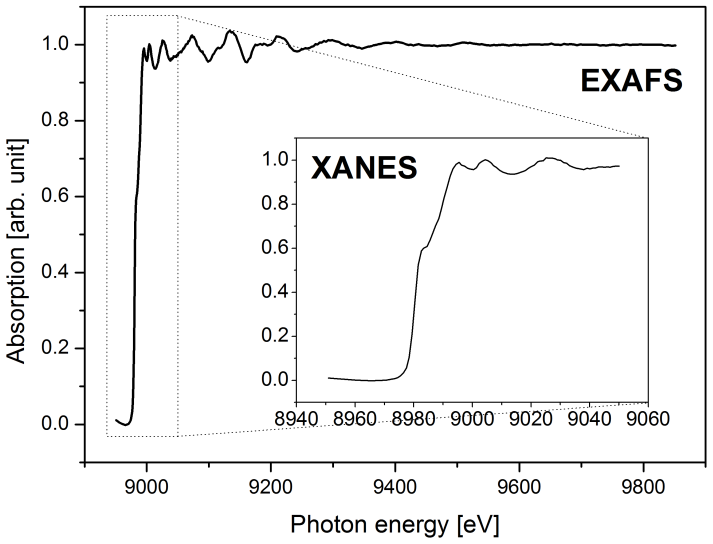

Figure 3.3: *EXAFS and XANES K-edge spectra of copper bulk. The XANES region extends some ten eV above the absorption edge whereas the EXAFS region extends several hundred eV above the absorption edge.*

XANES is sensitive to oxidation state and coordination chemistry of the absorbing atom while EXAFS gives information about the distances, coordination number and species of the neighbouring atoms [46]. Since the absorption edge is related to a transition of a core electron to an unoccupied state, the near edge region is sensitive to the unoccupied density of states.

The origin of the oscillatory structure can be explained by considering the photoelectron as a matter wave with the de Broglie wavelength λ

$$\lambda = \frac{h}{p} = \frac{h}{\sqrt{2m_e(E_{h\nu} - E_{edge})}} \tag{3.8}$$

or, because the EXAFS function is a function of k, the wavenumber k

$$k = \frac{2\pi}{\lambda} = \sqrt{\frac{2m_e(E_{h\nu} - E_{edge})}{\hbar^2}} \tag{3.9}$$

with the electron mass m_e and h and $\hbar$ the Planck constant and reduced Planck constant, respectively. The electrons of the atoms surrounding the photoionised atom can backscatter the electron waves. The forward propagating and backscattered waves can interfere constructively or destructively, depending on the electrons's wavenumber, i.e. on the photon energy. The alternating constructive and destructive interference modulates the absorption coefficient, causing the XAFS. In the EXAFS region mainly single scattering of the photoelectron occurs whereas XANES is called the multiple scattering region. This is due to the fact that the inelastic mean free path of the photoelectrons in the EXAFS region is just some Ångström. But the slow photoelectrons in the XANES region have an inelastic mean free path of several Ångström. They can scatter with many atoms without losing kinetic energy. The latter makes a quantitative analysis of XANES more difficult compared to EXAFS.

There are in principle two ways to perform XAFS measurements. The first one is to measure in transmission mode. The intensities of the incident and transmitted X-ray beam is measured as a function of the photon energy. This method is preferred for thin and uniform samples. For thick or dilute samples it is preferred to monitor the X-ray fluorescence or the Auger electron yield. Due to the low escape depth of the Auger electrons this technique is very surface sensitive. In fact, a high surface sensitivity can also be achieved with X-ray fluorescence if the X-ray beam has a very grazing incidence on the sample. This technique is known as surface EXAFS (SEXAFS).

4 Experimental results

4.1 X-ray photoelectron spectroscopy of deposited Au_n clusters ($n = 1 - 35$)

Photoelectron spectroscopy (PES) is a well-established and versatile tool to explore the electronic structure of matter. In general it is used to investigate electronic and magnetic properties, chemical and catalytic properties as well as structural aspects. Furthermore PES is a surface sensitive and element specific technique, which is suitable for the analysis of extremely diluted samples such as free molecules, adsorbates and sub-monolayer surfaces. Moreover, highly brilliant synchrotron radiation allows to study spatially separated clusters on a surface with a coverage density down to a few percent of an atomic monolayer.

XPS spectra are usually interpreted in terms of initial and final state effects. Initial state effects are associated with the intrinsic electronic and geometric structure of the cluster whereas final state effects are associated with the creation of the photohole. The cluster-size dependent binding energy shift of free clusters can often be explained by the liquid drop model [47, 48] in which the ionisation potential scales linearly with the inverse cluster radius. This has been verified experimentally for valence ionisation of free mass-selected clusters [49, 50, 51] and recently for shallow core shell photodetachment studies of free mass-selected anionic lead clusters [3, 52]. Deposited clusters, on the other hand, are subject to extra-atomic screening and charge transfer from the support, which can alter the initial and final state of the cluster, respectively. The XPS binding energy of deposited metal clusters has been found to be blue shifted with respect to the solid [16]. This has been explained by the reduced final state screening as a result of the reduced metallic conductivity and, secondly, by the electrostatic charging of the cluster due to retarded neutralisation of the photohole [53, 54].

In general metal clusters on thin oxide films have attracted considerable attention due to their interesting chemical and catalytic properties [4, 5, 6, 55, 56, 57, 58, 59]. In particular small Au clusters have a high potential to be used as new catalysts. To highlight the electronic structure of oxide-supported Au-clusters and the interaction with the support we present a detailed study of the characteristic Au 4f photoemission peak. Several XPS studies on atomic Au islands, nanoparticles and deposited clusters have been done in the past, mainly on rutile, silica or graphite using moderate spectral resolution [12, 53, 60, 61, 62, 63, 64]. Common to all those measurements is a high binding energy shift of the 4f binding energy with respect to the bulk 4f line which is generally interpreted in terms of an electrostatic final state effect. Here we present a synchrotron photoemission study of an extended series of

mass-selected clusters. The cluster results are directly compared to the 4f photoemission spectrum of an evaporated macroscopic Au film. All Measurements have been carried out with an energy resolution below the core hole lifetime broadening of the Au 4f inner shell (≈ 0.3 eV). Our measurements highlight not only a systematic XPS shift as function of size but reveals detailed differences in the line shape and peak width of the supported clusters with respect to the bulk. Moreover our highly resolved measurements on mass selected clusters reveal some XPS intensity at negative binding energies with respect to the bulk peak. A detailed analysis of the $4f_{7/2}$ photoelectron component as function of cluster size unravels different contributions caused by initial and final state effects as well as effects induced by the interaction with the substrate.

A series of gold clusters between Au_1 and Au_{35} has been measured at the undulator beamline UE52-PGM. The clusters have been measured at a photon energy of $h\nu = 250$ eV, i.e. near the photoionisation cross section maximum ($\approx$5 Mbarn [65]), within about one hour measuring time. Additionally a freshly evaporated gold film has been measured with the same experimental conditions for comparison with the clusters. A total Gaussian broadening of $\Delta E_{experiment} = 0.2\ eV$ has been fitted from the bulk peak using a Voigt profile and a natural lifetime broadening of $\Delta E_{Lorentz} = 0.3\ eV$ [66].

The Au 4f photoelectron spectra of Au_2, Au_5, Au_{20} and Au_{30} in comparison to the spectrum of the macroscopic gold film are shown in figure 4.1. A systematic increase of the binding energy with decreasing cluster size is obvious. The peak maximum of the gold $4f_{7/2}$ bulk line is set to the literature value of $E_b = 84$ eV [67] while the cluster peak maxima are calibrated to the bulk value and increase from 84.2 eV to 84.8 eV with decreasing cluster size. Furthermore a pronounced peak broadening is revealed, which rises from 1 to 1.7 eV (FWHM) with decreasing cluster size. With the same experimental conditions the bulk photoemission line shows a width of 0.4 eV. Regardless of an experimental resolution better than the natural lifetime broadening ($\Delta E_{experiment} = 0.2\ eV$) no fine structure is resolved in any of the cluster spectra. Moreover figure 4.1 exhibits that the low binding energy tail of all cluster spectra almost perfectly matches the low binding energy tail of the normalised solid gold surface core level peak (see also figure 4.6 and 4.7). The surface peak of solid gold has a negative surface core level shift of 0.4 eV with respect to the bulk core level peak [66]. The negative surface core level shift is an initial state effect, which is explained by the valence band narrowing of the less coordinated surface atoms. This causes a charge redistribution from 6s to 5d and hence an increased charge density and screening of the core hole. The normalised

surface core level line is shown in figure 4.1 at a binding energy of $E_B = 83.6$ eV with the same life time broadening as the bulk peak [68].

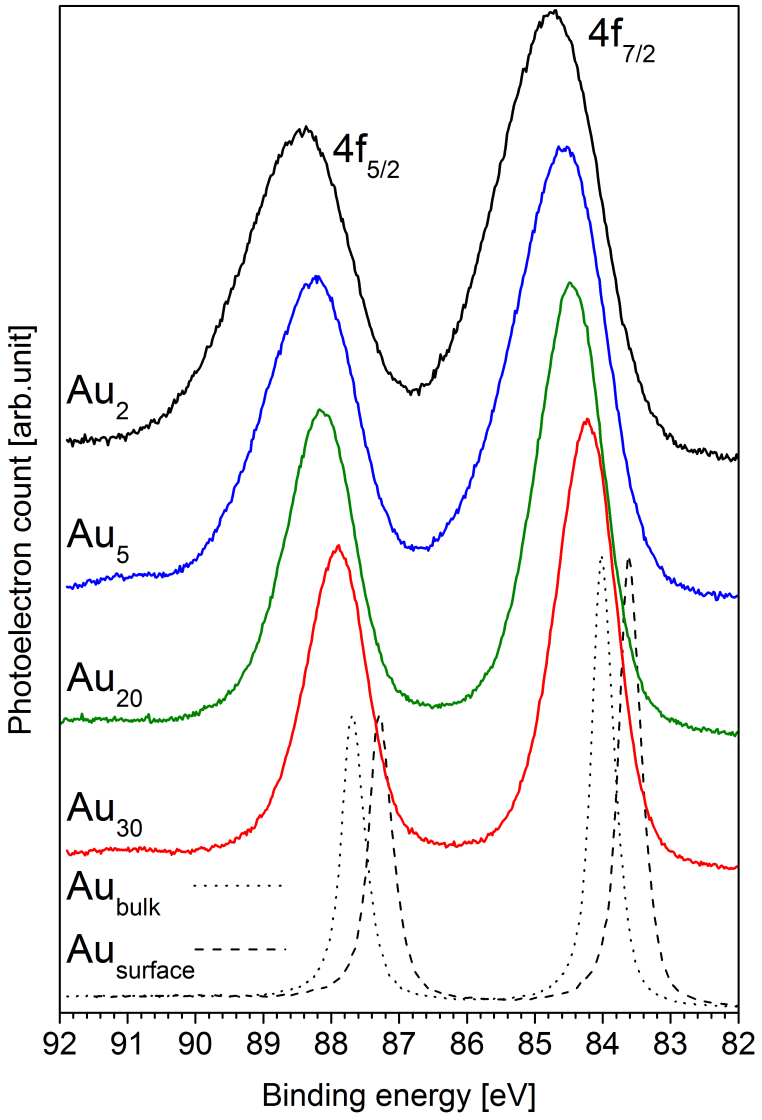

Figure 4.1: *X-ray photoelectron spectra of deposited gold clusters in comparison with the spectrum of a macroscopic gold film recorded with the same experimental conditions. The intensity normalised surface core level peak of solid gold is shown as dashed line. It is shifted by -0.4 eV with respect to the bulk core level peak (dotted line). Note that the low binding energy tail of the clusters match the low binding energy tail of the surface core level peak (see also figure 4.6 and 4.7).*

The systematic increase of the binding energy with decreasing cluster size can be explained by the size dependent electrostatic interaction between the ionised cluster and the escaping photoelectron [53, 54]. The positive charge left on the cluster is

confined by the cluster radius R according to the electrostatic drop model [47, 48]. Therefore it interacts with the escaping photoelectron in contrast to the metallic bulk phase for which the charge is spread to an infinite surface. Within this classical framework the ionisation potential of a spherical metal droplet increases linearly with the inverse cluster radius according to equation 4.1.

$$IP_{cluster} = IP_{bulk} + \alpha \frac{e^2}{4\pi\epsilon_0 R} \tag{4.1}$$

The constant α amounts to 0.5 when the classical electrostatic energy of a metal sphere is considered [69]. Experimentally α has been determined to be smaller than the classical value with values between 0.2 and 0.4 depending on the element of which the cluster is build up [50]. The deviation from the classical value origins mainly from quantum corrections (e.g. electron spillout) and non simple metal behaviour concerning the electronic and geometric structure, which is not considered in the liquid drop model.

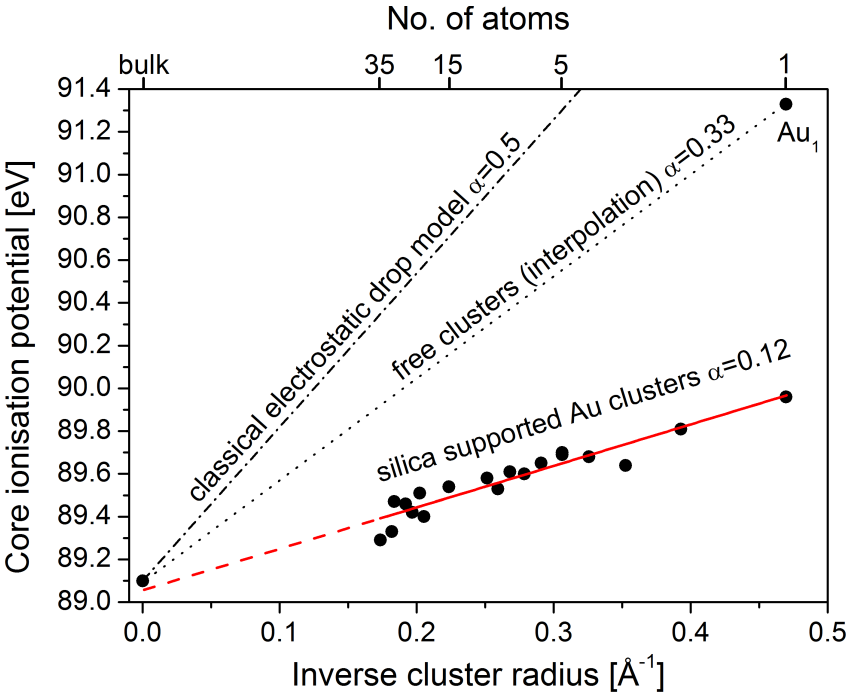

Figure 4.2: *The core ($4f_{7/2}$) ionisation potential (binding energy plus work function of the solid) of deposited gold clusters as a function of the inverse cluster radius. The classical electrostatic drop model for free particles is shown as dash-dotted line. The dotted line shows an interpolation of free neutral gold clusters. Note that the slope of the supported clusters is considerably reduced with respect to free clusters. The gold 4f XPS peak of the free neutral atom has been measured by Patanen et al. [70].*

Figure 4.2 shows the core ionisation potential (equation 4.2) of the silica sup-

ported gold clusters as a function of the inverse cluster radius in comparison with the classical electrostatic drop model ($\alpha = 0.5$) and the core ionisation potential of free gold clusters. By the slope of the interpolated line $\alpha = 0.33$ is determined for free gold clusters. The core ionisation potential line of free gold clusters has been interpolated by the measured ionisation potential of the free gold atom $\mathrm{IP}_{\mathrm{gold\ atom}} = 91.28$ eV [70] and the bulk ionisation potential $\mathrm{IP}_{\mathrm{gold\ bulk}} = 89.1$ eV.

$$IP(4f_{7/2}) = E_B(4f_{7/2}) + \phi_{solid} \tag{4.2}$$

As obvious from the fit of the experimental data of the supported clusters (red line) a linear dependence of the core ionisation potential of the supported clusters versus the inverse cluster radius is apparent. The linear dependence illustrates the validity of the liquid drop model for deposited gold clusters, which means, that the core hole is delocalised over the surface of the cluster on a timescale relevant to photoemission as originally discussed by Wertheim *et al.* [53], Cheung [54, 71] and DiCenzo *et al.* [72]. These authors used the final state charge approach, i.e. the interaction of the escaping photoelectron with the unit charge left on the cluster surface, to explain the high binding energy shift of supported gold nano-islands. However the slope of the supported cluster data is much smaller with respect to free clusters and also to the classical electrostatic drop model. From the straight line fits $\alpha = 0.12$ and $\alpha = 0.33$ are determined for the supported and free gold clusters, respectively. Hence the supported gold clusters exhibit a smaller size dependent ESCA shift than free gold clusters.

The notable reduced XPS shift of supported gold clusters with respect to free gold clusters is attributed to the interaction of the clusters with the substrate. In contrast to photoionised free clusters supported clusters are subject to extra-atomic charge transfer by the substrate after photoionisation. Depending on the velocity of this final state screening the interaction between the photoelectron and the ionised cluster can alter. If the extra-atomic screening by the support is fast with respect to the timescale of photoemission the interaction between the escaping photoelectron and the charged cluster is reduced and therewith the ionisation potential. According to this substrate dependent charge compensation the classical electrostatic model has been refined by introducing an exponential damping time τ. Within this dynamic model introduced by Hövel *et al.* [73] the delocalised charge of a deposited cluster is compensated between τ and $\tau + dt$ with the probability

$$P(t)dt = \frac{1}{\tau} e^{-\frac{t}{\tau}} dt \tag{4.3}$$

The characteristic time constant τ can be interpreted as a tunnelling time. It can be considered as a measure of the electronic coupling strength between cluster and

substrate. The support-induced screening is probed by the kinetic energy of the photoelectron. According to the inverse-radius model the electrostatic shift is given by

$$E(R,t) = \frac{\alpha e^2}{4\pi\epsilon_0}\left(\frac{1}{R} - \frac{1}{R+vt}\right) \tag{4.4}$$

with R the radius of the cluster and v the velocity of the escaping photoelectron

$$v_{e^-} = \sqrt{\frac{2E_{kin}}{m_{e^-}}} \tag{4.5}$$

where E_{kin} corresponds to the measured kinetic energy of the photoelectron. Finally the distribution of energy shifts is given by equation 4.6 as discussed in [73, 74].

$$P(E) = P(t(E))\frac{dt}{dE} = \frac{RE_{max}}{v\tau\left(E_{max}-E\right)^2}\cdot e^{-\frac{RE}{v\tau(E_{max}-E)}} \tag{4.6}$$

E_{max} is the maximum shift in binding energy which results for τ tending towards infinity, i.e. without substrate-induced core hole screening within the time relevant for photoemission.

Figure 4.3 exemplarily shows the distribution of energy shifts at four neutralisation times. In this simulation a cluster radius of 5.5 Å, which corresponds to a size of Au_{30}, and photoelectron velocity of $7.6 \cdot 10^6$ m/s is used. α has been set to 0.33, which is equal to the value of the free clusters as deduced from the slope in figure 4.2. For the two extremal values $\tau \leq 10^{-18}$ s and $\tau \geq 10^{-14}$ s the shift distribution resembles a delta distribution at zero and E_{max}, respectively. In case of $\tau \leq 10^{-18}$ s the charge left on the cluster is immediately neutralised and practically no energy shift occurs. In contrast, for a delayed neutralisation with $\tau \leq 10^{-14}$ s a maximum electrostatic energy shift appears. For an intermediate neutralisation time between $\tau \leq 10^{-16}$ s and $\tau \leq 10^{-15}$ s the energy shifts are distributed between zero and E_{max}. The measured XPS peak is the convolution of the energy shift distribution with a Voigt profile. This Voigt profile has been simulated by a Lorentzian with a width equal to the natural lifetime of solid gold and a Gaussian with a width equal to the experimental resolution.

The dynamic liquid drop model has recently been applied by Howard *et al.* [62] to analyse the XPS peaks of gold nanoclusters grown on TiO_2. However, the small binding energy shifts and small changes of the line width as a function of the relatively large gold islands ($1.5 - 2.5$ nm) were not sufficient to compare the experimental data with the dynamic liquid drop model in a quantitative manner. Here the dynamic liquid drop model of Hövel *et al.* [73] is applied to supported gold clusters with a well defined size.

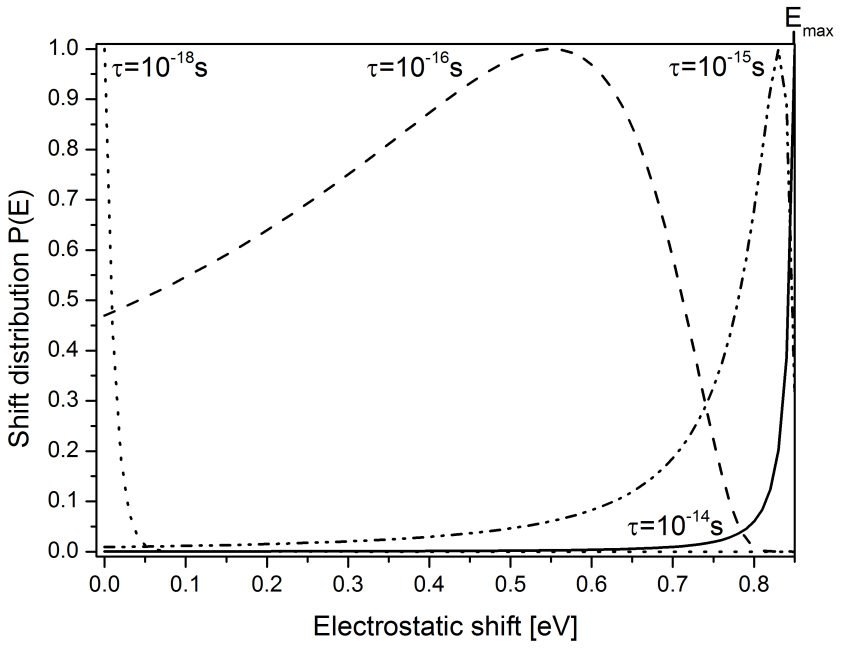

Figure 4.3: *Simulated probability distribution of the electrostatic shift according to the dynamic liquid drop model of Hövel et al. [73]. A kinetic energy of the photoelectron of $E_{kin} \approx 161\ eV$, a cluster radius of $R = 5.5\ \AA$ and $\alpha = 0.33$ has been used at three different neutralisation times τ. For immediate neutralisation ($\tau \geq 10^{-18}s$) of the photohole no electrostatic shift occurs whereas a maximum shift is observed for free particles without neutralisation ($\tau \geq 10^{-14}s$). In the case of charge transfer between the charged cluster and the substrate a broad distribution of energy shifts must be considered ranging from the minimum to the maximum electrostatic shift. The convolution of the shift distribution with the XPS lineshape of the solid (Voigt profile) corresponds to the measured cluster XPS peak.*

In figure 4.4, 4.5 and 4.6 the dynamic liquid drop model has been applied to the measured gold $4f_{7/2}$ XPS peak of Au_{10}. The substrate induced extra-atomic screening time was varied within the core hole lifetime (10^{-16} s to 10^{-15} s). A spherical shape of the clusters has been assumed from which the cluster radius is calculated by equation 4.7 using the number of atoms n and the gold Wigner-Seitz radius $r_{WS} = 1.6$ Å. The addition of the Bohr radius $a_0 = 0.53$ Å accounts for the electron spill-out.

$$r = n^{1/3} \cdot r_{WS} + a_0 \tag{4.7}$$

The shift in binding energy is quite well reproduced by the dynamic model if referred to the gold surface core level peak (located at $E_B = -0.4$ eV). In contrast, if the much smaller shift between the bulk core level peak of solid gold (located at $E_B = 0$ eV)

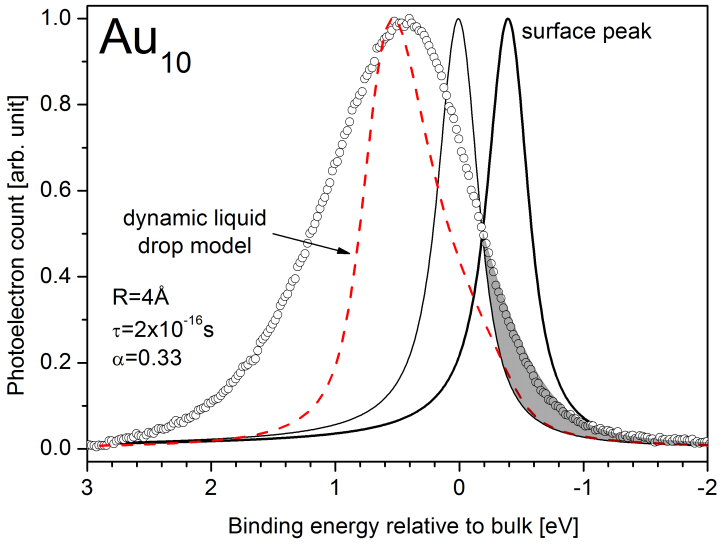

Figure 4.4: *$4f_{7/2}$ XPS peaks of supported Au_{10} together with a fit analysis of the peak shift and lineshape. The dynamic liquid drop model has been applied using a spherical cluster radius of 4 Å and $\alpha = 0.33$. From the position of the red dashed line an extra-atomic screening time of $2 \cdot 10^{-16}$ s has been determined. The dashed line is clearly broadened with respect to the peaks of solid gold. Nevertheless, there are further contributions necessary to fit the experimental data (see figure 4.5). The shaded area is explained in the text.*

and the cluster peak is simulated the lineshape at low binding energies is poorly reproduced. Thus the cluster peak intensity on the right side of the solid gold bulk peak (shaded area in figure 4.4) can be considered as a proof of an initial state shift of the less coordinated surface-like cluster atoms. However most of the cluster peak intensity appears at higher binding energy with respect to the gold bulk peak because the initial state shift is mainly overcompensated by the larger electrostatic final state shift. Nevertheless, because of the exponential-like distribution (equation 4.6) of energy shifts between zero and E_{max} some fraction of the intensity still appears at the pure initial state binding energy. In fact, Wertheim *et al.* measured the 4f core level of small gold particles supported on metglas (amorphous metal alloy) and found a small negative binding energy shift [53] for the smallest coverage. The high density-of-states near and at the Fermi level of this metal-like substrate accelerates charge transfer to the cluster resulting in a fairly reduced charging of the cluster during photoemission.

The dynamic electrostatic model not only predicts an energy shift but leads also to a line broadening due to the exponential-like distribution (equation 4.6) of

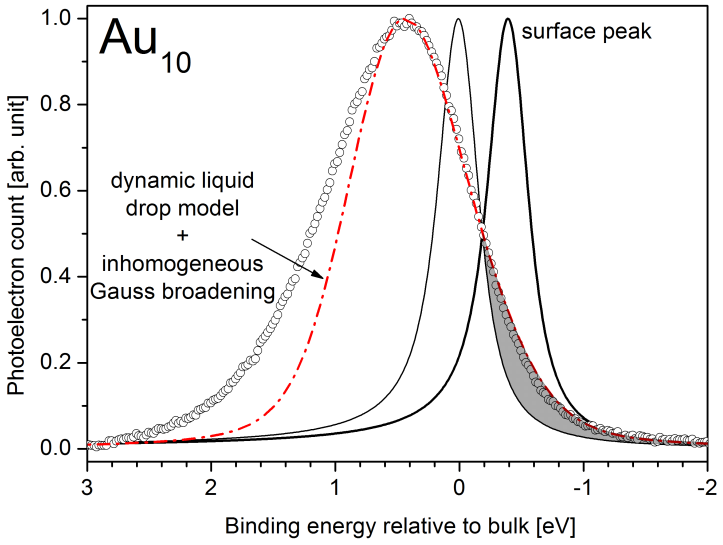

Figure 4.5: *The dash-dotted line is a convolution of the dashed line from figure 4.4 (dynamic screening) with a Gaussian profile (FWHM of 0.75 eV). With an additional inhomogeneous Gauss broadening the peak maximum and the low binding energy tail of the experimental data is well fitted. However, a clear peak asymmetry remains on the high binding energy tail (see figure 4.6).*

energy shifts. The dashed line in figure 4.4 and 4.7 is a convolution of the energy shift distribution P(E) (equation 4.6) with a single gold XPS line, which is a symmetric Voigt profile composed by an experimental Gauss broadening of $\Delta E_{exp} = 0.2\ eV$ and a natural lifetime broadening of $\Delta E_{nat} = 0.3\ eV$. As obvious in figure 4.4 and 4.7 a single gold line convoluted with the electrostatic shift distribution causes more than 50% of the width of the gold data. Clearly this broadening is not sufficient to reproduce the whole width of the measured cluster XPS peaks. Therefore an additional Gauss broadening is necessary to reproduce the width and line shape of the cluster XPS peaks. The additional Gauss broadening is a result of the statistical variation of the electronic and geometric structure of the supported clusters and chemically inequivalent atoms in a cluster. Also the different adsorption sites of the supporting-surface leads to an additional Gauss broadening. Interestingly the broadening is getting larger with decreasing cluster size, i.e. the broadening is more pronounced the more atoms of the cluster are in contact with the substrate. In the case of small clusters, with a rather flat geometry [76], most atoms are in contact with the substrate while for larger clusters gold-gold interactions dominate over gold-substrate interactions. Thus the number of cluster atoms in contact with the support is enhanced for small clusters which could explain the increased broadening

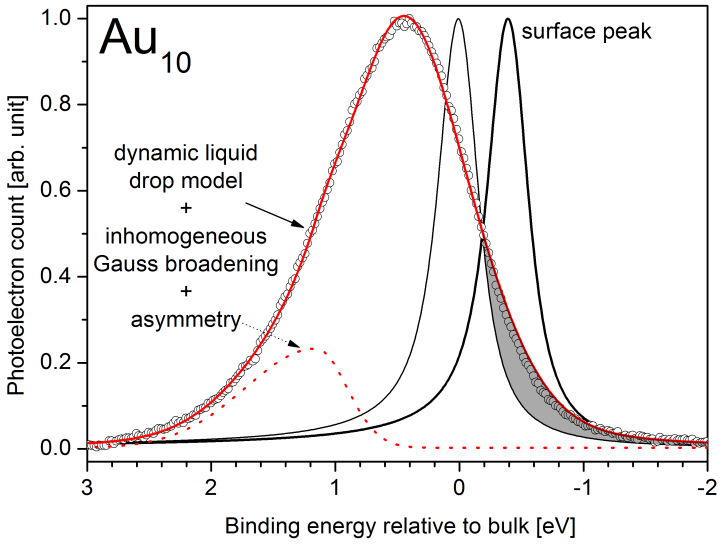

Figure 4.6: *The red full line is a sum of the dash-dotted line from figure 4.5 (dynamic screening plus inhomogeneous broadening) and the remaining asymmetry, which was fitted by an asymmetric Gaussian profile. A comparable symmetry has been found on core-hole line shapes of chemisorbed adsorbate molecules [75]. The experimental data can be well fitted with the dynamic liquid drop model plus additional broadening (see also figure 4.7 for additional cluster sizes).*

with decreasing cluster size. This is furthermore supported by figure 4.8, which shows the $4f_{7/2}$ XPS line width (FWHM) of the clusters as a function of the inverse cluster radius. For clusters larger than ten atoms the line width varies linearly with the inverse cluster radius, as obvious from the figure. In a simple geometric consideration the atomic surface to volume ratio N_S/N of a spherical cluster changes linearly with the inverse cluster radius (equation 4.8). Hence the contact area between the cluster and the surface changes linearly with the inverse cluster radius according to

$$\frac{N_S}{N} \propto N^{-1/3} \propto R^{-1} \tag{4.8}$$

Another contribution to the line broadening could be phonon broadening due to excited intra-molecular cluster vibrations and phonon coupling to the silicon oxide layer which is getting weaker with increasing cluster size. The same explanation has been given in [77] where a cluster size dependent line broadening in small silica supported platinum clusters ($Pt_1 - Pt_6$) has been found. These authors explain the fairly enhanced line width of the platinum 4f peaks by phonons, which are excited by the creation of the core hole at the platinum atom [77].

While the low binding energy part of the XPS peak is well fitted by the dynamic

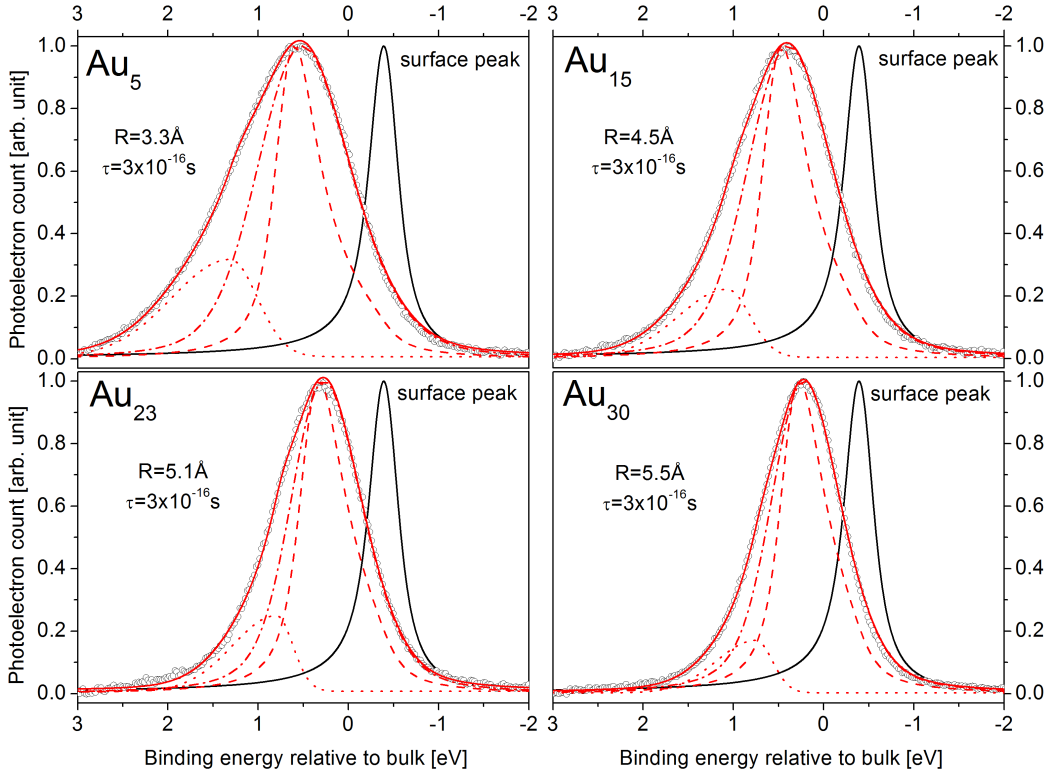

Figure 4.7: *$4f_{7/2}$ XPS peaks of supported Au_5, Au_{15}, Au_{23} and Au_{30} together with a fit analysis of the peak shift and lineshape. The peak envelope is composed by three different contributions: the electrostatic shift of the dynamic liquid drop model, an inhomogeneous Gauss broadening and a high binding energy asymmetry. The gold surface XPS peak of the solid is a convolution of an experimental resolution of $\Delta E_{exp} = 0.2\ eV$ and a natural lifetime broadening of $\Delta E_{nat} = 0.3\ eV$ with a slight Doniach-Sunjic skewness.*

screening model including additional Gauss broadening to consider inhomogeneities a clear asymmetry remains on the high binding energy side. This asymmetry cannot be explained by the dynamic drop model. Note that the asymmetry decreases with increasing cluster size. Hence it is not associated with the evolving metallic character of the clusters, i.e. no Doniach-Sunjic skewness. A comparable asymmetry has been found by Fuggle *et al.* [75] on core hole line shapes of chemisorbed adsorbate molecules but not on those of physisorbed particles. These authors explained the asymmetry on the high binding side with low energy excitations into the continuum caused by the sudden creation of a core hole and associated relaxation of the valence electrons of the support. Due to the core hole in the final state the unoccupied adsorbate levels of the initial state are pulled below the Fermi level and filled in the final state. A pull down of empty gold levels and their filling should be

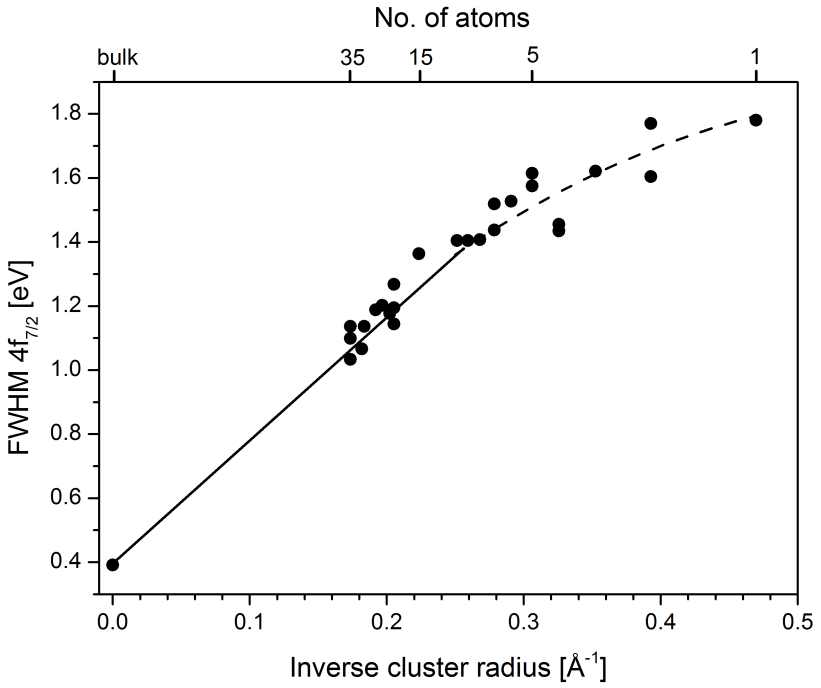

Figure 4.8: *Gold $4f_{7/2}$ XPS line width as a function of the inverse cluster radius. For clusters with more than ten atoms a linear dependence of the line width is obvious. Such a behaviour suggests that the line width increases with decreasing atomic surface-to-volume ratio of the clusters.*

highly probable due to the relatively high density of unoccupied levels in small gold clusters [78, 79]. In analogy to the XPS line shape of chemisorbed molecules we thus interpret the asymmetry on the high binding energy side of the cluster peaks as an indication of chemisorption of the clusters on the substrate. According to this the observed asymmetry is considered as evidence of a relatively strong cluster substrate hybridisation which could also explain the efficient final state charge compensation and therewith the reduced ionisation potential of the supported clusters with respect to the interpolated free clusters.

In summary $4f_{7/2}$ core photoelectron spectra of mass-selected gold clusters (Au_n $n = 1 - 35$) on the natural oxide layer of a silicon wafer have been measured with highest reasonable resolution, i.e. below the natural lifetime broadening. An overall blue shift of the binding energy with respect to the bulk peak is observed, which scales linearly with the inverse cluster radius. The systematic ESCA shift can be explained within the liquid drop model by an electrostatic final state effect which dominates the peak shift. Note that the core ionisation potential as a function of the inverse cluster radius for supported gold clusters changes less strongly than ex-

pected for free clusters. Therefore we assume intense final-state screening of the ionised cluster by charge transfer from the substrate on a timescale relevant for photoemission. Such extra-atomic final-state screening by the substrate and a peak asymmetry on the high binding energy side of the photoelectron peak furthermore give evidence for chemisorption-like interaction between the clusters and substrate. The dynamic screening model is useful to explain the relatively small XPS shift with respect to the free clusters and the liquid drop model. However, this model alone cannot explain the pronounced peak width. The additional Gauss broadening is attributed to inhomogeneous broadening (chemically inequivalent atoms and different adsorption sites) and phonon broadening (phonon excitation of substrate). Cluster specific "each-atom-counts" behaviour is not evident for the size-dependent XPS shift of small supported gold clusters. The photoelectron intensity at binding energies smaller than the gold bulk peak is finally interpreted as an initial state effect due to the reduced coordination of cluster atoms. This initial state effect causes a red shift in binding energy but is mainly overcompensated by the electrostatic final state effect. Note that for supported silver clusters we hardly ever observe any XPS intensity at binding energies smaller than the silver bulk peak (figure 4.9). In fact, solid silver exhibits a marginal surface core level shift [66]. In case of silver the 4d and 5s bands are much more separated in energy than in gold. Therefore the charge redistribution between the silver 4d and 5s valence orbitals is much less pronounced for low-coordinated surface atoms of silver. The result for small silver clusters supports furthermore our interpretation that the XPS intensity observed at the higher energy tail of the XPS peak arises from an initial state effect of low coordinated gold atoms.

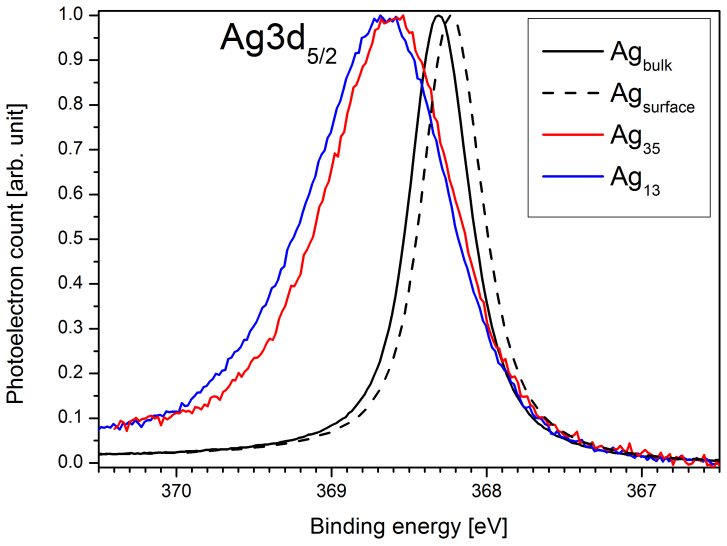

Figure 4.9: *Silver $3d_{5/2}$ XPS peaks of silica supported Ag_{13} and Ag_{35} together with the bulk and surface component of solid silver. All spectra have been recorded at 480 eV photon energy with a total experimental resolution of 260 meV. Only a slight XPS intensity can be observed at binding energies smaller than the silver bulk peak.*

4.2 Auger electron spectroscopy of deposited Cu_n clusters ($n = 8 - 55$)

One of the fundamental properties of metals is the ability to damp electrostatic fields on a relatively short length scale given by the Thomas-Fermi screening length (≈ 1 Å for metals). The ability to screen a long-range Coulomb field is mainly determined by the availability of free charge carriers in the subbands nearest the Fermi level. As a result of the mobile conduction electrons, which are characteristic for metals, the screening in metallic systems is very efficient. In contrast to solid metals, however, the confined electron gas of small metal clusters should have an reduced ability to screen electrostatic fields [80, 81]. Thus in small metal clusters long range interaction forces are expected. In this chapter we will report on the evolution of metallic screening as a function of cluster size by probing the electrostatic interaction between a photoelectron and valence ionised Auger final state using excitation-energy dependent PCI-Auger spectroscopy.

For free clusters photodetachment spectroscopy on anions is usually applied to measure the HOMO-LUMO gap and thus to receive information on the bandgap closure of the clusters [51, 82, 83]. Another method is the measurement of the ionisation potential as, for example, done on mercury clusters by Rademann *et al.* [2]. The methods, however, are not applicable for supported clusters as the extra charge of the anion is after some times transferred to the substrate (see chapter 4.1) and because the valence photoelectron intensity of the clusters will be strongly superimposed by the substrate signal. The application of X-ray based Auger spectroscopy, however, has the unique merit that the intrinsic property of a deposited cluster can be probed without being affected by the signal intensity of the substrate. Thus studying the evolution of the metallicity by means of the core related PCI shift the non metal-to-metal transition of supported metal clusters can principally be probed in an element specific way. Here we will report on the PCI shift in metal clusters which approaches the bulk limit somewhere between 2.5 and 3 nm.

In particular, post collision interaction (PCI) [84, 85] has been used to probe the screening ability of supported metal clusters. The PCI process is characterised by an energy exchange between the photoelectron and Auger electron. Usually the Auger is measured at photon energies far above the core ionisation potential (sudden limit). However, if the photon energy is lowered towards the value of the core ionisation threshold, the Coulomb interaction between the slowly escaping photoelectron and the remaining ion affects the kinetic energy of the Auger electron. The effect is most pronounced at an ionisation energy just above the threshold. The smaller the distance between the photoelectron and the ionised atom during its Auger decay, the larger is the energy loss of the photoelectron and the energy gain of the Auger

electron due to the sudden change from a singly to doubly charged ion (see figure 4.10). In a metal, however, the extra charge in the two hole Auger final state is effectively screened by the conduction electrons so that a PCI shift is practically negligible with respect to the atom [86]. This is different for clusters as the confined electron gas does not efficiently screen the valence holes as a real metal. Therefore the screening ability of copper clusters has been probed by measuring the development of the PCI shift from the atom to the solid. The maximum PCI shift is considered as a quantitative measure of the screening ability of the cluster.

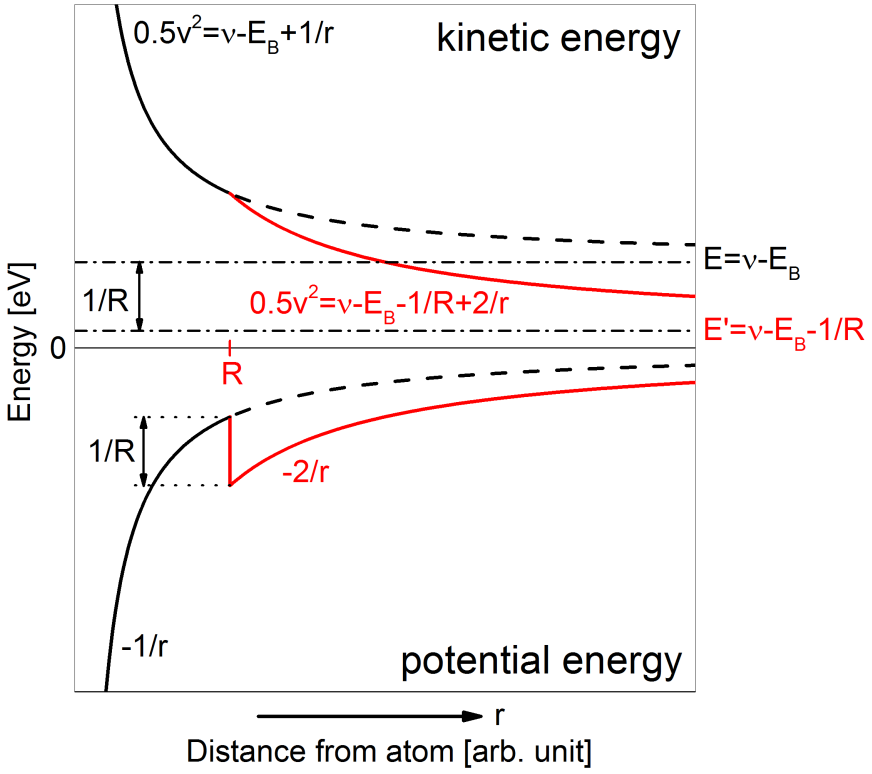

Figure 4.10: *Energy diagram of the PCI process. At a distance R the photoelectron is overtaken by the Auger electron. Suddenly the photoelectron is affected by a doubly charged ion in which previously one charge was screened by the Auger electron. Without PCI the final photoelectron kinetic energy is $\nu - E_B$. In the case of PCI the energy 1/R lost by the photoelectron is transferred to the Auger electron. The figure is based on a diagram from [87]. All units are atomic units.*

Normal Auger in copper clusters

In this sub-section a brief overview of the normal L-edge Auger decay ($L_3M_{4,5}M_{4,5}$) of supported copper clusters is given before discussing the PCI-shifted Auger spectra. The normal Auger decay is measured at an excitation energy far above the core

ionisation potential ($h\nu = IP_{core} + > 50$ eV). Well above the ionisation edge the normal Auger is independent of the photon energy, that means Auger energy and line shape do not change with photon energy. Therefore the normal Auger spectra have been recorded with fully open monochromator exit slit (1200 μm) to get the highest possible photon flux ($\approx 1 \cdot 10^{11}$ photons per second) at beamline PM4. The normal Auger spectra have been recorded with a nominal photon energy of 980 eV and a photon energy resolution of $\Delta E_{h\nu} \approx 3.6\ eV$. The hemispherical electron analyser (Scienta SES 100) was set to a kinetic energy resolution of $\Delta E_{analyser} \approx 1.6\ eV$ (pass energy = 100 eV, entrance slit = 3.2 mm).

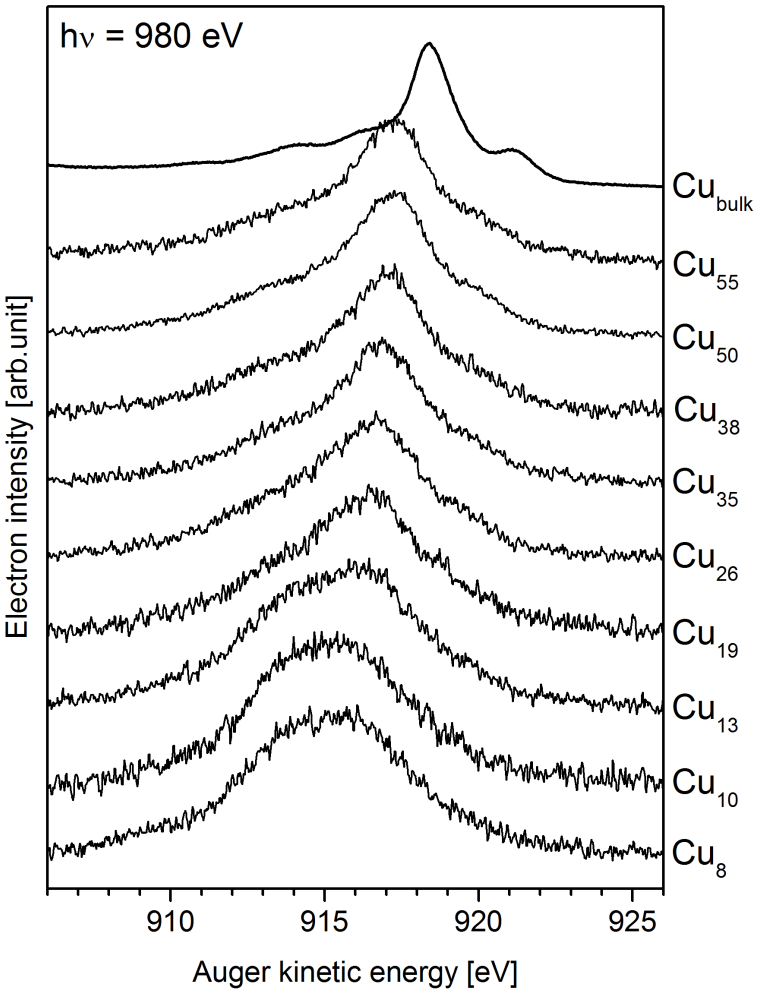

Figure 4.11: *A series of normal Auger (L_3MM) spectra recorded at 980 eV photon energy. The copper bulk spectrum has been measured with a clean copper single crystal. A clear size-dependent shift of the Auger energy is observable.*

Figure 4.11 shows the normal Auger spectra of solid copper and a series of copper clusters. The Auger energy of the main line for all clusters is red shifted with respect

to the bulk value of 918.4 eV [88]. With increasing number of atoms in the clusters the Auger energy tends towards the bulk Auger energy. The maximum shift is -3.3 eV for small clusters and still -1.2 eV for Cu_{55} with respect to the $^1G_4$ main line of the solid [45]. The L_3MM Auger energy corresponds to the difference between the initial core hole state $2p^{-1}$ and the valence ionised two hole final state $3d^{-2}$ including the Coulomb interaction energy $E_{Coulomb}$ of the double vacancy (equation 4.9).

$$E_{kin}^{Auger} = E_{L_3} - E_{M_4} - E_{M_5} - E_{Coulomb} \tag{4.9}$$

With the measured XPS and UPS data of the clusters and bulk [89] it follows that the change of the Coulomb interaction ($\Delta E_{Coulomb}$) contributes most to the red shift of the cluster Auger kinetic energy. The enhanced final state Coulomb interaction for the clusters is probably caused by a stronger localisation of the 3d-orbitals with respect to the delocalised 3d-band of the solid [89].

Most significant, however, is a shift of the Auger energy to higher kinetic energy when recording the spectra at smaller photon energies as discussed in the next chapter. As obvious from equation 4.9 the Auger kinetic energy is increasing with decreasing Coulomb interaction energy, which occurs if the photoelectron emerges slowly and "helps" to screen the two-hole final state during the Auger decay.

4.2.1 Post collision interaction in Cu clusters

The photon-energy dependent Auger spectra have been taken with photon energies close to the L_3 ionisation threshold ($h\nu = 933\ eV$, $h\nu = 937\ eV$), close to the sudden limit ($h\nu = 978\ eV$) and in between ($h\nu = 951\ eV$, $h\nu = 958\ eV$). The spectra have been recorded with a better experimental resolution than the normal Auger spectra (chapter 4.2) since the resonant excitation is photon-energy dependent. The electron analyser resolution was tuned to $\Delta E_{analyser} \approx 1.6\ eV$ and the photon energy resolution was set to $\Delta E_{h\nu} \approx 1.2\ eV$ by closing the exit slit of the monochromator from 1200 μm to 400 μm with respect to the spectra in figure 4.11.

Figure 4.12 shows the cluster Cu_{50} L_3MM Auger region recorded at three different photon energies: below the L_3-edge at $h\nu = 923\ eV$ (shifted about 14 eV to higher kinetic energy), short above the L_3-edge at $h\nu = 937\ eV$ and far above the L_3-edge at $h\nu = 978\ eV$. At photon energies below the L_3-edge, i.e. at 923 eV (blue line), it is not possible to excite L_3MM Auger transitions. In this case just the silicon valence band together with the superimposed weak copper valence band is recorded. At photon energies immediately above the absorption edge, i.e. at 937 eV (red line), the Auger spectrum is superimposed with photoemission lines of the silica support (oxygen 2s at 908 eV, silicon valence band at 925 to 935 eV). To decompose the pure Auger features from the superimposed photoemission lines the below-threshold

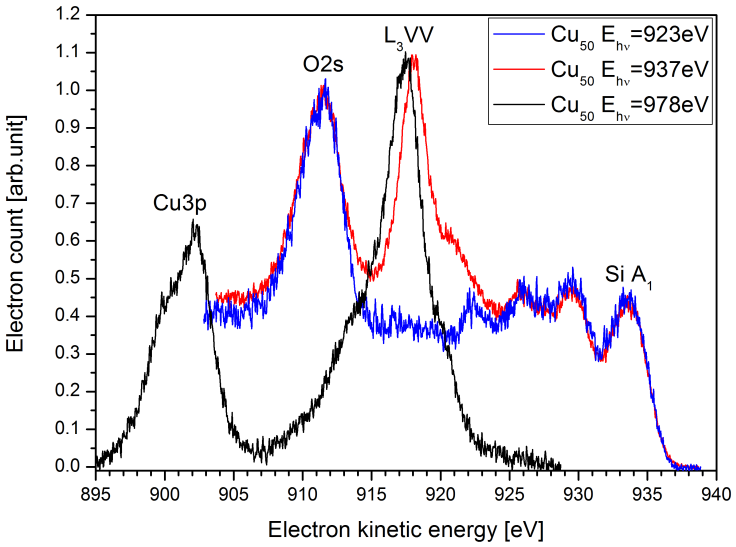

Figure 4.12: *Auger (L_3VV) region of deposited Cu_{50}. The displayed spectra have been measured with three different photon energies. Below the absorption edge ($h\nu$ = 923 eV, shifted 14 eV to higher kinetic energy), near the absorption edge ($h\nu$ = 937 eV) and far above the absorption edge ($h\nu$ = 978 eV). The Auger spectrum recorded with $h\nu$ = 937 eV is superimposed by the silicon valence band at high kinetic energies.*

spectrum recorded at $h\nu = 923\ eV$ has been shifted accordingly to the photon energy and subtracted from the Auger spectra. At photon energies far above the absorption edge (black line) the valence band is shifted fairly beyond the Auger lines and also no XPS peak is present in the Auger region. Only the copper 3p core level is visible at lower kinetic energies but is not overlapping the Auger peak. The spin orbit splitting of the $3p_{1/2}$ and $3p_{3/2}$ state amounts to 2.45 eV. However, the two spin orbit components cannot be resolved because of the relatively broad natural width of 1.6 eV [90].

Figure 4.13 exemplarily shows the Auger spectra of Cu_{26} and Cu_{50} in comparison with the Auger spectrum of a clean copper single crystal. In the cluster spectra the silicon valence band and the oxygen 2s background has been subtracted as described in the preceding paragraph. With a photon energy close to the sudden limit a clear red shift is apparent for the Auger lines of the clusters in comparison to the solid spectrum. The red shift amounts to -1.7 eV and -1.2 eV for Cu_{26} and Cu_{50}, respectively. Most significant, however, is a clear photon energy dependent Auger shift to higher kinetic energies when the cluster spectra are recorded with smaller photon energies. In contrast, the solid Auger spectrum hardly ever shifts when the

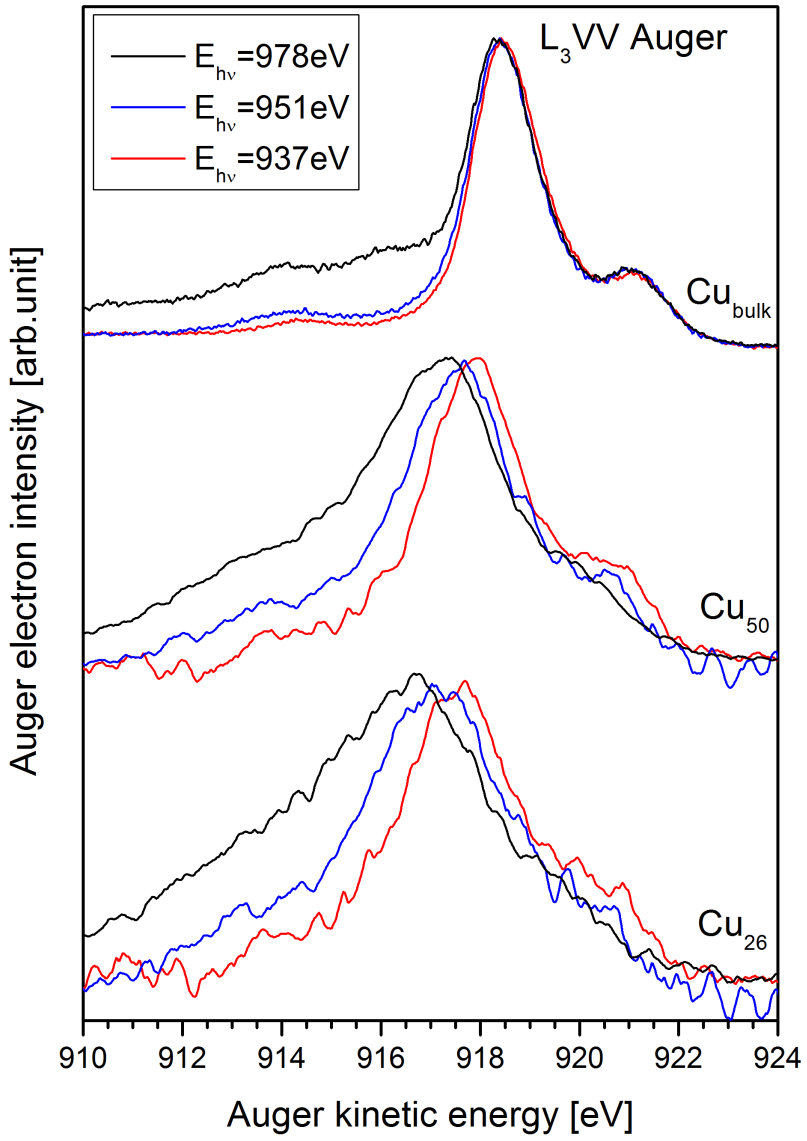

Figure 4.13: *L_3MM Auger spectra of deposited Cu_{50} and Cu_{26} in comparison to a spectrum of a copper single crystal. The spectra have been taken at three different photon energies. Near the sudden limit ($h\nu = 978\ eV$), close to the L_3 ionisation threshold ($h\nu = 937\ eV$) and in between ($h\nu = 951\ eV$). The intensity at Auger kinetic energies smaller than 917 eV in the bulk spectrum measured at $h\nu = 978\ eV$ arises due to satellite Auger decay which does not occur at a photon energy of 937 eV and 951 eV, i.e. from shake up/off initial states.*

photon energy is changed.

In figure 4.14 the energies of the main Auger line of all cluster samples and the solid are compiled and plotted against the photon energy. The curve of the

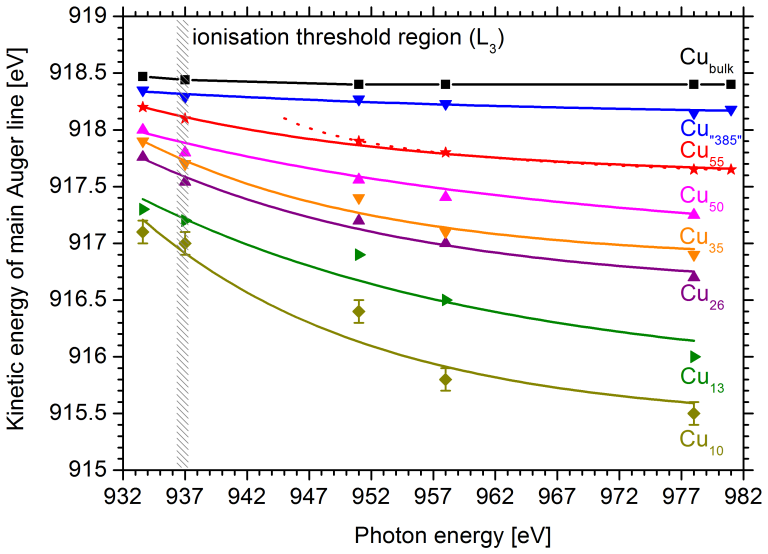

Figure 4.14: *The kinetic energy of the Auger main line as a function of the photon energy for a series of copper clusters (Cu_8 - Cu_{55}). Also shown is the curve of a high-density sample with an average size of 385 copper atoms and solid copper. The dotted lines through the data points are polynomials, which serve as a guide to the eye. For Cu_{55} a Barker-Berry fit (red dashed) is shown which is applicable for photon energies several electron volts above the threshold. The hatched area marks the L_3 ionisation threshold of the copper clusters and copper bulk [67].*

solid (black) shows no significant deviation of the Auger kinetic energy as function of the photon energy. Over the whole excitation energy range, i.e. between the core ionisation potential (hatched area) and the sudden limit ($h\nu = 978\ eV$), the maximum difference in the Auger kinetic energy amounts just to 50 meV. In contrast to the bulk, however, the Auger kinetic energy of the clusters show a clear photon energy dependence. The change of the Auger kinetic energy with respect to the value at the sudden limit corresponds to the PCI shift. All clusters show a positive PCI shift. The shift is largest for small clusters while it decreases with increasing cluster size. The maximum PCI shift decreases from 1.5 eV to 0.45 eV as function of cluster size (from Cu_{10} to Cu_{55}). The maximum PCI shift approaches the bulk limit at a cluster size of ≈ 385 atoms. The Cu_{385}-sample has been approximated by the statistical distribution of agglomerated Cu_{55} clusters on the substrate as explained later on. At photon energies well above the ionisation threshold the PCI shift follows the classical Barker-Berry formula (equation 4.10, dashed line in figure 4.14) [84, 85],

which is valid for $\Delta E_{kin} \ll E_{h\nu} - IP$

$$\Delta E_{kin}^{Auger} = \frac{1}{2\tau} \frac{1}{\sqrt{2(E_{h\nu} - IP)}} \tag{4.10}$$

with τ the lifetime of the inner-shell vacancy and IP the core ionisation potential. The ionisation potential is equal to the copper $2p_{3/2}$ binding energy of the supported clusters, which range between 932.8 eV (Cu_{55}) and 933.3 eV (Cu_{10}) [89] and the work function of the silicon support, which is ≈ 4.5 eV [91]. Near the ionisation potential the Auger kinetic energy varies smoothly across the threshold region according to the Niehaus model [92]. This model describes the Auger decay in the presence of a slowly escaping photoelectron exposed to the Coulomb field of the core hole.

The significant PCI shift of the small deposited copper clusters is attributed to a less efficient screening and consequently to a rather non-metallic character of the supported copper clusters. In other words the valence electrons of the supported clusters are not metallic enough to efficiently screen the double vacancy of the Auger final state. In the case of the metallic bulk in contrast, the charges of the two hole final state are efficiently screened by the delocalised valence electrons. Hence the presence of a slowly escaping photoelectron barely effects the kinetic energy of the Auger electron. This is different for the non-metallic clusters. The slowly escaping photoelectron helps to screen the double vacancy of the Auger final state, which causes a gain of the Auger kinetic energy. As a result the Auger kinetic energy increases in the presence of a slow photoelectron excited shortly above the L_3 threshold energy. The Auger kinetic energy converges to the value of the normal Auger at higher photon energies due to a loss of screening of the fast escaping photoelectron. The electrostatic interaction, i.e. the PCI shift, clearly depends on the cluster size. This size-dependence shows that the non-metallic character of the clusters is not obscured by the interaction with the substrate.

The cluster size-dependent evolution of the screening energy is quantified with the maximum PCI shift per cluster. As a result of energy conservation the interaction energy between the photoelectron and the remaining ionic final state is transferred to the kinetic energy of the Auger electron. Thus the maximum PCI shift, i.e. the difference of the Auger kinetic energy measured with a photon energy far above and close to the core ionisation threshold, is equal to the negative value of the interaction energy. The interaction energy between the photoelectron and the two-hole Auger final state as a function of the cluster radius is shown in figure 4.15. The cluster radius again has been approximated with equation 4.12. The very small clusters are reasonably well fitted with an ordinary Coulomb-like potential, which clearly deviates from the data for clusters larger than Cu_{19}. Between Cu_{55} and Cu_{385} the interaction becomes disproportionally damped. Thus the screening develops into a

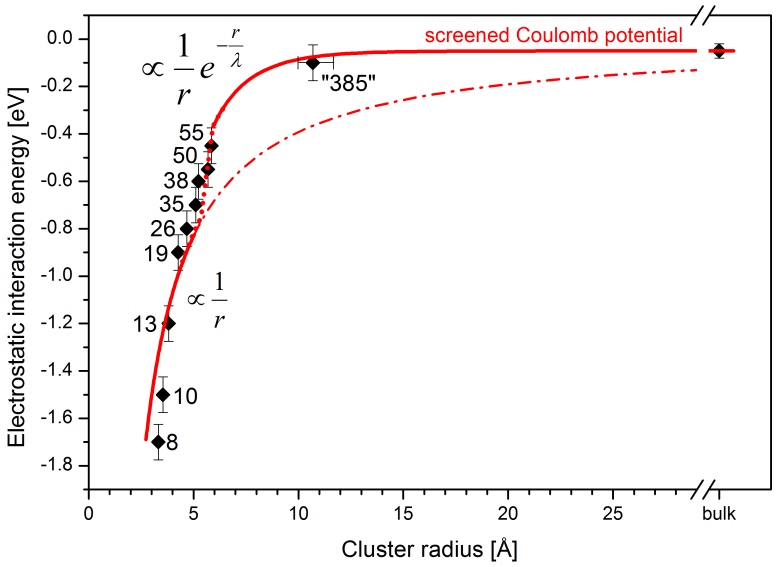

Figure 4.15: *The electrostatic interaction energy, which equals the negative maximum PCI shift, as a function of the spherical cluster radius. The data points from Cu_{19} to Cu_{55} are interpolated to visualise the evolution from a Coulomb-like into a screened Coulomb-like interaction. For the small clusters a pure Coulomb-like potential has been fitted whereas for the data points from Cu_{55} to the bulk a screened Coulomb-like potential is shown. The size of the cluster with 385 atoms has been approximated with a Poisson distribution after deposition of a high density Cu_{55} sample.*

macroscopic like behaviour between 0.5 nm and 1 nm. For the region from 0.5 nm to the bulk limit a screened Coulomb potential has been fitted using

$$\Phi_{Coulomb}(r) = \frac{Q}{4\pi\epsilon_0 \cdot r} e^{-\frac{r}{\lambda}} \tag{4.11}$$

Q is the charge of the remaining ion and λ the Thomas-Fermi screening length or the inverse Thomas-Fermi screening wave vector. A Thomas-Fermi screening length of $\lambda = 2.5$ Å is deduced from the exponentially damped Coulomb fit. This value is somewhat larger than the screening length for metals with $\lambda \approx 1$ Å but much smaller than the screening length for semiconductors with $\lambda \approx 100$ Å. For very small clusters the interaction energy correlates linearly with the inverse cluster radius as can be seen in figure 4.16. Thus the electrostatic interaction behaves Coulomb like for very small clusters, whereas the inverse radius dependence gets clearly weakened for clusters larger than Cu_{19}. The change of the slope in figure 4.16 is caused by the onset of screening which gradually evolves with cluster size.

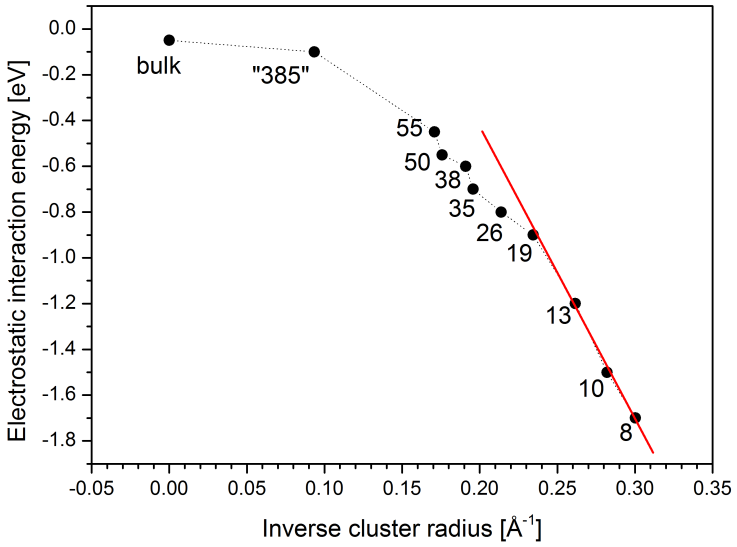

Figure 4.16: *The electrostatic interaction energy as a function of the inverse cluster radius. Note that the Coulomb-like linear dependence gets clearly weakened for clusters larger than* Cu_{19}.

The size of the cluster with a PCI shift close to the bulk limit has been approximated by island formation of Cu_{55} clusters as it is not possible to deposit such big clusters due to limitations of the cluster apparatus (transmission of the dipole magnet up to 5000 u). The high-density Cu_{55} sample was produced by depositing Cu_{55} clusters for approximately three hours and also strongly focusing the ion beam onto the substrate. The cluster spot size on the substrate has been deduced by position dependent Cu $2p_{3/2}$ XPS yield. During the deposition a total charge of $\approx 8 \cdot 10^{-8}$ C was accumulated as deduced by integrating the recorded deposition current. From both the total deposited charge and cluster spot size a cluster density of $\approx 8.5 \cdot 10^{13}$ clusters per cm^2 is received. Note that the agglomeration of the high-density Cu_{55} sample is experimentally evident by the fairly reduced PCI shift with respect to the normal density spectrum of Cu_{55} ($\approx 5 \cdot 10^{11}$ clusters per cm^2). Also the XPS and XAS spectra (not shown) of the high density sample resemble more this of the bulk than the normal density sample. The island size of the agglomerated Cu_{55} clusters has been approximated by the statistical distribution of the clusters on the substrate. Therefore the sample surface is hypothetically divided in small deposition units. These units are defined in such way that all deposited clusters are clearly separated from each other, i.e. all deposition sites around one cluster are unoccupied (see figure 4.17). On a sample surface with well ordered and separated clusters every deposition unit is occupied by a single cluster. At higher surface density the

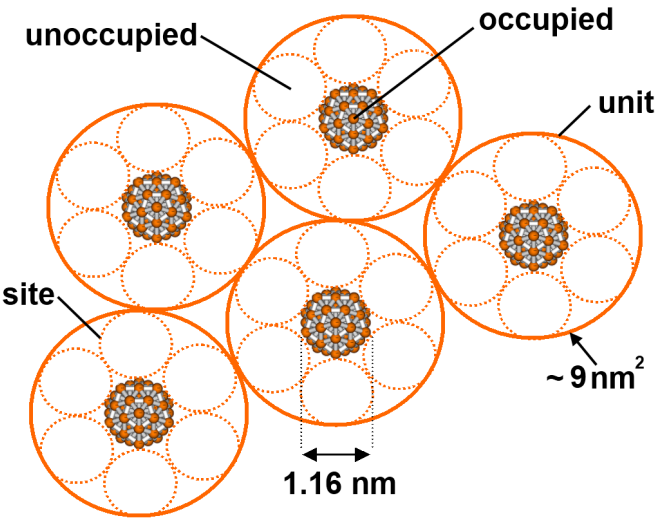

Figure 4.17: *A monolayer of well ordered and separated Cu_{55}-clusters is defined by occupied and unoccupied deposition sites (area $\approx 1\ nm^2$). Each deposition unit (area $\approx 9\ nm^2$) is occupied by only one cluster for an ideal monolayer of non-interacting clusters.*

additional clusters will be deposited adjacent to an existing cluster leading to the statistical formation of islands of two, three and more Cu_{55} clusters. One adsorption site has the same area as the projected area of a Cu_{55} cluster. The projected area of an icosahedral Cu_{55} cluster has been determined by the radius r of a sphere with $n = 55$ atoms using the Wigner-Seitz radius of copper bulk $r_{WS} = 0.14$ nm. The addition of the Bohr radius $a_0 = 0.53$ Å gives a reasonably approximation of the electron spill-out.

$$r = n^{1/3} \cdot r_{WS} + a_0 \tag{4.12}$$

The assumed spherical geometry can be motivated by the fact that compact icosahedral structures are favoured for free copper clusters [93]. These compact structures, even though partially distorted, are still maintained during deposition as simulated in a recent molecular dynamics study of small copper clusters softly landed on a copper surface [94]. With the resulting cluster radius of $r_{Cu_{55}} = 0.58$ nm a projected cluster area of 1.06 nm^2 has been calculated. One deposition unit is build up of one adsorption site in the centre and six densely packed adsorption sites around. The result is an area of ≈ 9 nm^2 for a single deposition unit. This corresponds to $\approx 1.1 \cdot 10^{13}$ deposition units per cm^2. The statistical distribution of the number of Cu_{55} clusters per deposition unit is finally given by a Poisson distribution. With our experimentally determined cluster coverage density of $\approx 8.5 \cdot 10^{13}$ per cm^2 and the density of deposition units of $\approx 1.1 \cdot 10^{13}$ per cm^2 the expected value and variance

of the Poisson distribution (equation 4.13) amounts to $\lambda \approx 7.7$.

$$P_\lambda(k) = \frac{\lambda^k}{k!} e^{-\lambda} \tag{4.13}$$

$P_\lambda(k)$ is the probability of k Cu_{55} clusters per deposition unit, i.e. the number of agglomerated Cu_{55} clusters or the island size. The Poisson distribution is displayed in figure 4.18. The weighted average of this statistics amounts to an island size of seven Cu_{55} clusters, i.e. Cu_{385}.

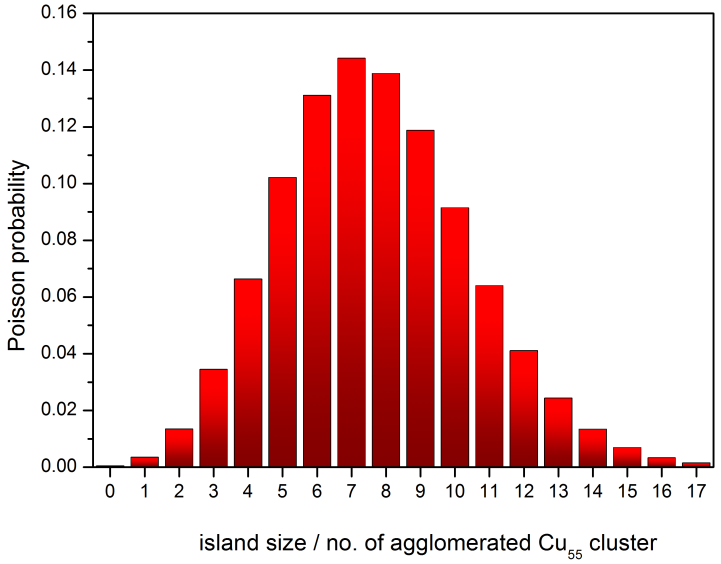

Figure 4.18: *Poisson distribution for the approximation of the agglomerated island size of the high-density Cu_{55} sample. The ratio between the surface density of the high density Cu_{55} sample and the surface density of an idealised monolayer of non-interacting Cu_{55} clusters is 7.7. This equals the expected value λ of the Poisson distribution. The weighted average amounts to an island size of $\approx$ 385 atoms.*

In summary, the PCI shift reveals that the photoelectron core-hole interaction gradually changes from a Coulomb-like into a screened Coulomb-like interaction within the sub-nm range. As a result of the fairly reduced screening ability supported copper clusters smaller than 1 nm should be considered to be clearly less metallic than the solid. A gradual change into a metallic-like screening behaviour evolves at a diameter between 1 and 2 nm.

4.3 X-ray absorption fine structure of deposited Cu_n clusters ($n = 19; 35; 55$)

Generally, structural information on supported clusters is hardly to receive due to missing long-range order and quite diluted sample density (1 % monolayer density). STM has gained atomic resolution of nanoclusters just in some particular cases and cannot easily be used for systematic investigations [95]. New promising geometry information of deposited clusters have recently been received with aberration-corrected scanning transmission electron microscopy (HAADF-STEM) for which crystalline-like cuboctahedral structures have been identified [96]. First direct evidence for bond-length contraction (2-10 %) as a function of decreasing particle size has been gained by EXAFS on atomic Cu-islands (1.5 - 4 nm) by Stöhr *et al.* at SSRL [97]. EXAFS on matrix-isolated nanoparticles (0.7 - 1.5 nm mean diameter) with a broad size distribution of +/- 0.5 nm has received fcc-like structures for particles of >1 nm diameter with nearest-neighbour distances similar to the bulk [4]. Strong bond length contraction of >10 % is suggested for clusters with a diameter <0.5 nm [14]. EXAFS measurements on size-selected clusters have not been reported yet.

4.3.1 X-ray absorption near edge structure

Figure 4.19 presents the XANES region of the X-ray absorption spectra of silica supported copper clusters in comparison with the spectrum of a bulk-like copper foil. All spectra have been recorded by measuring the copper Kα_1 X-ray fluorescence at about 8046 eV using an energy dispersive X-ray fluorescence detector (Röntec x-flash 1201). The spectra of Cu_{19} and Cu_{55} have been measured at atmospheric pressure whereas Cu_{35} has been measured under vacuum conditions. The K-edge energy is given by the maximum of the derivative of the absorption edge. The location of the absorption edge of solid copper is equal to the literature value of $E_0 = 8980.5$ eV [98]. The K-edge of all cluster samples is shifted towards higher photon energy. The absorption edge of Cu_{35} is shifted by 5.2 eV to $E_0^{Cu_{35}} = 8985.7$ eV. For the aerated samples, Cu_{19} and Cu_{55}, the absorption edge is shifted even more namely by 10.2 eV and 11 eV for Cu_{19} ($E_0^{Cu_{19}} = 8990.7$ eV) and Cu_{55} ($E_0^{Cu_{55}} = 8991.5$ eV), respectively. The considerable shift hints to oxidation of the aerated samples as a blue shift of the absorption edge with increasing oxidation state has been observed for solid copper oxide samples such as CuO and Cu_2O [99]. XANES is generally interpreted in terms of unoccupied orbitals near the Fermi level, into which the core electron is excited. Due to orbital angular momentum conservation only dipole transitions are allowed for copper in the resonant excitation region before the ionisation threshold. The shoulder seen at the absorption edge of solid copper is attributed to the 1s $\rightarrow$ 4p

bound-to-bound state transition. In contrast, such shoulder can not be observed in the cluster spectra.

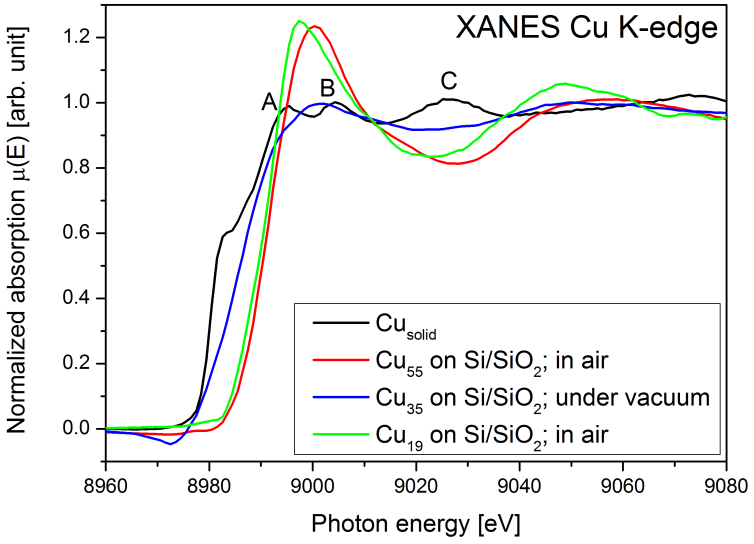

Figure 4.19: *K-edge XANES spectra of Cu_{35}, aerated Cu_{19} and Cu_{55} and a copper foil. The cluster absorption edge is shifted to higher photon energy. Moreover the absorption fine structure in the multiple-scattering region is clearly different as compared to solid copper.*

Moreover the overall shape of the cluster and solid absorption spectra is strikingly different. Solid copper shows its characteristic features at ≈ 8995 eV, ≈ 9004 eV and ≈ 9026 eV within the post-edge region (marked with A, B and C in figure 4.19), whereas the cluster spectra just show two broad features at ≈ 9000 eV and ≈ 9050 eV. A double feature has also been found in recent multiple-scattering calculations for copper clusters assuming a fcc-like structure by Oyanagi *et al.* [100]. Nevertheless, the calculated XANES spectra of Cu_n ($n \geq 43$) of these authors show a triple feature similar to the solid spectrum, what cannot be confirmed by our measurements. Montano *et al.* [14] suggest a fcc structure for copper clusters with $n \geq 13$ atoms based on EXAFS studies of matrix-isolated copper nano clusters (5 - 15 Å mean diameter). However, the observed solid-like fcc structure of the matrix-isolated copper clusters might be induced by interaction of the clusters with the argon-matrix as discussed in [101, 102]. Mazalova *et al.* [103] presented L_3-edge XANES of matrix-isolated Cu_{13} in the gas phase together with calculations of Cu_{13} of icosahedral, cuboctahedral and amorphous structure. Their experimental XANES spectrum resembles most the theoretical spectrum of icosahedral Cu_{13}. Therefore these authors conclude that small copper clusters favour icosahedral arrangement

compared to cuboctahedral and amorphous geometry. A structural change from icosahedral structure to fcc has been discussed by Reinhard *et al.* [104] who studied nanometer-sized free copper particles using electron diffraction. These authors found that icosahedral structure dominates at sizes well below 3.8 nm, while fcc structure is favoured at $\geq$3.8 nm. The geometrical structure of copper nanoparticles changes with particle size because of the competition between surface and bulk energy contributions. Icosahedral structure minimises surface energy whereas fcc structure minimises bulk energy [104].

From the differences in the multiple scattering region of the absorption spectra it is obvious that the unoccupied valence region and the concluded structure of the deposited copper clusters is clearly different from the structure of solid copper. Also the comparison with the spectra of Oyanagi *et al.* and Montano *et al.* demonstrates that the structure of the measured copper clusters is not fcc-like.

There are also differences in the line shape of the individual cluster spectra. The wiggles in the near post-edge region of the oxidised clusters are much more pronounced as compared to the cluster measured under vacuum conditions. By comparing the XANES of the clusters with the solid we can experimentally confirm that Cu_{35} did not oxidise under the prevailing vacuum conditions, whereas Cu_{19} and Cu_{55} oxidised at atmospheric pressure. The changed XANES features are a result of the oxidation as in this case the filled 3d-band of the cluster is emptied. A "white-line" similar to 2p $\rightarrow$ 3d transitions in the soft X-ray regime results due to partial hybridisation of empty 3d orbitals with 4p orbitals.

4.3.2 Extended X-ray absorption fine structure

EXAFS evaluation - example solid copper

The EXAFS spectra of copper clusters have been recorded by measuring the K-shell X-ray fluorescence. For data evaluation the software package IFEFFIT (interactive XAFS analysis and Feff fitting) [105] together with HORAE[1] [106] has been used. IFEFFIT is a suite of programs for XAFS analysis including Feff6l [107] for EXAFS refinements. Horae is a collection of graphical interfaces using IFEFFIT including Athena for XAS data processing, Artemis for EXAFS analysis using Feff and Hephaestus a beamline utility providing tables of atomic absorption data. First, the fine structure beyond the absorption edge (E_0) has to be isolated. This fine structure, the XAFS function $\chi(E)$, is defined as

$$\chi(E) = \frac{\mu(E) - \mu_0(E)}{\Delta\mu_0} \tag{4.14}$$

[1]In Greek mythology the Horae were the goddesses of seasons.

where $\mu(E)$ is the measured absorption spectrum and $\mu_0(E)$ is the post-edge background representing the photoabsorption curve of an atom. The atomic background is not the absorption of a physically isolated atom but rather the absorption of an atom in its environment, where the effects of the neighbouring atoms are disabled. $\Delta\mu_0$ is the height of the post edge background, on which the oscillating EXAFS signal is superimposed. The absorption spectrum is normalised to get rid of variations in sample preparation, detector settings and other aspects of measurement. Normalisation is done by fitting a pre-edge and a post-edge line to the spectrum. The difference at the absorption threshold is $\Delta\mu_0$, which is used for normalisation. To get the position E_0 of the edge step (absorption threshold), the absorption spectrum has to be differentiated and the maximum of the derivative gives the edge step energy. Figure 4.20 shows the copper solid K-edge absorption spectrum together with

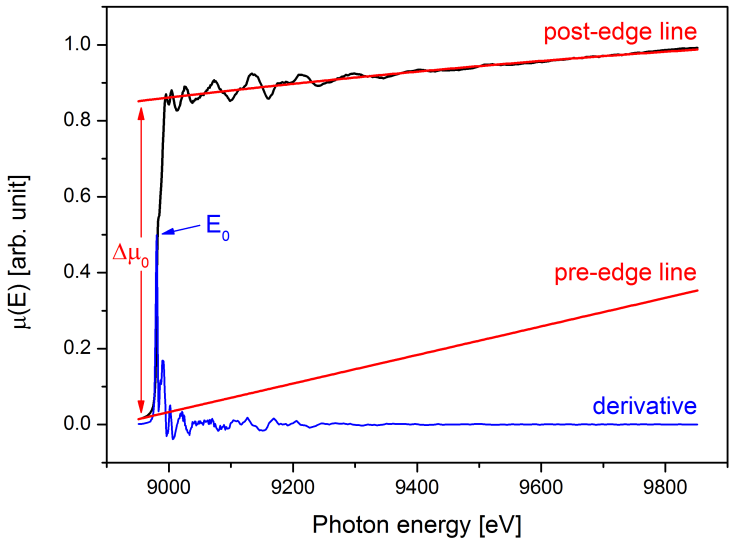

Figure 4.20: *EXAFS spectrum of solid copper as measured by the X-ray fluorescence. The maximum of the derivative of the spectrum gives a K-edge energy E_0 of 8980.5 eV which is equal to the literature value [98]. The difference of the fitted pre-edge and post-edge lines at the edge energy is the normalisation factor $\Delta\mu_0$.*

the fitted pre-edge and post-edge lines. The derivative of the spectrum has been multiplied by a factor of four for a better visibility. As can be seen the derivative has two maxima because of the kink in the absorption edge (see figure 3.3). The kink is associated with a bound-to-bound state transition 1s $\rightarrow$ 4p. E_0 has been set to the first most intense peak. The resulting normalised spectrum is shown in figure 4.21.

The next step is the post-edge background subtraction to isolate the EXAFS sig-

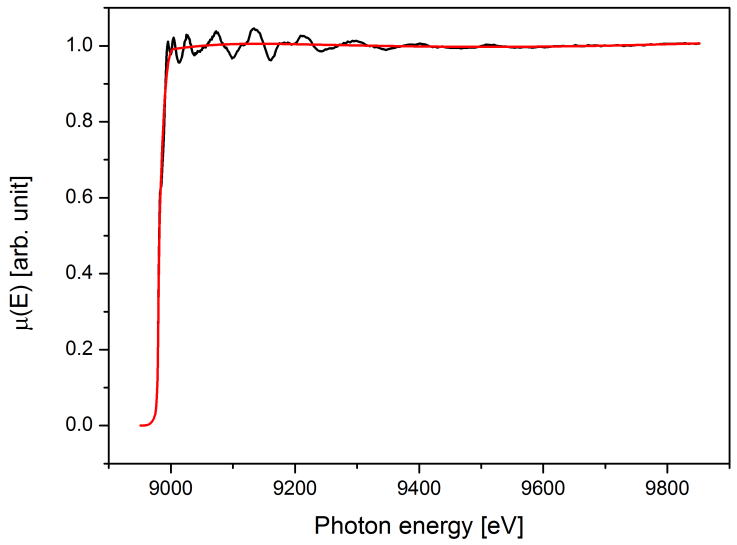

Figure 4.21: *The normalised copper solid EXAFS spectrum (black) together with the post-edge background (red) which has to be subtracted in order to isolate the EXAFS fine structure. The post-edge background equals the absorption of an isolated atom. This post-edge background has to be fitted in such a way that only a low frequency background is removed but not the high frequency EXAFS fine structure.*

nal. Since the absorption spectrum of a copper atom is not available the background has to be approximated. The background is determined by least-square fitting of the experimental data with a spline. A spline is a piecewise defined function which consists of several polynomials of the order n. These polynomials are linked to each other at the nodes where the function value and the first derivative of two adjacent splines have to match. By varying the number and order of the polynomials a very flexible spline can be constructed. The fit of the spline is performed in such way, that the low frequency contributions of the background are removed from the high-frequency EXAFS signal [108]. Athena provides a background-removal procedure, which can be manipulated by several parameters to get a "correct" background. Whether the background approximation is proper can be seen after Fourier transformation since the low frequencies oscillations in k-space cause unphysical low distances at around 1 Å in R-space. After post-edge background subtraction and converting the photoelectron's kinetic energy into wavenumbers with equation 3.9, one gets the EXFAS fine structure in k-space, or simply the EXAFS. The EXAFS of copper bulk is displayed in figure 4.22. As can be seen the EXAFS decays rather quickly with increasing k. To amplify the oscillations at high k and to get a more uniform intensity over a larger k-range the EXAFS can be weighted with k^n with n

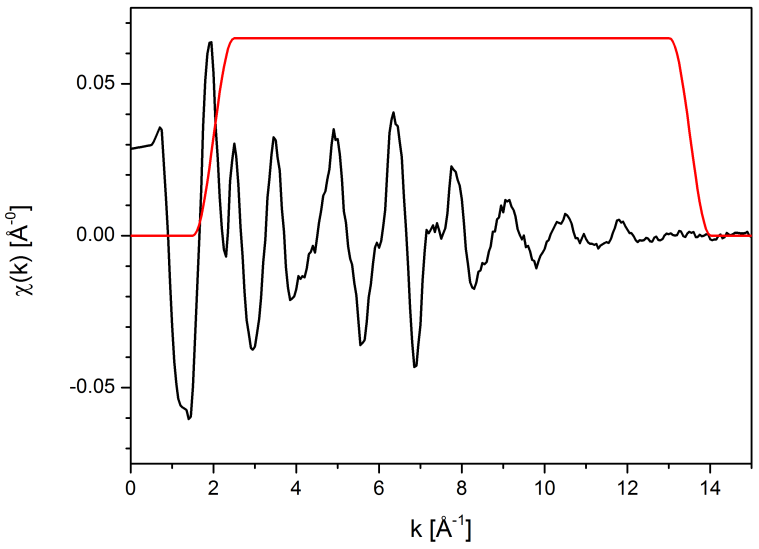

Figure 4.22: *Copper bulk EXAFS after subtraction of the single atom absorption signal and converting the photoelectron kinetic energy into wavenumbers. The EXAFS is decreasing rapidly with k. In order to enhance the EXAFS at higher k-values with respect to the lower k-values, $\chi(k)$ can be multiplied by k to the power of 1, 2 or 3. Thus here $\chi(k)k^0$ is displayed.*

equal to one, two or three. Figure 4.23 shows the k^2-weighted EXAFS. Also shown is a Hann window function by which the k^2-weighted EXAFS will be multiplied before Fourier transformation. The window function defines the weighting of the EXAFS during Fourier transformation.

The last step of the EXAFS analysis is the Fourier transformation of the k^2-weighted EXAFS $k^2\chi(k)$. Figure 4.24 shows the Fourier transformed EXAFS spectrum in R-space. For physical interpretation it is common to display the magnitude of the Fourier transform since the Fourier transformation

$$\hat{\chi}(R) = \frac{1}{\sqrt{2\pi}} \int_0^\infty k^n \chi(k) e^{ikr} dk \tag{4.15}$$

yields a complex function consisting of an imaginary sine and a real cosine part. The magnitude of the Fourier transform can be interpreted as a pseudo radial distribution function showing features equal to the nearest neighbour distances. It is important to mention that the nearest neighbour distances on the abscissa are not equal to the real interatomic distance because of the phase shift the electron wave experiences. The phase shift is caused by the movement of the ejected photoelectron in the varying potential of the absorbing and backscattering atom. The total phase shift is a sum of

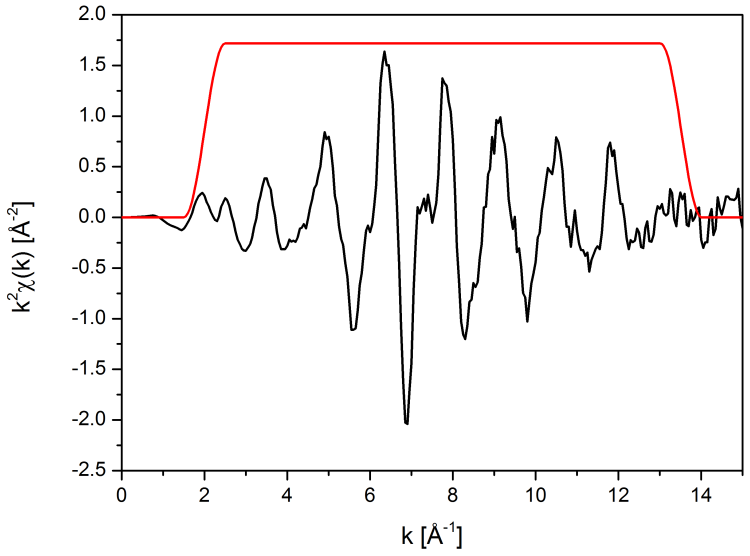

Figure 4.23: *The k^2-weighted EXAFS together wiht a Hann window function (red line). After weighting $\chi(k)$ with k^2 the EXAFS is more uniform over the whole k-range. The EXAFS will be multiplied with the window function for weighting during Fourier transformation.*

the phase shift of the outgoing photoelectron from the ionised absorbing atom and the phase shift of the backscattered photoelectron from the neutral neighbouring atom [109]. As can be seen in equation 4.18 the phase shift belongs to the argument of the sine function which contains the distance information. The phase shift can be approximated linear in k over the EXFAS energy range with a negative slope as

$$\delta_j(k) = -\alpha_j k + \beta_j \tag{4.16}$$

with α_j and β_j constant [110]. By substituting equation 4.16 into equation 4.18 one gets the argument of the sine function of the EXAFS equation 4.18

$$k(2R_j - \alpha_j) + \beta_j \tag{4.17}$$

This means that the frequency of the sine is changed from $2R_j$ to $2R_j - \alpha_j$ and in the Fourier transform all features are shifted by α_j towards smaller radius. To obtain the nearest neighbour distances from the pseudo radial distribution function α_j has to be added to the position of the peaks. For copper α_j is about 0.3 Å [97].

The EXAFS equation is given by [46]

$$\chi(k) = \sum_j \frac{N_j e^{-2k^2\sigma_j^2} e^{-2R_j/\lambda(k)} f_j(k)}{kR_j^2} sin[2kR_j + \delta_j(k)] \tag{4.18}$$

with j the individual coordination shell of identical atoms at approximately the same distance from the central atom, N_j the coordination number, $\lambda(k)$ the inelastic mean free path of the photoelectron, $f_j(k)$ the scattering amplitude, $\delta_j(k)$ the phase shift and σ^2 the mean square displacement in the bond distance R_j because of slightly different nearest neighbour distances even for atoms of the same coordination shell. As can be seen the EXAFS will consist of several frequencies, hence it is possible to identify different coordination shells. Due to the $\lambda(k)$ and R_j^{-2} term EXAFS only probes in a short distance around the central atom.

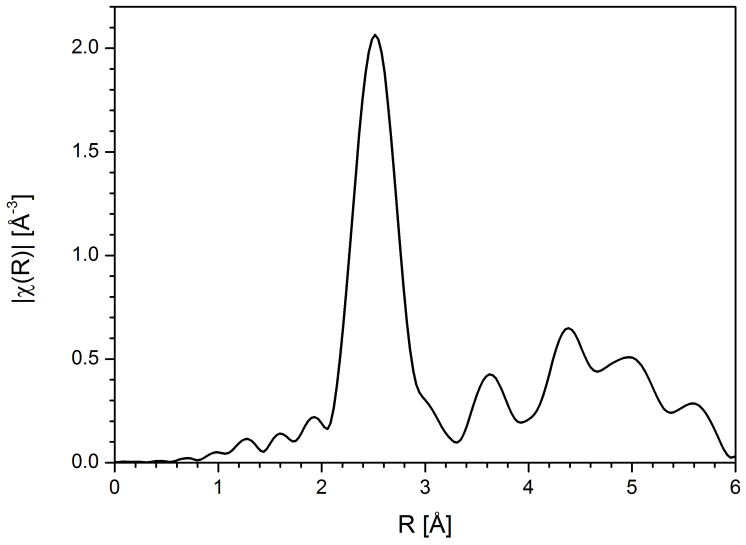

Figure 4.24: *Phase corrected copper bulk EXAFS after Fourier transformation into R-space. The intense feature at ≈ 2.5 Å is the bond distance of the first coordination shell. The features at larger radii belong to higher coordination shells.*

The intense feature at 2.52 Å in figure 4.24 gives the distance from the absorbing atom to the atoms of the first coordination shell. The weaker features at larger radii arise due to higher coordination shells. The calculated nearest neighbour distance for fcc copper with a lattice parameter of 3.61 Å is 2.55 Å. Montano et al. [14] indicate 2.54 Å for the first near-neighbour distance of fcc copper. The determination of the coordination numbers of the coordination shells for copper is straightforward, because the crystal structure of copper is known. Otherwise the coordination numbers have to be determined, together with the bond distances and the mean square displacement, by EXAFS modelling. When the scattering amplitude, the phase shift and the inelastic mean free path are known then the structural parameters N_j, R_j and σ^2 can be refined by fitting $\chi(k)$ with the EXFAS equation. Starting with the crystal structure of copper FEFF software can calculate the missing parameters

$f_j(k)$, $\Delta_j(k)$ and $\lambda(k)$. These factors can be used together with the EXAFS equation to get the structural parameters from the measured data. These calculations can be done in R-space or k-space due to the use of Fourier transform. Working in R-space has the advantage that single coordination shells can be selected and the higher ones can be ignored [46].

EXAFS copper clusters

The extended K-edge absorption spectra of supported copper clusters in comparison with a copper foil are shown in figure 4.25. Solid copper shows a pronounced fine structure beyond the absorption edge. In contrast, the copper clusters do not show such a distinct high frequency structure. Rather, the continuum absorption is superimposed with a low frequency structure, which does not originate from single scattering and hence does not belong to the EXAFS fine structure. The three features at ≈ 9000 eV, ≈ 9050 eV and ≈ 9130 eV are the most dominant features in the absorption spectra of the copper clusters. Interestingly, the cluster spectra, especially the Cu_{35} spectrum measured under vacuum, look similar to the spectra of copper clusters on an amorphous carbon substrate measured by Apai *et al.* [97]. These authors measured the K-edge absorption spectra of copper clusters formed by

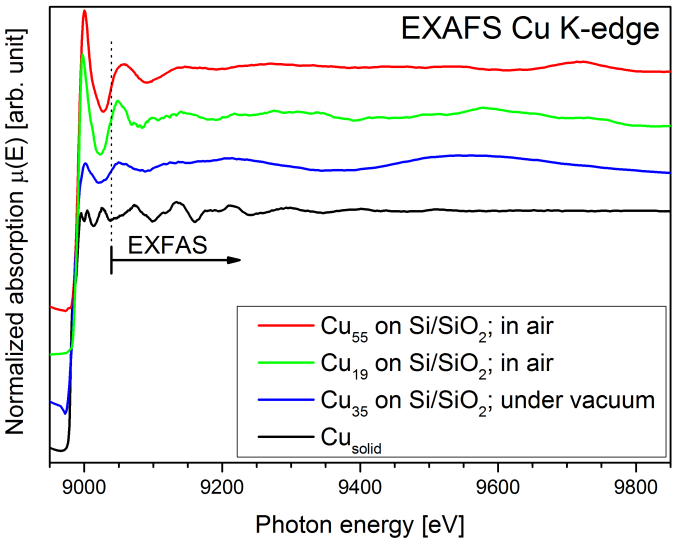

Figure 4.25: *EXAFS spectra of silica supported copper clusters and a copper foil. Cu_{35} has been measured under vacuum conditions whereas Cu_{19} and Cu_{55} has been measured in air. The EXAFS fine structure is much less pronounced in the cluster spectra as compared to the spectrum of solid copper.*

vapour deposition as a function of the atomic surface density. The spectrum with the lowest surface density of $8 \cdot 10^{14}$ atoms per cm^2 shown in [97] also shows the aforementioned features at the same photon energy as presented in this work.

Figure 4.26 shows the individual EXAFS spectra together with the corresponding atomic background. The atomic background of solid copper is quite linear beyond the absorption edge. No low-frequency structure is present in the spectrum and the EXAFS can be easily extracted. In the cluster spectra a high proportion of low frequencies is present, visible by the long wiggles beyond the absorption edge. Therefore, the atomic background spline has been fitted to the low frequency structure to make this structure non-existent in the EXAFS. Otherwise the low frequencies can cause unphysically short distances in the pseudo radial distribution function after Fourier transformation of the EXAFS. In case of the oxidised samples the high increase of intensity at the absorption edge has to be considered during atomic background fitting. This is the reason for the huge increase of the spline function

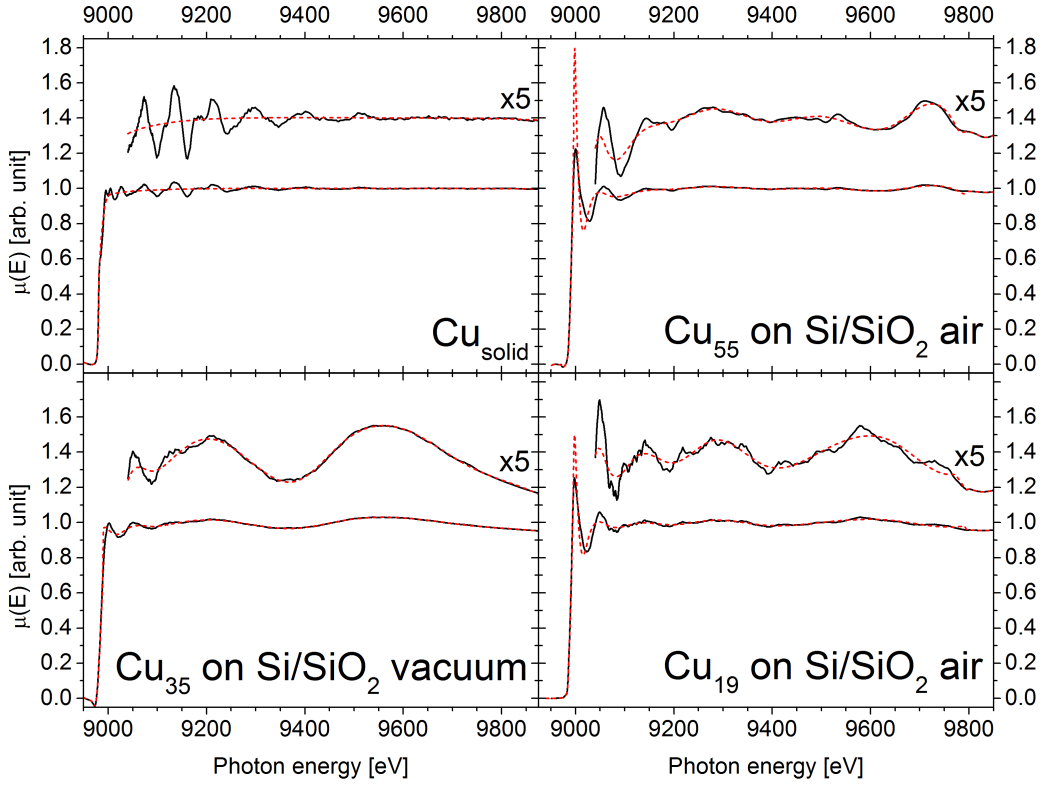

Figure 4.26: *EXAFS spectra of the measured samples (black) together with their corresponding atomic background (red). The EXAFS region is additionally shown five times enhanced. During background fitting it is important to remove the low frequency wiggles beyond the absorption edge of the cluster spectra. The EXAFS region is enhanced by a factor of 5.*

at ≈ 9000 eV photon energy. Unfortunately the huge increase of the spline cannot be avoided. However it has no effect on the EXAFS evaluation as it belongs to the XANES region.

The isolated, k^2-weighted EXAFS in k-space of all samples is shown in figure 4.27. It is conspicuous that the fine structures of the copper foil and Cu_{35} measured under vacuum conditions show a biconvex envelope whereas the fine structures of the aerated Cu_{19} and Cu_{55} samples show a biconcave envelope. Weighting with different powers of k is done to counteract the attenuation of the oscillatory structure with increasing k. The amplitude of the oscillations can be made more or less constant over the whole k-range and also the resolution of the Fourier transform can be increased. On the other hand the noise of the EXAFS signal is amplified by too strong weighting. For the cluster data weighting with k^2 has been the best compromise.

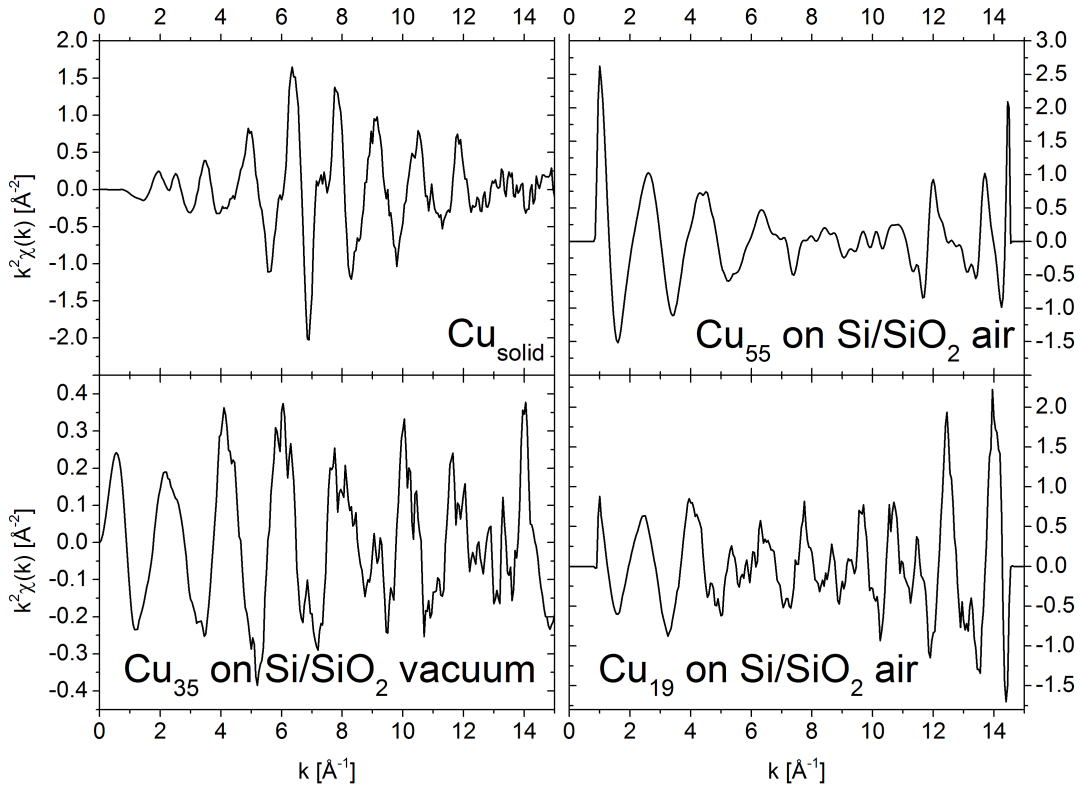

Figure 4.27: *k^2-weighted EXAFS in k-space of solid copper and the clusters Cu_{55}, Cu_{35} and Cu_{19}.*

After Fourier transforming the k^2-weighted EXAFS the pseudo radial distribution functions of copper solid and clusters are received as shown in figure 4.28. Solid copper shows an intense feature at 2.25 Å. The first nearest neighbour distance of fcc copper is 2.55 Å as determined by X-ray diffraction [111]. That means the value of α^{Cu-Cu} (equation 4.17), which has to be added to the position of the latter feature is

0.3 Å. As the phase shift only depends on the element and not on the chemical environment [109] the same shift can be applied to the cluster data for Cu-Cu distances.

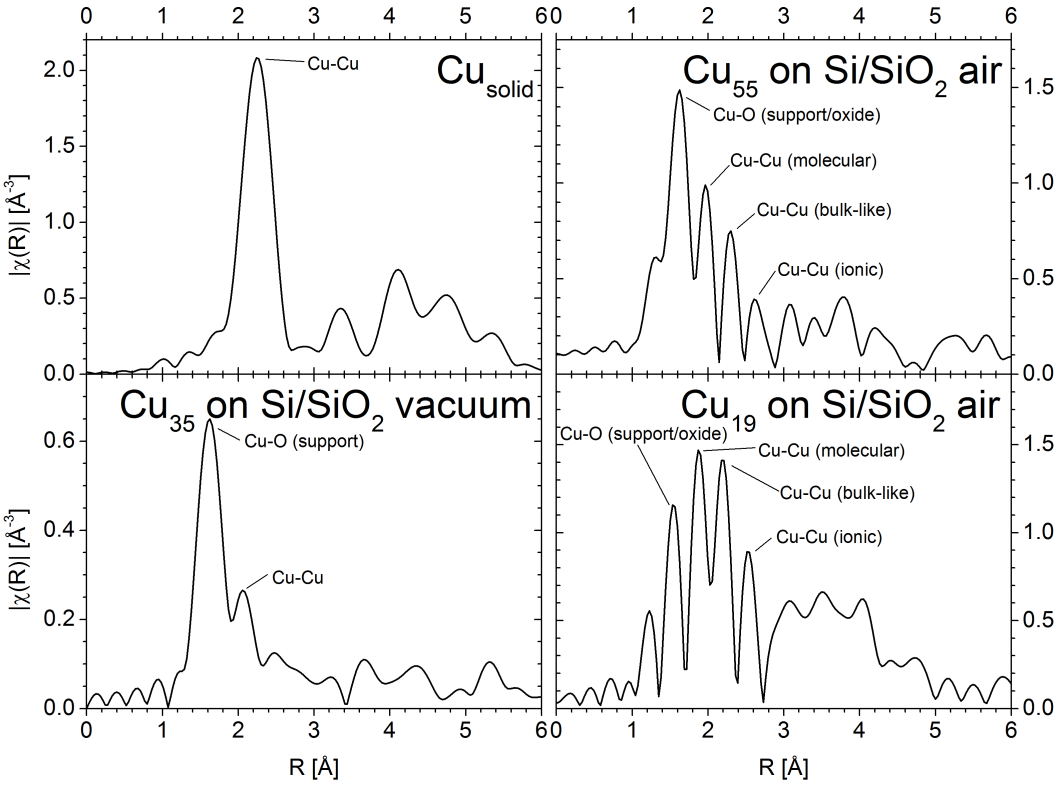

Figure 4.28: *k^2-weighted EXFAS in R-space of solid copper and the clusters Cu_{55}, Cu_{35} and Cu_{19} (non phase corrected).*

The pseudo radial distribution function of Cu_{35} shows two features at 1.62 Å and 2.06 Å, respectively. The feature at R = 2.06 Å can be attributed to a Cu-Cu nearest neighbour distance of 2.36 Å (including phase shift correction) which is comparable to a Cu-Cu distance of copper islands found by Apai *et al.* [97]. These authors observe a nearest neighbour distance of 2.33 Å for vapour deposited copper clusters on amorphous carbon with an atomic density of $8 \cdot 10^{14}$ atoms per cm^2. The other feature, located at 1.62 Å, cannot be attributed to Cu-Cu bonds since the bond length would be too short. We explain this feature by bonds between copper atoms of the cluster and oxygen atoms of the silica layer of the support as the Cu-O bond lengths are usually shorter than Cu-Cu bond lengths. To determine the Cu-O bong length the value of α^{Cu-O} is needed, i.e. the phase shift the photoelectron matter wave experiences, which has its origin at the absorbing copper atom and is backscattered from an oxygen atom. To determine α^{Cu-O} the position of the features in the pseudo radial distribution function of CuO and Cu_2O have to be compared with the literature values of the nearest neighbour distances. As the two

possible copper oxygen compounds have not been measured during this work for the determination of α^{Cu-O} the K-edge absorption spectra have been taken from a web-based library of XAFS data on model compounds [112]. The pseudo radial distribution functions of CuO and Cu_2O reveal a feature at 1.53 Å and 1.42 Å, respectively, which correspond to the first Cu-O nearest neighbour distance. The Cu-O bond length in CuO and Cu_2O is 1.95 Å and 1.84 Å, respectively, as received by X-ray diffraction [111, 113]. Thus for α^{Cu-O} a value of 0.42 Å has been determined. The same value has been applied to the cluster data for evaluation of the EXAFS and calculation of the Cu-O bond length due to the transferability of phase shifts [109]. Now we can come back to Cu_{35} and its feature at R = 1.62 Å. With the received α^{Cu-O} the Cu-O bond length has been calculated to 2.04 Å. This distance is about 0.1 Å longer than the Cu-O distance of CuO reported in various literature.

The EXAFS of the oxidised samples (Cu_{19} and Cu_{55}) look strikingly different as compared to the sample measured under vacuum conditions (Cu_{35}). The pseudo radial distribution functions of Cu_{19} and Cu_{55} look similar to each other except that the characteristic features are shifted about 0.1 Å from each other. The EXAFS of Cu_{19} and Cu_{55} show features at 1.23 Å, 1.55 Å, 1.88 Å, 2.19 Å, 2.53 Å and 1.31 Å, 1.62 Å, 1.97 Å, 2.29 Å, 2.62 Å, respectively. The features at 1.23 Å and 1.31 Å certainly cannot be attributed to Cu-Cu bonds and also not to Cu-O bonds. For the samples exposed to atmospheric pressure it is imaginable that copper atoms are bound to carbon atoms. Nevertheless, also this bond distance would be too short as the Cu-C bond distance in organocopper compounds is about 1.85 - 1.9 Å [114]. As in the case of Cu_{35} the features at 1.55 Å and 1.62 Å can be attributed to Cu-O bonds. Increased by $\alpha^{Cu-O} = 0.42$ Å the latter features yield a Cu-O bond length of 1.97 Å and 2.04 Å for Cu_{19} and Cu_{55}, respectively. We suppose that inner-cluster Cu-O bonds and Cu-O bonds between cluster and silica atoms have about the same bond length.

The three next features of both Cu_{19} and Cu_{55} are attributed to Cu-Cu bonds. By adding $\alpha^{Cu-Cu} = 0.3$ Å to the positions of the features in the EXAFS the following Cu-Cu bond lengths have been received. 2.18 Å and 2.27 Å, 2.49 Å and 2.59 Å, 2.83 Å and 2.92 Å for Cu_{19} and Cu_{55}, respectively. The first set of distances with 2.18 Å and 2.27 Å are quite short. However, these bond lengths are in good agreement with the Cu-Cu bond distance in the copper dimer, which has been found to be 2.22 Å [115]. Montano *et al.* [14] also found such a short Cu-Cu bond length in 6 Å mean diameter copper particles. The next bond lengths appearing are 2.49 Å and 2.59 Å for Cu_{19} and Cu_{55}, respectively. The Cu-Cu bond length for Cu_{19} is somewhat shorter than the first nearest neighbour distance of solid copper whereas the Cu-Cu bond length for Cu_{55} is somewhat longer. In fact, Montano *et al.* [14]

found a Cu-Cu distance of 2.54 Å for small copper particles embedded in solid argon with a size of 10 Å (this equates to approximately Cu_{50}) in diameter. The largest Cu-Cu bond lengths of 2.83 Å and 2.92 Å for Cu_{19} and Cu_{55}, respectively, are longer than the first nearest neighbour distance of solid copper (2.55 Å). However these large Cu-Cu bond lengths have been found for copper oxides with a distance of 2.9 Å and 3 Å for CuO and Cu_2O, respectively [111].

bond length [Å] (phase corrected)	Cu_{35}	Cu_{19}	Cu_{55}	Cu_{solid}	Cu-oxides
Cu-Cu ($\alpha^{Cu\text{-}Cu}$=0.30)	2.36	2.18 *(dimer)*	2.27 *(dimer)*	2.55	2.90 *CuO*
		2.49 *(metal-like)*	2.59 *(metal-like)*		
		2.83 *(oxide,ionic)*	2.92 *(oxide, ionic)*		3.01 *Cu_2O*
Cu-O ($\alpha^{Cu\text{-}O}$=0.42)	2.04 *(silica support)*	1.97 *(silica support/ oxides)*	2.04 *(silica support/ oxides)*		1.95 *CuO*
					1.84 *Cu_2O*

Figure 4.29: *Nearest-neighbour bond lengths as obtained by EXAFS of Cu_{35}, oxidised Cu_{19} and Cu_{55} and solid copper. The applied phase-shift correction factors (α^{Cu-Cu} and α^{Cu-O}) are given too.*

Small deposited copper clusters (Cu_{35}) show a bond length contraction of approximate 8%. The observed bond length contraction is a result of the large number of surface atoms in the clusters. The lower coordination number of surface atoms with respect to bulk atoms causes a reduction of repulsive interactions between non-bonded electron pairs [97]. In oxidised clusters three different Cu-Cu bonds have been found. The shortest bond length is "molecular-like" equal to the copper dimer. Furthermore a bulk-like as well as an extended ionic-like bond length (Cu^+-Cu^+) have been deduced from the EXAFS measurments. The extended bond length is also found in crystalline CuO and Cu_2O. Note that coexisting dimer-like and bulk-like bond lengths have been observed by Mazalova *et al.* [116] for small Cu-O clusters deposited on GaAs.

5 Summary

In the present thesis an X-ray spectroscopy study has been performed on mass-selected deposited metal clusters. To explore the electronic and geometric structure as a function of cluster size a variety of X-ray spectroscopic techniques have been used: X-ray photoelectron spectroscopy has been applied to gold clusters in order to analyse the size-dependent XPS binding energy shift. PCI-Auger electron spectroscopy has been applied to copper clusters to reveal information about the electrostatic screening ability of small clusters. Moreover extended X-ray absorption spectroscopy has been used to receive nearest neighbour distances of mass-selected copper clusters.

An overall blue shift of the Au 4f XPS binding energy with respect to the bulk peak is observed, which scales linearly with the inverse cluster radius. The systematic ESCA shift can be explained within the liquid drop model by an electrostatic final state effect which dominates the peak shift. The core ionisation potential as a function of the inverse cluster radius for supported gold clusters changes less strongly than expected for free clusters. Therefore we assume intense final-state screening of the ionised cluster by charge transfer from the substrate on a timescale relevant for photoemission. Such extra-atomic final-state screening by the substrate and a peak asymmetry on the high binding energy side of the photoelectron peak furthermore give evidence for chemisorption-like interaction between the clusters and substrate. The dynamic screening model is useful to explain the relatively small XPS shift with respect to the free clusters and the liquid drop model. The additional Gauss broadening is attributed to inhomogeneous broadening and phonon broadening. Cluster specific "each-atom-counts" behaviour is not evident for the size-dependent XPS shift of small supported gold clusters. The photoelectron intensity at binding energies smaller than the gold bulk peak is interpreted as an initial state effect due to the reduced coordination of cluster atoms. This initial state effect causes a red shift in binding energy but is mainly overcompensated by the electrostatic final state effect.

Excitation-energy dependent Auger spectra of supported copper clusters exhibit a cluster-size dependent evolution of the PCI interaction energy. The PCI shift reveals that the photoelectron core-hole interaction gradually changes from a Coulomb-like into a screened Coulomb-like interaction within the sub-nm range. As a result of the fairly reduced screening ability supported copper clusters smaller than 1 nm should be considered to be clearly less metallic than the solid. A gradual change into a metallic-like screening behaviour evolves at a diameter between 1 and 2 nm.

Small deposited copper clusters (Cu_{35}) show a bond length contraction of approximate 8%. In oxidised clusters three different Cu-Cu bonds have been found. The shortest bond length is "molecular-like" equal to the copper dimer. Further-

more a bulk-like as well as an extended ionic-like bond length (Cu^+-Cu^+) have been deduced from the EXAFS measurments.

To carry on the work done in this thesis it is most important to study bigger clusters (n$\geq$200). It would be very interesting to repeat the gold XPS measurements on free clusters to completely neglect the substrate influence and obtain the pure cluster properties. Core hole spectroscopy on free clusters has not been done so far using synchrotron radiation due to the lack of intensity. One possibility is the use of a continuously working high-output magnetron cluster sources in conjunction with a velocity map imaging (VMI) electron spectrometer [117] to enhance the signal. Especially for further structure investigation an extended series of copper clusters should be studied by EXAFS. In addition the clusters should be oxidises in a controlled manner. The measurement of absorption spectroscopy on free clusters at synchrotrons is possible with the use of ion traps. The comparison of free and supported clusters can elucidate the influence of the substrate on the structure of the clusters. Another way to decrease the cluster-substrate interaction is the deposition onto less interacting materials such as MgO or HOPG. However, due to the low cluster-substrate interaction special deposition techniques are required to avoid agglomeration.

References

[1] O. Sipr, J. Minar, and H. Ebert. Magnetism of free and supported clusters: a comparative study. *Central European Journal of Physics*, **7**(2):257–263, 2009.

[2] K. Rademann, B. Kaiser, U. Even, and F. Hensel. Size dependence of the gradual transition to metallic properties in isolated mercury clusters. *Physical Review Letters*, **59**(20):2319–2321, 1987.

[3] V. Senz, T. Fischer, P. Oelßner, J. Tiggesbäumker, J. Stanzel, C. Bostedt, H. Thomas, M. Schöffler, L. Foucar, M. Martins, J. Neville, M. Neeb, T. Möller, W. Wurth, E. Rühl, R. Dörner, H. Schmidt-Böcking, W. Eberhardt, G. Ganteför, R. Treusch, P. Radcliffe, and K.-H. Meiwes-Broer. Core-Hole Screening as a Probe for a Metal-to-Nonmetal Transition in Lead Clusters. *Physical Review Letters*, **102**(13):138303, 2009.

[4] U. Heiz, A. Sanchez, S. Abbet, and W.-D Schneider. Catalytic Oxidation of Carbon Monoxide on Monodispersed Platinum Clusters: Each Atom Counts. *Journal of the American Chemical Society*, **121**(13):3214–3217, 1999.

[5] H. Häkkinen and U. Landman. Gas-Phase Catalytic Oxidation of CO by Au 2-. *Journal of the American Chemical Society*, **123**(39):9704–9705, 2001.

[6] N. Nilius, M. Ganduglia-Pirovano, V. Brázdová, M. Kulawik, J. Sauer, and H.-J Freund. Counting Electrons Transferred through a Thin Alumina Film into Au Chains. *Physical Review Letters*, **100**(9):096802, 2008.

[7] S. Peredkov, S. Sorensen, A. Rosso, G. Öhrwall, M. Lundwall, T. Rander, A. Lindblad, H. Bergersen, W. Pokapanich, S. Svensson, O. Björneholm, N. Mårtensson, and M. Tchaplyguine. Size determination of free metal clusters by core-level photoemission from different initial charge states. *Physical Review B*, **76**(8):081402, 2007.

[8] C. Bréchignac, M. Broyer, Ph Cahuzac, G. Delacretaz, P. Labastie, J. Wolf, and L. Wöste. Probing the Transition from van der Waals to Metallic Mercury Clusters. *Physical Review Letters*, **60**(4):275–278, 1988.

[9] J. T. Lau, J. Rittmann, V. Zamudio-Bayer, M. Vogel, K. Hirsch, Ph. Klar, F. Lofink, T. Möller, and B. v. Issendorff. Size Dependence of $L_{2,3}$ Branching Ratio and 2p Core-Hole Screening in X-Ray Absorption of Metal Clusters. *Physical Review Letters*, **101**(15):153401, 2008.

[10] S. Peredkov, M. Neeb, W. Eberhardt, J. Meyer, M. Tombers, H. Kampschulte, and G. Niedner-Schatteburg. Spin and Orbital Magnetic Moments of Free Nanoparticles. *Physical Review Letters*, **107**(23):233401, 2011.

[11] M. Niemeyer, K. Hirsch, V. Zamudio-Bayer, A. Langenberg, M. Vogel, M. Kossick, C. Ebrecht, K. Egashira, A. Terasaki, T. Möller, B. v. Issendorff, and J. T. Lau. Spin Coupling and Orbital Angular Momentum Quenching in Free Iron Clusters. *Physical Review Letters*, **108**(5):057201, 2012.

[12] S. DiCenzo, S. Berry, and E. Hartford. Photoelectron spectroscopy of single-size Au clusters collected on a substrate. *Physical Review B*, **38**(12):8465–8468, 1988.

[13] W. Eberhardt, P. Fayet, D. M. Cox, Z. Fu, A. Kaldor, R. D. Sherwood, and D. Sondericker. Photoemission from mass-selected monodispersed Pt clusters. *Physical Review Letters*, **64**(7):780–783, 1990.

[14] P. Montano, G. Shenoy, E. Alp, W. Schulze, and J. Urban. Structure of Copper Microclusters Isolated in Solid Argon. *Physical Review Letters*, **56**(19):2076–2079, 1986.

[15] V. Vijayakrishnan and C. N. R. Rao. An investigation of transition metal clusters deposited on graphite and metal oxide substrates by a combined use of XPS, UPS and Auger spectroscopy. *Surface Science*, **255**(1-2):L516–L522, 1991.

[16] M. Mason. Electronic structure of supported small metal clusters. *Physical Review B*, **27**(2):748–762, 1983.

[17] J. T. Lau, A. Föhlisch, R. Nietubyc, M. Reif, and W. Wurth. Size-Dependent Magnetism of Deposited Small Iron Clusters Studied by X-Ray Magnetic Circular Dichroism. *Physical Review Letters*, **89**(5):057201, 2002.

[18] K.-H. Meiwes-Broer. *Metal clusters at surfaces: Structure, quantum properties, physical chemistry*. Springer, Berlin and and New York, 2000.

[19] S. Peters, S. Peredkov, B. Balkaya, N. Ferretti, A. Savci, A. Vollmer, M. Neeb, and W. Eberhardt. Inner-shell photoionization spectroscopy on deposited metal clusters using soft x-ray synchrotron radiation: An experimental setup. *Review of Scientific Instruments*, **80**(12):125106, 2009.

[20] B. Balkaya. *Aufbau einer Magnetronclusterquelle*. Diploma Thesis, TU Berlin, Berlin, 2005.

[21] R. Klingeler, P. S. Bechthold, M. Neeb, and W. Eberhardt. An experimental setup for nondestructive deposition of size-selected clusters. *Review of Scientific Instruments*, **73**(4):1803, 2002.

[22] H. Haberland. Filling of micron-sized contact holes with copper by energetic cluster impact. *Journal of Vacuum Science & Technology A: Vacuum, Surfaces, and Films*, **12**(5):2925, 1994.

[23] D. L. Olynick, J. M. Gibson, and R. S. Averback. Impurity-suppressed sintering in copper nanophase materials. *Philosophical Magazine A*, **77**(5):1205–1221, 1998.

[24] N. Matsunami, Y. Yamamura, Y. Itikawa, N. Itoh, Y. Kazumata, S. Miyagawa, K. Morita, R. Shimizu, and H. Tawara. Energy dependence of the ion-induced sputtering yields of monatomic solids. *Atomic Data and Nuclear Data Tables*, **31**(1):1–80, 1984.

[25] S. Peters, S. Peredkov, N. Ferretti, A. Savci, and M. Neeb. Core level photoionization spectroscopy of supported metal clusters: Cu_{55} on silica. *Journal of Electron Spectroscopy and Related Phenomena*, **181**(2-3):140–144, 2010.

[26] F. Schäfers. REFLEC 21.10 - a program to calculate VUV/X-RAY optical elements and SYNCHROTRON RADIATION BEAMLINES, 2009.

[27] Lawrence Berkeley National Laboratory. X-RAY DATA BOOKLET, 2011. http://xdb.lbl.gov/.

[28] Helmholtz Zentrum Berlin. Experimental Methods and Beamlines at Bessy II. http://www.helmholtz-berlin.de/user/experimental-infrastructures/instruments-photons/index_en.html.

[29] H. Petersen, C. Jung, C. Hellwig, W. B. Peatman, and W. Gudat. Review of plane grating focusing for soft x-ray monochromators. *Review of Scientific Instruments*, **66**(1):1, 1995.

[30] R. Follath and F. Senf. New plane-grating monochromators for third generation synchrotron radiation light sources. *Nuclear Instruments and Methods in Physics Research Section A: Accelerators, Spectrometers, Detectors and Associated Equipment*, **390**(3):388–394, 1997.

[31] Elettra synchrotron Trieste. Atomic Calculation of Photoionization Cross-Sections and Asymmetry Parameters. http://ulisse.elettra.trieste.it/services/elements/WebElements.html.

[32] A. Erko, I. Packe, C. Hellwig, M. Fieber-Erdmann, O. Pawlizki, M. Veldkamp, and W. Gudat. KMC-2: the new x-ray beamline at BESSY II. *AIP Conference Proceedings*, **521**:415–418, 2000.

[33] A. Erko, I. Packe, W. Gudat, N. Abrosimov, and A. Firsov. A crystal monochromator based on graded SiGe crystals. *Nuclear Instruments and Methods in Physics Research Section A: Accelerators, Spectrometers, Detectors and Associated Equipment*, **467-468**:623–626, 2001.

[34] J. H. Hubbell and S. M. Seltzer. Tables of X-ray Mass Attenuation Coefficients and Mass Energy-Absortion Coefficients, 2004. http://www.nist.gov/pml/data/xraycoef/index.cfm.

[35] H. Hertz. Ueber einen Einfluss des ultravioletten Lichtes auf die electrische Entladung. *Annalen der Physik und Chemie*, **267**(8):983–1000, 1887.

[36] A. Einstein. Über einen die Erzeugung und Verwandlung des Lichtes betreffenden heuristischen Gesichtspunkt. *Annalen der Physik*, **322**(6):132–148, 1905.

[37] S. Doniach and M. Šunjić. Many-electron singularity in X-ray photoemission and X-ray line spectra from metals. *Journal of Physics C: Solid State Physics*, **3**(2):285–291, 1970.

[38] J. J. Olivero and R.L. Longbothum. Empirical fits to the Voigt line width: A brief review. *Journal of Quantitative Spectroscopy and Radiative Transfer*, **17**(2):233–236, 1977.

[39] D. Shirley. High-Resolution X-Ray Photoemission Spectrum of the Valence Bands of Gold. *Physical Review B*, **5**(12):4709–4714, 1972.

[40] S. Tougaard. Quantitative analysis of the inelastic background in surface electron spectroscopy. *Surface and Interface Analysis*, **11**(9):453–472, 1988.

[41] D. L. Adams and J. N. Andersen. FitXPS 2.12, 2001. http://www.sljus.lu.se/download.html.

[42] M. O. Krause. Atomic radiative and radiationless yields for K and L shells. *Journal of Physical and Chemical Reference Data*, **8**(2):307, 1979.

[43] W. Eberhardt, G. Kalkoffen, and C. Kunz. Measurement of the Auger Decay after Resonance Excitation of Xe 4d and Kr 3d Resonance Lines. *Physical Review Letters*, **41**(3):156–159, 1978.

[44] D. Coster and R. de L. Kronig. New type of auger effect and its influence on the x-ray spectrum. *Physica*, **2**(1-12):13–24, 1935.

[45] E. Antonides, E. Janse, and G. Sawatzky. LMM Auger spectra of Cu, Zn, Ga, and Ge, II. Relationship with the L_{23} photoelectron spectra via the $L_2L_3M_{45}$ Coster-Kronig process. *Physical Review B*, **15**(10):4596–4601, 1977.

[46] M. Newville. Fundamentals of XAFS, 2004. http://www.xafs.org.

[47] J. Perdew. Energetics of charged metallic particles: From atom to bulk solid. *Physical Review B*, **37**(11):6175–6180, 1988.

[48] M. Seidl and J. Perdew. Size-dependent ionization energy of a metallic cluster: Resolution of the classical image-potential paradox. *Physical Review B*, **50**(8):5744–5747, 1994.

[49] M. M. Kappes. Experimental studies of gas-phase main-group metal clusters. *Chemical Reviews*, **88**(2):369–389, 1988.

[50] W. de Heer. The physics of simple metal clusters: experimental aspects and simple models. *Reviews of Modern Physics*, **65**(3):611–676, 1993.

[51] B. v. Issendorff and O. Cheshnovsky. METAL TO INSULATOR TRANSITIONS IN CLUSTERS. *Annual Review of Physical Chemistry*, **56**(1):549–580, 2005.

[52] J. Bahn, P. Oelßner, M. Köther, C. Braun, V. Senz, S. Palutke, M. Martins, E. Rühl, G. Ganteför, T. Möller, B. von Issendorff, D. Bauer, J. Tiggesbäumker, and K-H Meiwes-Broer. Pb 4f photoelectron spectroscopy on mass-selected anionic lead clusters at FLASH. *New Journal of Physics*, **14**(7):075008, 2012.

[53] G. K. Wertheim, S. B. DiCenzo, and S. Youngquist. Unit Charge on Supported Gold Clusters in Photoemission Final State. *Physical Review Letters*, **51**(25):2310–2313, 1983.

[54] T. T. P. Cheung. X-ray photoemission of small platinum and palladium clusters. *Surface Science*, **140**(1):151–164, 1984.

[55] Y. Iizuka, H. Fujiki, N. Yamauchi, T. Chijiiwa, S. Arai, S. Tsubota, and M. Haruta. Adsorption of CO on gold supported on TiO_2. *Catalysis Today*, **36**(1):115–123, 1997.

[56] M. Valden. Onset of Catalytic Activity of Gold Clusters on Titania with the Appearance of Nonmetallic Properties. *Science*, **281**(5383):1647–1650, 1998.

[57] M. Haruta. Catalysis: Gold rush. *Nature*, **437**(7062):1098–1099, 2005.

[58] L. Fan. Preparation of Au/TiO_2 catalysts by suspension spray reaction method and their catalytic property for CO oxidation. *Applied Catalysis A: General*, **246**(1):87–95, 2003.

[59] P. Schwerdtfeger. Nanostrukturen von Gold – von kleinen Clustern zu niederdimensionalen Anordnungen. *Angewandte Chemie*, **115**(17):1936–1939, 2003.

[60] D. C. Lim, R. Dietsche, M. Bubek, G. Ganteför, and Y. D. Kim. Oxidation and Reduction of Mass-Selected Au Clusters on SiO_2/Si. *ChemPhysChem*, **7**(9):1909–1911, 2006.

[61] D.M Cox, B. Kessler, P. Fayet, W. Eberhardt, Z. Fu, D. Sondericher, R. Sherwood, and A. Kaldor. Chemical and electronic properties of size selected metal clusters: XPS studies of gold clusters. *Nanostructured Materials*, **1**(2):161–165, 1992.

[62] A. Howard. Initial and final state effects in photoemission from Au nanoclusters on TiO_2(1 1 0). *Surface Science*, **518**(3):210–224, 2002.

[63] H. Kröger, P. Reinke, M. Büttner, and P. Oelhafen. Gold cluster formation on a fullerene surface. *The Journal of Chemical Physics*, **123**(11):114706, 2005.

[64] M. Quinten, I. Sander, P. Steiner, U. Kreibig, K. Fauth, and G. Schmid. Photoemission on gold-55-clusters derived from gold-phosphine $AuP(C_6H_5)_3Cl$. *Z Phys D - Atoms, Molecules and Clusters (Zeitschrift für Physik D Atoms, Molecules and Clusters)*, **20**(1-4):377–379, 1991.

[65] J. J. Yeh and I. Lindau. Atomic subshell photoionization cross sections and asymmetry parameters: $1 \leq Z \leq 103$. *Atomic Data and Nuclear Data Tables*, **32**(1):1–155, 1985.

[66] P. Citrin, G. K. Wertheim, and Y. Baer. Surface-atom x-ray photoemission from clean metals: Cu, Ag, and Au. *Physical Review B*, **27**(6):3160–3175, 1983.

[67] J. C. Fuggle and N. Mårtensson. Core-level binding energies in metals. *Journal of Electron Spectroscopy and Related Phenomena*, **21**(3):275–281, 1980.

[68] P. Citrin and G. K. Wertheim. Photoemission from surface-atom core levels, surface densities of states, and metal-atom clusters: A unified picture. *Physical Review B*, **27**(6):3176–3200, 1983.

[69] J. D. Jackson. *Classical electrodynamics*. Wiley, New York, 3. edition, 1999.

[70] M. Patanen, S. Aksela, S. Urpelainen, T. Kantia, S. Heinäsmäki, and H. Aksela. Free atom 4f photoelectron spectra of Au, Pb, and Bi. *Journal of Electron Spectroscopy and Related Phenomena*, **183**(1-3):59–63, 2011.

[71] T. T. P. Cheung. X-ray photoemission of Pb and Sn particles supported on carbon. *Chemical Physics Letters*, **110**(2):219–222, 1984.

[72] S. B. DiCenzo and G. K. Wertheim. Comment on "core binding energies for clusters deposited on different insulating substrates: ESCA spectra and theoretical electronic structure studies". *Journal of Electron Spectroscopy and Related Phenomena*, **43**(3):C7–C12, 1987.

[73] H. Hövel, B. Grimm, M. Pollmann, and B. Reihl. Cluster-Substrate Interaction on a Femtosecond Time Scale Revealed by a High-Resolution Photoemission Study of the Fermi-Level Onset. *Physical Review Letters*, **81**(21):4608–4611, 1998.

[74] H. Hövel, I. Barke, H.-G Boyen, P. Ziemann, M. Garnier, and P. Oelhafen. Photon energy dependence of the dynamic final-state effect for metal clusters at surfaces. *Physical Review B*, **70**(4):045424, 2004.

[75] J. C. Fuggle, E. Umbach, D. Menzel, K. Wandelt, and C.R Brundle. Adsorbate line shapes and multiple lines in XPS; comparison of theory and experiment. *Solid State Communications*, **27**(2):65–69, 1978.

[76] H. Häkkinen, B. Yoon, U. Landman, X. Li, H.-J. Zhai, and L.-S. Wang. On the Electronic and Atomic Structures of Small Au_N^- (N = 4−14) Clusters: A Photoelectron Spectroscopy and Density-Functional Study. *The Journal of Physical Chemistry A*, **107**(32):6168–6175, 2003.

[77] W. Eberhardt, P. Fayet, D. M. Cox, Z. Fu, A. Kaldor, R. D. Sherwood, and D. Sondericker. Core level photoemission from monosize mass selected Pt clusters deposited on SiO_2 and amorphous carbon. *Physica Scripta*, **41**(6):892–895, 1990.

[78] H. Häkkinen, M. Moseler, and U. Landman. Bonding in Cu, Ag, and Au Clusters: Relativistic Effects, Trends, and Surprises. *Physical Review Letters*, **89**(3):033401, 2002.

[79] J. Stanzel, M. Neeb, W. Eberhardt, P. Lisinetskaya, J. Petersen, and R. Mitrić. Switching from molecular to bulklike dynamics in electronic relaxation of a small gold cluster. *Physical Review A*, **85**(1):013201, 2012.

[80] M. Cini and P. Ascarelli. Quantum size effects in metal particles and thin films by an extended RPA. *Journal of Physics F: Metal Physics*, **4**(11):1998–2008, 1974.

[81] M. Cini. Dielectric response of arbitrary surfaces and size quantized metals. *Surface Science*, **62**(1):148–164, 1977.

[82] C.-Y. Cha, G. Ganteför, and W. Eberhardt. Photoelectron spectroscopy of Cu_n^- clusters: Comparison with jellium model predictions. *The Journal of Chemical Physics*, **99**(9):6308, 1993.

[83] R. Busani, M. Folkers, and O. Cheshnovsky. Direct Observation of Band-Gap Closure in Mercury Clusters. *Physical Review Letters*, **81**(18):3836–3839, 1998.

[84] R. Barker and H. Berry. Electron Energy Distributions from Ionizing Collisions of Helium and Neon Ions with Helium. *Physical Review*, **151**(1):14–19, 1966.

[85] V. Schmidt, N. Sandner, W. Mehlhorn, M. Adam, and F. Wuilleumier. Post-Collision Interaction in the Xenon $N_{4,5}$-OO Auger Spectrum Excited by Photon Impact. *Physical Review Letters*, **38**(2):63–66, 1977.

[86] T. Miller and T.-C. Chiang. Solid-state screening effect on the post-collision interaction. *Physical Review B*, **29**(2):1121–1124, 1984.

[87] W. Eberhardt, S. Bernstorff, H. Jochims, S. Whitfield, and B. Crasemann. Photoelectron recapture through post-collision interaction. *Physical Review A*, **38**(7):3808–3811, 1988.

[88] J. P. Tobin, W. Hirschwald, and J. Cunningham. XPS and XAES studies of transient enhancement of Cu^I at CuO surfaces during vacuum outgassing. *Applications of Surface Science*, **16**(3-4):441–452, 1983.

[89] S. Peters. *Röntgen-Photoemissionsspektroskopie an deponierten Kupfer- und Goldclustern*. Diploma Thesis, TU Berlin, Berlin, 2009.

[90] L. Yin, I. Adler, T. Tsang, M. Chen, D. Ringers, and B. Crasemann. Widths of atomic M-shell vacancy states and quasiatomic aspects of radiationless transitions in solids. *Physical Review A*, **9**(3):1070–1080, 1974.

[91] F. Himpsel, F. McFeely, A. Taleb-Ibrahimi, J. Yarmoff, and G. Hollinger. Microscopic structure of the SiO_2/Si interface. *Physical Review B*, **38**(9):6084–6096, 1988.

[92] A. Niehaus. Analysis of post-collision interactions in Auger processes following near-threshold inner-shell photoionization. *Journal of Physics B: Atomic and Molecular Physics*, **10**(10):1845–1857, 1977.

[93] M. Böyükata and J. C. Belchior. Structural and energetic analysis of copper clusters: MD study of Cu_n (n = 2-45). *Journal of the Brazilian Chemical Society*, **19**(5):884–893, 2008.

[94] D. Alamanova, V. G. Grigoryan, and M. Springborg. Deposition of copper clusters on the Cu(111) surface. *Surface Science*, **602**(7):1413–1422, 2008.

[95] R. Schaub, H. Jödicke, F. Brunet, R. Monot, J. Buttet, and W. Harbich. Decorated Ag_{19} on Pt(111) or the "Rare Gas Necklace". *Physical Review Letters*, **86**(16):3590–3593, 2001.

[96] Z. Y. Li, N. P. Young, M. Di Vece, S. Palomba, R. E. Palmer, A. L. Bleloch, B. C. Curley, R. L. Johnston, J. Jiang, and J. Yuan. Three-dimensional atomic-scale structure of size-selected gold nanoclusters. *Nature*, **451**(7174):46–48, 2007.

[97] G. Apai, J. Hamilton, J. Stohr, and A. Thompson. Extended X-Ray—Absorption Fine Structure of Small Cu and Ni Clusters: Binding-Energy and Bond-Length Changes with Cluster Size. *Physical Review Letters*, **43**(2):165–169, 1979.

[98] S. Kraft, J. Stümpel, P. Becker, and U. Kuetgens. High resolution x-ray absorption spectroscopy with absolute energy calibration for the determination of absorption edge energies. *Review of Scientific Instruments*, **67**(3):681, 1996.

[99] A. Gaur, B. D. Shrivastava, and S. K. Joshi. Copper K-edge XANES of Cu(I) and Cu(II) oxide mixtures. *Journal of Physics: Conference Series*, **190**:012084, 2009.

[100] H. Oyanagi, Z. H. Sun, Y. Jiang, M. Uehara, H. Nakamura, K. Yamashita, Y. Orimoto, L. Zhang, C. Lee, A. Fukano, and H. Maeda. Small copper clusters studied by x-ray absorption near-edge structure. *Journal of Applied Physics*, **111**(8):084315, 2012.

[101] L. Lei, Z. Lei, C. Kaitai, and L. Yufen. Critical Size of a Crossover from Noncrystalline Icosahedra to Crystalline Cuboctahedra Structure for Copper Clusters. *Chinese Physics Letters*, **10**(3):139–142, 1993.

[102] J. Farges, M. F. de Feraudy, B. Raoult, and G. Torchet. Noncrystalline structure of argon clusters. I. Polyicosahedral structure of Ar_N clusters, $20 \leq N \leq 50$. *The Journal of Chemical Physics*, **78**(8):5067, 1983.

[103] V. L. Mazalova, A. V. Soldatov, S. Adam, A. Yakovlev, T. Möller, and R. L. Johnston. Small Copper Clusters in Ar Shells: A Study of Local Structure. *The Journal of Physical Chemistry C*, **113**(21):9086–9091, 2009.

[104] D. Reinhard, B. Hall, P. Berthoud, S. Valkealahti, and R. Monot. Size-Dependent Icosahedral-to-fcc Structure Change Confirmed in Unsupported Nanometer-Sized Copper Clusters. *Physical Review Letters*, **79**(8):1459–1462, 1997.

[105] M. Newville. IFEFFIT: interactive XAFS analysis and FEFF fitting. *Journal of Synchrotron Radiation*, **8**(2):322–324, 2001.

[106] B. Ravel and M. Newville. ATHENA , ARTEMIS , HEPHAESTUS: Data analysis for X-ray absorption spectroscopy using IFEFFIT. *Journal of Synchrotron Radiation*, **12**(4):537–541, 2005.

[107] J. J. Rehr and R. C. Albers. Theoretical approaches to x-ray absorption fine structure. *Reviews of Modern Physics*, **72**(3):621–654, 2000.

[108] M. Bauer and H. Bertagnolli. X-ray absorption spectroscopy - the method and its applications. *Bunsenmagazin*, pages 216–231, 2007.

[109] P. Citrin, P. Eisenberger, and B. Kincaid. Transferability of Phase Shifts in Extended X-Ray Absorption Fine Structure. *Physical Review Letters*, **36**(22):1346–1349, 1976.

[110] E. Stern, D. Sayers, and F. Lytle. Extended x-ray-absorption fine-structure technique. III. Determination of physical parameters. *Physical Review B*, **11**(12):4836–4846, 1975.

[111] K. Tohji, Y. Udagawa, T. Mizushima, and A. Ueno. The structure of the copper/zinc oxide catalyst by an in-situ EXAFS study. *The Journal of Physical Chemistry*, **89**(26):5671–5676, 1985.

[112] M. Newville, S. A. Carroll, P. A. O'Day, G. Waychunas, and M. Ebert. A web-based library of XAFS data on model compounds. *Journal of Synchrotron Radiation*, **6**(3):276–277, 1999.

[113] G. Martens, P. Rabe, N. Schwentner, and A. Werner. Improved extended-x-ray-absorption fine-structure (EXAFS) studies applied to the investigation of Cu-O, Cu-N, and Cu-Br bond lengths. *Physical Review B*, **17**(4):1481–1488, 1978.

[114] Z. Rappoport and I. Marek. *The chemistry of organocopper compounds*. Wiley, Chichester and and Hoboken and NJ, 2009.

[115] N. Aslund, R. F. Barrow, W. G. Richards, and D. N. Travis. Rotational analysis of bands of the B-X system of Cu_2 and of the A-X system of Bi_2. *Arkiv för Fysik*, **30**:171, 1965.

[116] V. L. Mazalova, A. V. Soldatov, H. Oyanagi, and K. Tamura. Structure of the electrochemically deposited Cu nanoclusters on p-GaAs(100) surface in H_2SO_4. *Journal of Physics: Conference Series*, **190**:012127, 2009.

[117] A. T. J. B. Eppink and D. H. Parker. Velocity map imaging of ions and electrons using electrostatic lenses: Application in photoelectron and photofragment ion imaging of molecular oxygen. *Review of Scientific Instruments*, **68**(9):3477, 1997.

Publications

1. S. Peters, S. Peredkov, B. Balkaya, N. Ferretti, A. Savci, A. Vollmer, M. Neeb, and W. Eberhardt. Inner-shell photoionization spectroscopy on deposited metal clusters using soft x-ray synchrotron radiation: An experimental setup. *Review of Scientific Instruments*, **80**(12):125106, 2009.

2. S. Peters, S. Peredkov, N. Ferretti, A. Savci, and M. Neeb. Core level photoionization spectroscopy of supported metal clusters: Cu_{55} on silica. *Journal of Electron Spectroscopy and Related Phenomena*, **181**(2-3):140-144, 2010.

3. S. Peters, S. Peredkov, B. Balkaya, N. Ferretti, M. Neeb, and W. Eberhardt. Evolution of metallic screening in small metal clusters probed by PCI-Auger spectroscopy. *Physical Chemistry Chemical Physics*, **12**(33):9867, 2010.

4. S. Peredkov, A. Savci, S. Peters, M. Neeb, W. Eberhardt, H. Kampschulte, J. Meyer, M. Tombers, B. Hofferberth, F. Menges, and G. Niedner-Schatteburg. X-ray absorption spectroscopy of mass-selected transition metal clusters using a cyclotron ion trap: An experimental setup for measuring XMCD spectra of free clusters. *Journal of Electron Spectroscopy and Related Phenomena*, **184**(3-6):113-118, 2011.

5. S. Peters, S. Peredkov, M. Al-Hada, M. Neeb and W. Eberhardt. Size-dependent XPS spectra of small supported Au-clusters. In Press, *Surface Science*, 2012, http://dx.doi.org/10.1016/j.susc.2012.09.024

Acknowledgements

Nicht ungenannt dürfen die folgenden Personen bleiben, welchen ich für ihre Hilfe und Unterstützung während meiner Zeit als Doktorand bei Bessy danken möchte.

Bei meinem Doktorvater, Prof. Dr. Wolfgang Eberhardt, möchte ich mich herzlich für die Möglichkeit bedanken bei ihm zu Promovieren, für seine vertvolle Kritik und sein Vertrauen in mich.

Außerordentlicher Dank geht an meinen Betreuer Dr. Matthias Neeb, mit dem ich nun schon fast fünf Jahre zusammenarbeiten durfte. Matthias hatte immer ein offenes Ohr für mich und hat mich in jeder Hinsicht tatkräftig unterstützt.

Aus meiner Arbeitsgruppe bei Bessy möchte ich Dr. Cosmin Lupulescu, Dr. Mohamed Al-Hada und ganz besonders Dr. Sergey Peredkov danken. Sergey hat mich sehr oft bei Messzeiten unterstützt und ich habe unsere Zusammenarbeit immer sehr genossen.

Peter Bischoff und Ali Savci danke ich für ihre Hilfe bei Elektronikarbeiten und Softwareprogrammierung.

Den Beamlinebetreuern von Bessy möchte ich danken, insbesondere Dr. Antje Vollmer von Beamline PM4, Stefan Pohl, Dr. Stefan Krause und Dr. Patrick Hoffmann von Beamline UE52 und Prof. Dr. Alexei Erko und Dr. Maria Brzhezinskaya von Beamline KMC-2.

Sehr dankbar bin ich für den guten Support bei Bessy, sei es die Werkstatt, die Elektronik- oder Vakuumgruppe. Vielen Dank Andreas Drescher, Torsten Wagner, Gert Meyer, Olaf Pawlizki, Andreas Meißner und Christian Kalus.

Zuletzt möchte ich meiner Familie, ganz besonders meiner Frau Stefanie und meiner Tochter Annike, für die aufmunternde Zeit neben der oft anstrengenden und deprimierenden Zeit als Doktorand danken.